High-redshift radio galaxy searches with the MeerKAT Galaxy Cluster Legacy Survey

Author:
Vasco Cossa

Supervisors:
Dr. Kenda Knowles
Prof. Oleg Smirnov

A thesis submitted in fulfilment of the requirements for the degree of **Master of Science in Physics**

Centre for Radio Astronomy Techniques and Technologies
Department of Physics and Electronics

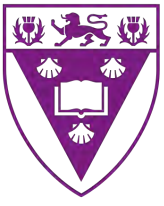

RHODES UNIVERSITY
Where leaders learn

August 2025

Declaration of Authorship

I, VASCO COSSA, declare that this thesis titled, "High-redshift radio galaxy searches with the MeerKAT Galaxy Cluster Legacy Survey" and the work presented in it are my own. I confirm that:

- This work was done wholly or mainly while in candidature for a research degree at this University.
- Where any part of this thesis has previously been submitted for a degree or any other qualification at this University or any other institution, this has been clearly stated.
- Where I have consulted the published work of others, this is always clearly attributed.
- Where I have quoted from the work of others, the source is always given. Except for such quotations, this thesis is entirely my work.
- I have acknowledged all main sources of help.
- Where the thesis is based on work done by myself jointly with others, I have made clear exactly what was done by others and what I have contributed myself.

July 2025

Publications

- Cossa, V. and Knowles, K. and Smirnov, O. (2024). Searching for high-redshift radio galaxies with the MeerKAT Galaxy Cluster Legacy Survey. Proceedings of the 68th Annual Conference of the South African Institute of Physics, pp. 394–401. SBN: 978-1-0370-2645-4. Johannesburg, South Africa: *The South African Institute of Physics.*

"Somewhere, something incredible is waiting to be known."

Carl Sagan

Abstract

We present the results of a search for high-redshift radio galaxy (HzRG) candidates using 30 of the 115 cluster fields of the MeerKAT Galaxy Cluster Legacy Survey (MGCLS). These fields were selected for their good dynamic range, astrometric accuracy, and full optical and infrared coverage from the Dark Energy Camera Legacy Survey (DECaLS) and the All-sky Wide Infrared Survey Explorer (AllWISE), respectively. Using multi-wavelength data and in-band radio spectral index measurements, we find 777 HzRG candidates, and an additional 1,040 faint sources lacking spectral data as potential candidates. Together, these 1,817 candidates represent 0.91% of the full sample. We obtained complete spectral coverage for all sources above 0.76 mJy and complete spectral index measurements down to 30 μJy, probing the faintest GHz-frequency population ever targeted in HzRG searches to date. Taking advantage of in-band spectral index measurements produced in this study, we also investigate the limitations of the assumption of the literature's canonical synchrotron spectral index $\alpha = -0.7$ for inter-frequency flux density extrapolation. Using both the canonical spectral index and our in-band spectral index measurements, we compared the flux densities for MGCLS point sources extrapolated to three different frequencies in different signal-to-noise ratios (SNR), relating to existing radio large-area sky surveys at 100 MHz, 400 MHz, and 1 GHz away from the MGCLS centre frequency, respectively. Although the assumption $\alpha = -0.7$ did not have any effect at the 100 MHz separation, it introduced a 7% deviation at 400 MHz frequency separation for high SNR sources and overestimated flux densities by a factor of 4 for the 1 GHz frequency separation. These results demonstrate that relying on the canonical spectral index for flux density extrapolation is only reliable for frequency offsets below 400 MHz and not reliable for frequency offsets around 1 GHz, even at high SNR, reinforcing the importance of using measured in-band spectral indices for reliable low-frequency flux density extrapolations.

Keywords: high-redshift radio galaxies; galaxy surveys.

Acknowledgements

I would like to express my deep gratitude to my supervisor, Dr. Kenda Knowles, for her invaluable guidance, support, and encouragement throughout this research. I am also grateful to Prof. Oleg Smirnov for enabling me to pursue this academic journey through the group bursary at Rhodes University Centre for Radio Astronomy Techniques Technologies (RATT). Special thanks to Dr. Nadeem Oozeer, Dr. Benjamin Hugo, Dr. Ilani Loubser, Dr. Landman Bester, Dr. Rosalind Skelton, Prof. James Chibueze and Dr. Tim Molteno for their insightful contributions and engagement in my work.

I am equally grateful to all my colleagues at RATT who were keen to help and answer my questions when needed and for their camaraderie and support, especially Dr. Lexy, Dr. Cyndie, Dr. Eric, Dr. Ramij, Athanaseus, Mikaela, Toivo, Victoria, Keegan, Koketso, Elizabeth, and Brenda.

To my family and all my friends, your unwavering encouragement has been my anchor and I thank you wholeheartedly. Lastly, I extend my appreciation to the Mozambican Astronomical Society steering committee for their dedication to promoting astronomy and science in Mozambique and inspiring a new generation of students in this field.

Contents

List of Figures

List of Tables

Abbreviations

4MOST	**4**-metre **M**ulti **O**bject **S**pectroscopic **T**elescope
AllWISE	**A**ll-sky **W**ide **I**nfrared **S**urvey **E**xplorer
ASKAP	**A**ustralian **S**quare **K**ilometre **A**rray **P**athfinder
CMB	**C**osmic **M**icrowave **B**ackground
DECaLS	**D**ark **E**nergy **C**amera **L**egacy **S**urvey
DECam	**D**ark **E**nergy **C**amera
DESI	**D**ark **E**nergy **S**pectroscopic **I**nstrument
DQF	**D**ata **Q**uality **F**lag
DR	**D**ata **R**elease
ER	**E**rror **R**ate
FR	**F**anaroff **R**iley
GLEAM	**G**alactic and **E**xtragalactic **A**ll-sky **M**urchison **W**ide-field **A**rray
HzRG	**H**igh **R**edshift **R**adio **G**alaxy
IAU	**I**nternational **A**stronomical **U**nion
ICM	**I**tracluster **M**edium
IR	**I**nfra **R**ed
LOFAR	**L**ow **F**requency **A**rray
LoTSS	**L**OFAR **T**wo-metre **S**ky **S**urvey
LR	**L**ikelihood **R**atio
MCMC	**M**arkov **C**hain **M**onte **C**arlo
MGCLS	**M**eerKAT **G**alaxy **C**luster **L**egacy **S**urvey
NED	**N**ASA/IPAC **E**xtragalactic **D**atabase
NRAO	**N**ational **R**adio **A**stronomy **S**urvey

NVSS	**N**RAO **V**LA **S**ky **S**urvey
RACS	**R**apid **A**SKAP **C**ontinuum **S**urvey
SDSS	**S**loan **D**igital **S**ky **S**urvey
SKA	**S**quare **K**ilometre **A**rray
SNR	**S**ignal to **N**oise **R**atio
USS	**U**ltra **S**teep **S**pectrum
VLBI	**V**ery **L**ong **B**aseline **I**nterferometry
WISE	**W**ide **I**nfrared **S**urvey **E**xplorer

Physical Constants

Speed of Light	c	=	$2.997\ 924\ 58 \times 10^8$ m/s
Hubble constant	H_0	=	70 km/s/Mpc

Symbols

a	cosmic scale factor	
α	spectral index	
χ_r^2	reduced chi-squared	
d	distance	m
I	brightness	$\mathrm{W/m^2}$
γ	lorenz factor	
ν	frequency	Hz
ν_o	reference frequency	Hz
S_ν	flux desnsity	Jy
$\mathrm{M}_\odot$	solar mass	$1.988416 \times 10^{30}\,\mathrm{kg}$
v	velocity	m/s
θ	angle	$^\circ$
z	redshift	
$Ly-\alpha$	Lyman-alpha	
$''$	arcseconds	arcsec

Dedicated to my beloved mother, Alice Macandja, whose unwavering sacrifices and boundless love have shaped and inspired Yola, Otília, and me.

Chapter 1

Introduction

Redshift is a key concept in cosmology and astronomy. It occurs when electromagnetic radiation emitted or reflected by an object shifts towards the lower energy end of the spectrum. This phenomenon is crucial for studying the properties of galaxies and gaining insights into the broader structure of the Universe. Theories regarding cosmological redshift emerged in the 19th century along with the development of wave mechanics and the exploration of phenomena associated with the Doppler effect. In 1848, the French physicist Fizeau was the first to describe the Doppler redshift, linking the shift in spectral lines observed in stars to the Doppler effect. Subsequently, in 1868, the British astronomer Huggins became the first to apply this method to measure the velocity of a star moving away from Earth (Huggins, 1868). In 1901, Belopolsky verified optical redshift in the laboratory using a system of rotating mirrors (Bélopolsky, 1901).

Later, Hubble discovered an approximate relationship between the redshift of the nebulae and their distance. This relationship became known as Hubble's Law (Hubble, 1929). This law states that the velocity at which a galaxy is receding from the observer is directly proportional to its distance from the observer. These observations supported Friedmann's work, in which he derived the Friedmann equations (Friedmann, 1924, cited by Nemiroff and Patla, 2008). These equations describe the expansion of space in homogeneous and isotropic models of the Universe within the framework of general relativity. They are considered the first observational foundation for the expanding Universe paradigm and are now among the most frequently cited evidence supporting the Big Bang theory.

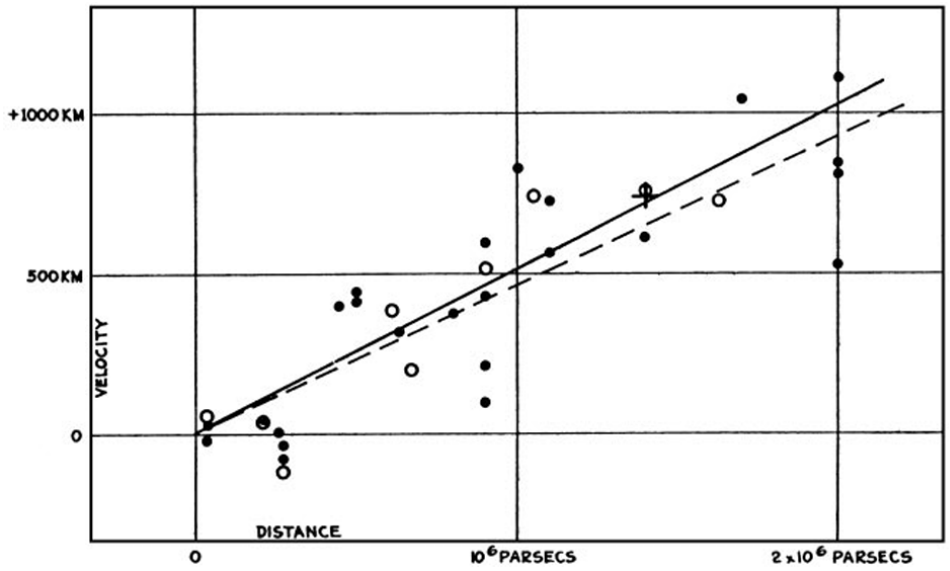

FIGURE 1.1: Galaxy recession velocity versus distance, showing the velocity-distance relationship of extragalactic nebulae. Black discs with a solid line represent the solar motion solution for individual nebulae, while circles and a dashed line indicate the grouped solution. The cross marks the mean velocity at the average distance of 22 nebulae with undetermined velocities, illustrating the evidence for the expansion of the Universe, with the slope representing the Hubble constant, indicating the rate of this expansion. Image source: Hubble (1929).

1.1 Hubble's Law and the Expansion of the Universe

Hubble provided the foundational evidence for one of the most important scientific discoveries of the twentieth century: the expanding Universe (Hubble, 1929). He demonstrated that galaxies are moving away from us in all directions, with those further away receding at a faster rate. Figure 1.1 represents the original Hubble diagram of velocity versus distance. The equation that describes the linear relationship in this graph is known as Hubble's Law:

$$v = H_0 \times d; \tag{1.1}$$

where v is the recession velocity of the galaxy (km/s), d is the distance to the galaxy (Mpc) and H_0 is the Hubble constant (km/s/Mpc).

For galaxies receding due to the expansion of the Universe, the recession velocity can be given as $v = c \times z$, where c is the speed of light and z is the redshift. In this case, the velocity is a fraction of the speed of light, and this expression resembles the Doppler shift. For relatively near objects, the relationship $v = c \times z = H_0 \times d$ illustrates the connection between H_0 and the redshift: $z = H_0 \times d/c$. Here, redshift is a dimensionless quantity, and the ratio H_0/c has units of distance.

The Hubble Law provides direct evidence for the expansion of the Universe. This expansion implies that the Universe was denser and hotter in the past, leading to the formation of galaxies in the early epochs after the Big Bang. By observing galaxies at increasing distances, corresponding to higher redshift, we can effectively look back in time and study how galaxies evolved in these early stages of the Universe's history.

1.2 Probing the High-Redshift Universe

The high-redshift Universe has been a focal point in cosmology and galaxy evolution studies, providing insights into the earliest stages of galaxy formation and the large-scale structure of the cosmos. At $z = 2 - 4$, we observe the peak of star formation activity and the emergence of structural patterns similar to those found in the local Universe (Shapley, 2011). Multi-wavelength deep-field surveys have been used to detect and study galaxies throughout cosmic history, enabling measurements of star formation rates and stellar masses (Salmon et al., 2015; Dickinson, 2016). Each of the different wavebands used in surveys to study the high-redshift Universe offers unique benefits and faces specific limitations.

1.2.1 Optical Surveys

Optical surveys have proven invaluable for probing the high-redshift Universe. The *Hubble Frontier Fields* programme[1] combines space telescope capabilities with gravitational lensing to detect galaxies at $z \sim 6$–8, allowing estimates of luminosity functions down to faint magnitudes (Atek et al., 2014). Ground-based telescopes such as *Subaru*[2] (Kaifu, 1998) have also contributed significantly, with surveys targeting Lyman-α emitters and Lyman break galaxies (Rhoads et al., 2001; Steidel et al., 2003; Iye, 2008). The *Euclid* mission[3] surveys large areas with high resolution in optical and near-infrared, potentially detecting Lyman-α emitters and quasars at $6.5 < z < 9.7$ (Mellier et al., 2024).

Despite these advantages, dust extinction significantly impacts the detection of distant galaxies at optical wavelengths, leading to potential biases in our understanding of the early Universe. Furthermore, as the redshift increases, the rest-frame ultraviolet (UV) emission of galaxies shifts out of the optical range, making it difficult to observe the

[1] https://frontierfields.org/about/
[2] https://www.naoj.org/Projects/Subaru/
[3] https://www.esa.int/Science_Exploration/Space_Science/Euclid

most distant objects (Kaviraj et al., 2008). Studies have shown that traditional colour selection techniques can miss up to 50% of luminous star-forming galaxies at $z \sim 2$ due to dust reddening (Daddi et al., 2004; Riguccini et al., 2011). These galaxies can have star formation rates exceeding 100 solar masses per year, contributing significantly to the cosmic infrared background (Cochrane, 2019).

1.2.2 Infrared Observations

Infrared surveys, like the *Wide-field Infrared Survey Explorer* (WISE)[4] (Wright et al., 2010) and the *Spitzer Space Telescope*[5] (Werner et al., 2004), have helped overcome some of the limitations of optical observations by detecting thermal emission from dust-enshrouded star-forming galaxies (Stern et al., 2012). The longer wavelengths of infrared light allow these instruments to peer through dust, revealing heavily obscured objects that optical surveys miss.

Recent *James Webb Space Telescope* (JWST)[6] (Gardner et al., 2023) observations have revealed numerous high-redshift galaxies, pushing our understanding of the early Universe. Photometric analysis of the SMACS0723 field has uncovered galaxy candidates up to $z \sim 16$, demonstrating extremely blue UV slopes and rapid stellar mass build-up (Atek et al., 2023). Analysis of 341 galaxies at $5 < z < 14$ shows a size-stellar mass relation similar to $z \sim 3$ galaxies but scaled down in size, with some sources exhibiting high star formation surface densities (Morishita et al., 2024). These findings demonstrate JWST's capability to uncover robust photometric candidates at high-redshift, providing crucial insights into the formation epoch of the first galaxies. However, infrared selection methods are still limited and can miss a significant fraction of galaxies, particularly at high-redshift, as they are limited by confusion noise, dust obscuration although less affected than optical surveys, and foreground obscuration (Blecha et al., 2018; Talia et al., 2021; Shen et al., 2022).

[4] https://www.jpl.nasa.gov/missions/wide-field-infrared-survey-explorer-wise/
[5] https://science.nasa.gov/mission/spitzer/
[6] https://science.nasa.gov/mission/webb/

1.2.3 X-ray Observations

X-ray observations from telescopes such as the *Chandra X-Ray Observatory*[7] (Weisskopf et al., 2000) and *X-Ray Multi-Mirror Mission (XMM-Newton)*[8] (Jansen et al., 2001) are excellent at detecting galaxies with active galactic nuclei (AGN) and massive galaxy clusters at high-redshift (Brandt and Hasinger, 2005; Brandt and Vito, 2017). These surveys effectively detect AGN, investigate their physical processes, and reveal their demographics across cosmic time (Brandt and Vito, 2017; She et al., 2017; Viitanen et al., 2019). X-ray detected galaxy clusters currently define the extended structure frontier at z ∼1.4-1.6. XMMU J0044.0–2033 at $z = 1.579$ is the most distant and luminous cluster selected by X-rays known (Santos et al., 2011). In contrast, X-ray selected AGN extend to considerably higher redshifts, with deep Chandra surveys uncovering $\sim$ 100 AGN in the z = 3-6 range and broader catalogues, including eROSITA, pushing to $z \geq 6$ (Natarajan et al., 2024). Most remarkably, the quasar hosted by UHZ1 at $z \sim 10.1$, detected jointly by Chandra and JWST, currently holds the record as the highest-redshift X-ray detected source known (Natarajan et al., 2024). X-rays penetrate dust, making them invaluable for probing the energetic cores of distant galaxies. However, X-ray surveys are generally limited to detecting the most extreme and luminous galaxies (Vito et al., 2018; Wang et al., 2023), and they struggle to trace the broader population of galaxies that are less active or in earlier evolutionary stages (LaMassa et al., 2009).

1.2.4 Radio Observations

In contrast to optical, infrared, and X-ray wavebands, radio observations are unaffected by dust extinction, making radio astronomy particularly well-suited for studying the high-redshift Universe. Radio waves pass through dusty regions unimpeded, allowing observations of galaxies even when they are heavily obscured by dust, making the radio regime the most efficient band to probe the high-redshift Universe (Ishwara-Chandra et al., 2010; Wang et al., 2013; Behiri et al., 2024). In the radio regime, the high-redshift Universe can be explored by studying high-redshift radio galaxies (HzRGs). However, creating complete samples of HzRGs is challenging due to their rarity and the difficulty in identifying them (De Breuck et al., 2001). The common use of an ultrasteep-spectrum (USS) criterion to identify the HzRGs biases samples toward only the most extreme, steep-spectrum objects, excluding those with flatter spectra, leading to an incomplete representation of

[7] https://chandra.harvard.edu/
[8] https://www.cosmos.esa.int/web/xmm-newton

the overall HzRG population (Jarvis et al., 2004; Broderick et al., 2007; Singh et al., 2014; Capetti and Balmaverde, 2024). Precise redshift measurements frequently rely on optical/near-infrared spectroscopy, but heavy internal dust obscures key emission lines and leads to spectroscopic incompleteness, making it difficult to confirm the redshift of these galaxies (Simpson et al., 2004; Casey et al., 2017). At $z > 3$, the increasing energy density of the cosmic microwave background (CMB) intensifies inverse Compton losses in extended lobes, quenching their synchrotron emission and causing even powerful radio sources to fall below survey detection thresholds, potentially biasing surveys against high-z radio-loud AGN (Ghisellini et al., 2014; Wu et al., 2017; Hodges-Kluck et al., 2021). Addressing these limitations requires the integration of wideband radio surveys spanning from a few hundred MHz to several GHz, combined with multi-wavelength follow-up to overcome the selection bias and dust obscuration and CMB quenching effects.

HzRG searches have been carried out over both contiguous and non-contiguous survey footprints. For example, De Breuck et al. (2000) compiled 669 HzRG candidates across a contiguous area of $\sim$ 30,000 deg^2 outside the Galactic plane. Both De Breuck et al. (2004) and Broderick et al. (2007) used the same dataset pairing the 843 MHz Sydney University Molonglo Sky Survey (SUMSS) matched to the 1.4,GHz NRAO VLA Sky Survey (NVSS), and each identified 76 candidates across a $\sim$ 360 deg^2 footprint. By contrast, Schmidt et al. (2006) adopted an optically non-detected selection in the Sloan Digital Sky Survey (SDSS) to pick out 96 HzRG candidates over a non-contiguous total area of only $\sim$ 2.4 deg^2. More recently, Saxena et al. (2018b) used the full Tata Institute of Fundamental Research Giant Metrewave Radio Telescope Sky Survey (TGSS) footprint, across a contiguous total sky area of 36,900 deg^2 (Intema et al., 2017), for the discovery of TGSS J1530+1049 at $z = 5.72$.

New and upcoming facilities will substantially improve counterpart identification, redshift confirmation, and sample completeness. JWST's near-infrared imaging and spectroscopy make it possible to obtain robust identifications and spectroscopic redshifts for faint, dust-obscured radio sources (Kokorev et al., 2023). The Vera Rubin Observatory will provide deep, wide-field optical photometry that is ideal for counterpart matching, photometric redshifts and target selection (Ivezić et al., 2019). MeerKAT's combination of high sensitivity, fine angular resolution and wide fractional bandwidth enables μJy-level detections, in-band spectral-index measurements and detailed polarimetric and morphological characterisation, which together improve candidate selection and classification (Knowles et al., 2022). Finally, the Square Kilometre Array[9] (SKA) will deliver the survey speed

[9] https://www.skao.int/en/explore/science-goals

and sensitivity needed to detect radio-loud quasars well into the reionisation era and to enable 21-cm forest experiments and large, statistically powerful population studies (Niu et al., 2025). Together, these instruments will markedly increase redshift accuracy and our ability to trace radio-galaxy evolution across cosmic time.

1.3 Radio Galaxies

Radio galaxies are extragalactic objects characterised by strong radio emissions up to 10^{41} erg/s, and are commonly associated with AGN. They can be divided into thermal and non-thermal types based on emission characteristics and accretion properties (Antonucci, 2011). Thermal radio galaxies, which are more frequent at higher radio luminosities, feature hidden quasar nuclei obscured by dusty toroidal structures (Ogle et al., 2006). Non-thermal radio galaxies are often found at lower radio luminosities (Antonucci, 2011), primarily emitting through synchrotron jets (Moffet, 1966). According to the optical spectra, radio galaxies can also be divided into broad-line and narrow-line radio galaxies. Typically, radio galaxies are predominantly associated with elliptical galaxies, particularly those with absolute photographic magnitudes brighter than -20 in blue band (B-band) (Rogstad and Ekers, 1969). Radio galaxies undergo cycles of activity and quiescence, with phases of dying, remnant, and restarted activity integral to their life cycle (Jurlin et al., 2020; Morganti, 2024).

Radio astronomy became a crucial tool in observational cosmology after the discovery that Cygnus A is associated with a faint and distant galaxy (Baade and Minkowski, 1979). By 1960, redshifts of $z = 0.45$ were measured for galaxies linked to radio sources (Minkowski, 1960). Two breakthroughs occurred towards the end of 1962: first, quasistellar radio sources or "quasars" were discovered (Schmidt, 1963), with much larger redshifts than radio galaxies (Kellermann, 2014). Second, it was shown that the space density of radio sources varies with the cosmic epoch (Davidson, 1962).

The radio frequency spectra and polarisation properties of radio galaxies and quasars indicate synchrotron radiation, which originates from relativistic electrons with a power-law distribution of energies. These electrons have a Lorentz factor of about 1000 and exist in a magnetic field with a strength of approximately 10^{-5} Gauss (Duffy and Blundell, 2012). Radio emission from extragalactic sources can be categorised into extended and compact structures. Extended structures are typically transparent and exhibit asymmetric brightness distributions in luminous, core-dominated sources, possibly due to relativistic

Doppler enhancement (Perley et al., 1982). Compact structures, on the other hand, are opaque due to a high relativistic electron density. These compact sources often display flat radio spectra, which can be explained by multiple discrete components with correlated magnetic fields and electron distributions (Marscher, 1977). There is no straightforward correlation between the size of the radio-emitting region and the size of the associated optical galaxy or quasar, although statistical differences are observed (Singal and Singh, 2013). Typically, compact sources are linked to quasars or AGN; however, less intense compact sources can also be found in seemingly normal elliptical galaxies (Ekers, 1978). Extended sources are usually associated with galaxies, but many are quasars with no visible optical counterpart. Most extended sources, especially quasars, reveal a compact central radio component when observed with high sensitivity and resolution; these central components are particularly notable in quasars (Owen and Puschell, 1984).

The population of radio galaxies can be divided into two primary categories: star-forming galaxies and radio-loud AGNs (Bonzini et al., 2012). In star-forming galaxies, radio emission is primarily driven by synchrotron radiation from supernova shocks and free-free emission from ionised hydrogen regions, establishing a direct link between radio luminosity and star formation rate (Condon, 1992). Radio-loud AGNs generate radio emissions solely from non-stellar processes driven by particles accelerated by the core of the AGN and are much more powerful and primarily located in elliptical galaxies, compared to star-forming galaxies (Condon, 1992; Sadler et al., 2002; Best et al., 2005).

Radio galaxies and quasars exhibit various radio morphologies, ranging from compact sources to extended structures spanning megaparsecs (Dabhade et al., 2023). Extended sources are traditionally classified as Fanaroff-Riley (FR) type I and II, while compact sources often display core-jet or equal double morphologies (Readhead and Pearson, 1982; Miraghaei and Best, 2017). High-resolution imaging uncovers various nuclear features, such as core-jet configurations and symmetric double-lobed structures (Readhead and Pearson, 1982). Jets in radio galaxies and quasars can span from sub-parsec to hundreds of kiloparsecs, interacting with the interstellar medium and potentially impacting star formation and galaxy evolution (Saikia, 2022). Statistical models indicate that quasars are typically observed within 50° of the source axis, while radio galaxies are viewed at larger angles, aligning with unified models of AGN (Lister et al., 1994). These varied structures and orientations enhance our understanding of the evolution and the connection between radio galaxies and quasars.

In many instances, the morphology of radio galaxies and quasars is too intricate to distinguish between the various observed features, and not all features are present in every

object. However, the most commonly observed properties include:

- Cores: compact, unresolved components commonly found in radio galaxies, particularly in quasars. Preston et al. (1983) identified milli-arcsecond scale cores in 80% of quasars and 10% of galaxies at 2.3 GHz. These cores frequently exhibit flat or inverted spectra, likely caused by synchrotron self-absorption (Broderick and Condon, 1975; Morganti et al., 1997). The ratio of core to extended flux, known as core dominance, varies between different types of sources and serves as an indicator of orientation in unified models of AGN (Morganti et al., 1997).

- Jets: powerful, highly collimated outflows extending from parsec to kiloparsec scales. Very Long Baseline Interferometry (VLBI) observations reveal complex structures and superluminal motions in jets on parsec scales (Zensus, 1997). The well-studied jet of M87 displays a filamentary structure and proper motions ranging from $0.1c$ to $0.7c$ at both parsec and kiloparsec scales (Biretta and Meisenheimer, 1993). Optical and radio polarimetry of the M87 jet at $0.2''$ resolution reveals highly ordered magnetic fields, with polarisation reaching up to 50% in certain regions (Perlman et al., 1999). The magnetic field is typically aligned with the jet axis but becomes perpendicular in shock-like knots. Multi-wavelength polarisation VLBI studies of AGN jets suggest the presence of helical magnetic fields, possibly generated by the combined rotation of the central black hole, accretion disk, and jet outflow (Gabuzda, 2015).

- Lobes: are large-scale structures linked to AGN, often forming pairs on opposite sides of the central source. The opening angle between these lobes can range from 180^o in classical double sources to much narrower angles in narrow-angle-tail radio galaxies (Arshakian et al., 2000). Bent lobes are more common in dense environments, with 78% of double-lobed radio galaxies exhibiting bent morphologies within 1 Mpc of cluster centres, compared to just 29% in the field (Silverstein et al., 2017). This bending is thought to result from ram pressure as the AGN moves through the intracluster medium (ICM) (Sakelliou and Merrifield, 2000; Silverstein, 2015). Wide-angle-tail sources, a specific type of bent radio source, are typically found in the brightest cluster galaxies of merging clusters and can act as indicators of cluster mergers (O'Dea and Baum, 2023). The extent of bending in radio lobes provides insights into ICM density and the velocity of the host galaxy (Silverstein, 2015).

- Hotspots: regions of intense emission located at the edges of radio lobes, formed by the interaction of jets with the intergalactic medium. These hotspots often exhibit

multiple knots and areas of diffuse emission, suggesting complex particle acceleration mechanisms (Prieto et al., 2002). The origin of secondary hotspots remains unclear, but they may represent expanding, fading structures (Pyrzas et al., 2015). X-ray emission in hotspots and knots is produced through diverse mechanisms, with some cases requiring inverse Compton scattering models to account for the observations. Hotspots typically exhibit smaller Doppler factors and larger co-moving magnetic fields compared to knots, reinforcing the idea that hotspots mark the jet termination points, while knots are features within the collimated jets. The differences between hotspots and knots likely arise from variations in Doppler boosting and magnetic field strengths (Zhang et al., 2010).

A recent observation of the nearby elliptical radio galaxy IC 4296 using MeerKAT's 1.28 GHz continuum image (Figure 1.2) has revealed new and intriguing morphological features in its large, low-luminosity radio source, which spans 510 kpc (Condon et al., 2021). The image, with its enhanced brightness sensitivity, dynamic range, and angular resolution, uncovered features referred to as *threads*, *ribbons*, and *rings*. The threads are faint, narrow emissions that form when helical Kelvin-Helmholtz instabilities disrupt the galaxy's main radio jets. The ribbons are smoother regions between the jets and lobes, likely remnants of earlier jet activity that have settled into pressure equilibrium. Additionally, vortex rings and backflows in the outer lobes indicate that the straight outer jets and ribbons are inclined by roughly 60° from our line of sight, a finding supported by photometric, geometric, and gas-dynamical measurements near the galaxy's nucleus.

1.4 High-Redshift Radio Galaxies

HzRGs are powerful radio sources hosted by massive forming galaxies, often found in overdense regions and surrounded by protoclusters (Miley and De Breuck, 2008), and are of particular interest due to their potential to provide insights into the formation and evolution of galaxies (van Breugel et al., 1999). They are also often found to be associated with clusters of galaxies at $z \sim 2 - 5$ (Stevens et al., 2003; Belsole et al., 2004; Galametz et al., 2012). It has been suggested that HzRGs are likely to be massive, with recent studies showing that HzRGs at $z \sim 4$ have average stellar masses of $\sim 4.2 \times 10^{11}\,\mathrm{M}_{\odot}$ (Yamamoto et al., 2025), and formed early in the Universe's history and are thought to be the progenitors of massive ellipticals (Röttgering et al., 1999). HzRGs are dominated

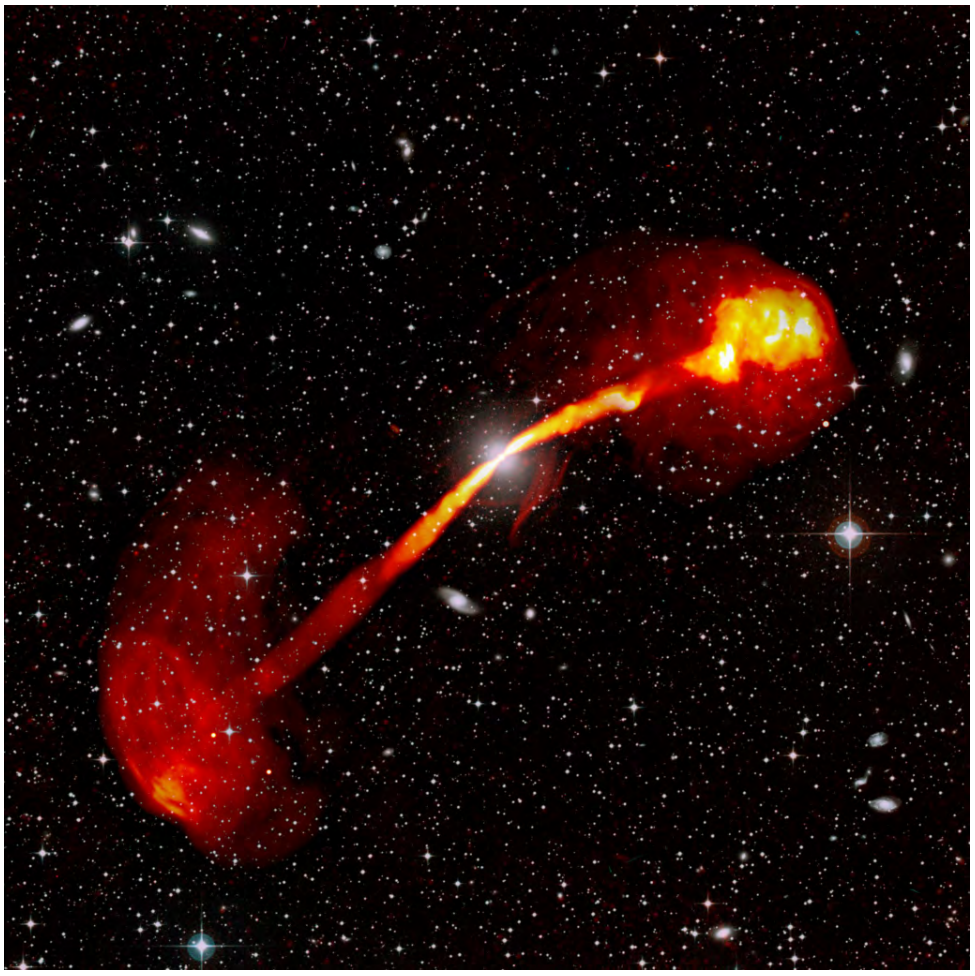

FIGURE 1.2: IC 4296 radio galaxy. MeerKAT radio data are shown in red/orange, while the SuperCOSMOS Sky Survey provides the visible light image, displaying the central giant elliptical galaxy, unrelated galaxies, and Milky Way stars. Credit: SARAO. Adapted from Condon et al. (2021).

by an old stellar population and are seen to have high star formation rates (Miley et al., 2006; Rocca-Volmerange et al., 2013).

Over the years, the highest redshift recorded for a known radio galaxy has steadily risen. Spinrad (1982) was the first to identify a radio galaxy beyond $z \sim 1$. Stern et al. (1999) identified 15 radio galaxies with z mostly above 1.5. De Breuck et al. (2000) described the construction of 669 USS radio sources (defined by $\alpha < -1.3$)[10], finding only 15% detectable in optical surveys. Spectroscopic follow-up of 62 objects in this sample revealed redshifts ranging from $z = 0.25$ to $z = 5.19$, including ten sources at $z > 3$. Cai et al. (2002) later used Very Long Baseline Interferometry (VLBI) observations to study three HzRGs at $z > 2$, revealing asymmetric structures.

[10]In the relation $S_\nu \propto \nu^\alpha$, where S_ν is the flux density at frequency ν and α is the spectral index.

More recently, Orenstein et al. (2019) expanded the catalogue of infrared-faint radio sources with known redshift to 131, with a median redshift of $z = 2.68$. Saxena et al. (2019) studied 13 faint radio galaxies with $0.52 < z < 5.72$, finding lower Lyman-α luminosities, narrower line widths, and lower stellar masses compared to brighter HzRGs, implying that faint HzRGs might represent a transitional population between star-forming galaxies and narrow-line AGNs. Broderick et al. (2022) refined HzRG selection techniques using low-frequency radio spectra and near-infrared data, identifying 51 new candidates, including one at $z = 5.55$ and another potentially at $z \sim 8$. The highest redshift radio galaxy known to date is at $z = 5.72$ (Saxena et al., 2018b).

The definition of "high-redshift" may differ slightly based on the scientific objectives and the observational context, but $z > 2$ is commonly considered the standard threshold for HzRG studies (McCarthy et al., 1990; Miley and De Breuck, 2008; Herzog et al., 2014; Saxena et al., 2018b). In this study, we also adopt $z > 2$ as the definition of high-redshift, since it corresponds to the first billion years after the Big Bang (Stark, 2016), extends beyond the peak of the star formation rate density (Bunker et al., 2006), and overlaps with the epoch of reionization ($z > 6$) (Fan, 2012).

1.4.1 The Redshift-Spectral Index Relation

The relation between z and α describes the observed trend, which is that radio galaxies with steeper spectral indices tend to be located at higher redshift. This relation has been known for many years and has been widely used to identify HzRGs candidates (Gopal-Krishna, 1988; Krolik and Chen, 1991; Bechtold et al., 1984; Carilli and Yun, 2000; De Breuck et al., 2001). Although the $\alpha - z$ correlation is useful, what causes the relation is still under debate. Inverse Compton losses, driven by the increased energy density of the CMB, were initially proposed as an explanation (Krolik and Chen, 1991). A study by Ker et al. (2012) highlighted that environmental differences, such as a denser intergalactic medium at a higher redshift, could also contribute to this steepening. They further noted the impact of sample selection effects and measurement frequencies, emphasising that while steep-spectrum selection can increase the proportion of high-redshift sources in samples, they may exclude a substantial number of such objects. Recent work by Morabito and Harwood (2018) confirmed that inverse Compton losses combined with selection effects could largely reproduce the observed correlation, reinforcing the complexity of the relationship between the spectral index and redshift.

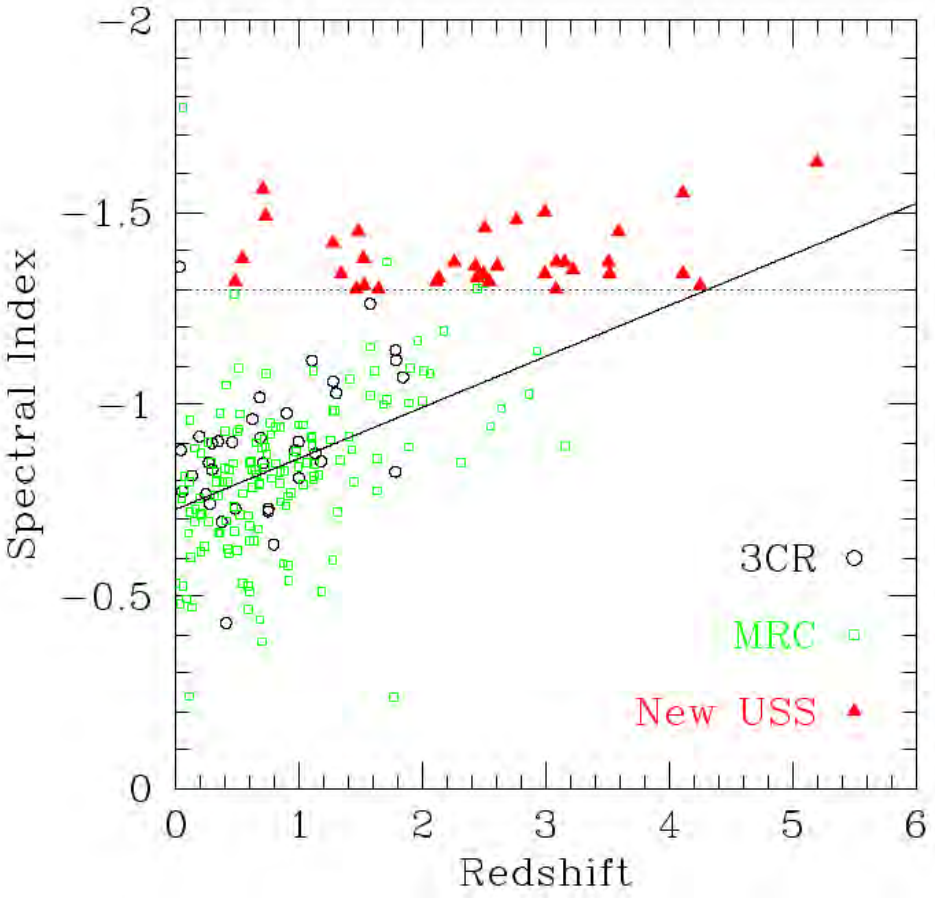

FIGURE 1.3: The empirical correlation between spectral index and redshift. The more distant radio galaxies have steeper spectra. The horizontal dotted line indicates the $\alpha < -1.3$ cut-off. Image source: De Breuck et al. (2001).

There is no uniform definition for a USS source in the literature, and different studies have used different frequencies and different spectral index thresholds, e.g. $\alpha^{4.85\,\mathrm{GHz}}_{151\,\mathrm{MHz}} \leq -0.981$ (Blundell et al., 1998), $\alpha^{325\,\mathrm{MHz}}_{74\,\mathrm{MHz}} \leq -1.2$ (Cohen et al., 2004), $\alpha^{843\,\mathrm{MHz}}_{408\,\mathrm{MHz}} \leq -1.3$ (De Breuck et al., 2004), $\alpha^{1.4\,\mathrm{GHz}}_{151\,\mathrm{MHz}} \leq -1.0$ (Cruz et al., 2006), $\alpha^{1.4\,\mathrm{GHz}}_{150\,\mathrm{MHz}} \leq -1.0$ (Ishwara-Chandra et al., 2010). USS radio sources are often associated with distant galaxies and extreme cosmic phenomena (Argo et al., 2013). Figure 1.3 shows a study by De Breuck et al. (2001) who presented an empirical correlation between radio spectral steepness and redshift, using a sample of 669 USS sources.

Although the USS criterion does not exclusively select high-redshift galaxies, since some low-redshift sources can also exhibit steep spectra, it has nonetheless been effective in identifying the largest number of HzRG candidates (De Breuck et al., 2001; Saxena et al., 2019). When the USS criterion is combined with multi-wavelength cross-matching, it can lead to the identification of reliable HzRG candidates (De Breuck et al., 2000; Pedani, 2003; Saxena et al., 2018b).

1.5 Thesis Motivation and Outline

Understanding the formation and evolution of massive galaxies in the early Universe is essential for refining models of large-scale structure and galaxy evolution (De Breuck et al., 2002). HzRGs offer a unique perspective on these processes, as they are among the most massive galaxies in the Universe, often associated with supermassive black holes and intense star formation activity (Rocca-Volmerange et al., 2004). These characteristics make HzRGs valuable tracers of the dense environments in the early Universe.

Despite their importance, identifying HzRGs remains a significant challenge due to their rarity and the difficulties in detection. As of 2018, fewer than 200 HzRGs were known (Morabito and Harwood, 2018). Recent advances in radio astronomy, particularly through surveys such as the MeerKAT Galaxy Cluster Legacy Survey (MGCLS; Knowles et al., 2022), have demonstrated the potential to expand this sample. For instance, Knowles et al. (2021) identified 274 HzRG candidates in the Abell 2751 field from the MGCLS, detecting sources with flux densities as low as 57 μJy at 1.28 GHz. This represents an order of magnitude improvement over previous studies at similar frequencies.

Building on this foundation, this thesis aims to extend the search for HzRG candidates to multiple MGCLS fields with image quality similar to Abell 2751. By taking advantage of the wideband nature of the MeerKAT, we also aim to investigate the usefulness of in-band spectral information of the MeerKAT data, where previous studies had to use multi-band data.

This thesis is structured as follows: In Chapter 2, we introduce the radio and multi-wavelength data used in this study, describe the sample selection, and the multi-stage methodology employed to identify HzRG candidates. Chapter 3 presents the results of the HzRG search and discusses the implications. In Chapter 4, we use the in-band spectral index measurements determined in Chapter 2 to test the limitations of the canonical spectral index assumptions used in the literature for flux density extrapolation. Chapter 5 provides a summary and concluding remarks.

Throughout this work, we assume a flat ΛCDM cosmology with $H_0 = 70\,\mathrm{km/s/Mpc}$ and $\Omega_m = 0.3$. We also adopt a power-law of the form $S_\nu \propto \nu^\alpha$, where $\alpha < 0$ denotes a steep-spectrum source (and $\alpha < -1$ an ultra steep-spectrum source), $\alpha \approx 0$ a flat-spectrum source, and $\alpha > 0$ an inverted spectrum source.

Chapter 2

Sample Selection and Methodology Overview

Our search for HzRGs employs a multiwavelength methodology utilising radio data from the MeerKAT, near/mid-infrared data from the WISE and optical data from the Dark Energy Camera (DECam). We first describe the data products of each survey, then the construction of our full sample that we use for our HzRGs candidates search. After selecting the MGCLS fields that are best suited for our search, we present the multistage filtering process that refines each field down to its final set of HzRG candidates. We show each step using the Abell 22 field as a representative case. Abell 22 was randomly selected for the sake of demonstration, and the same steps were applied to the rest of the sample.

2.1 Data Sources

MGCLS provides wideband radio data covering a ∼700 MHz range (fractional bandwidth of 0.55). The Dark Energy Camera Legacy Survey[1] (DECaLS) provides optical data (g, r, z bands to ∼24 AB mag), while the All-sky Wide Infrared Survey Explorer[2] (AllWISE) provides infrared measurements (3.4–22 μm at mJy sensitivities) for multi-wavelength cross-matching.

[1] https://www.legacysurvey.org/decamls/
[2] https://wise2.ipac.caltech.edu/docs/release/allwise/

FIGURE 2.1: Aerial view of the MeerKAT radio telescope (credit: SARAO).

2.1.1 Radio data: MGCLS

The MGCLS consists of long-track (6–10 hours) observations of 115 galaxy clusters using MeerKAT's L-band (856–1712 MHz) receiver. MeerKAT comprises 64 offset Gregorian parabolic dishes, each with a diameter of 13.5 m. Approximately 75% of these antennas are concentrated within a compact core region with a diameter of ∼1 km, shown in Figure 2.1, featuring the shortest baseline of 29 m. The remaining dishes extend outward, resulting in a maximum baseline of 8 km. Each of MeerKAT's antennas is currently equipped with receivers that cover the UHF-band (544–1088 MHz), L-band and S-band (1750–3500 MHz) (Jonas and MeerKAT Team, 2016).

The MGCLS has produced a wealth of data, including radio visibilities, calibrated image cubes, and catalogues of compact and diffuse sources. Figure 2.2 shows the distribution of the observed galaxy clusters in the Southern sky with declinations ranging from −85 to 0 degrees. Each MGCLS field covers a sky area of $\sim 1.2^\circ \times 1.2^\circ$ after primary beam correction, with a typical central RMS noise of 4–6 μJy beam^{-1} in full resolution (FWHM $\approx 7.5''$–$8''$). With 115 non-contiguous fields in the southern sky, this results in a total surveyed sky area of approximately 165.6 deg^2 in the southern sky. An excerpt of these clusters is provided in Table 2.1 with the right ascension and declination corresponding to the MeerKAT observations, taken from Table 1 from Knowles et al. (2022).

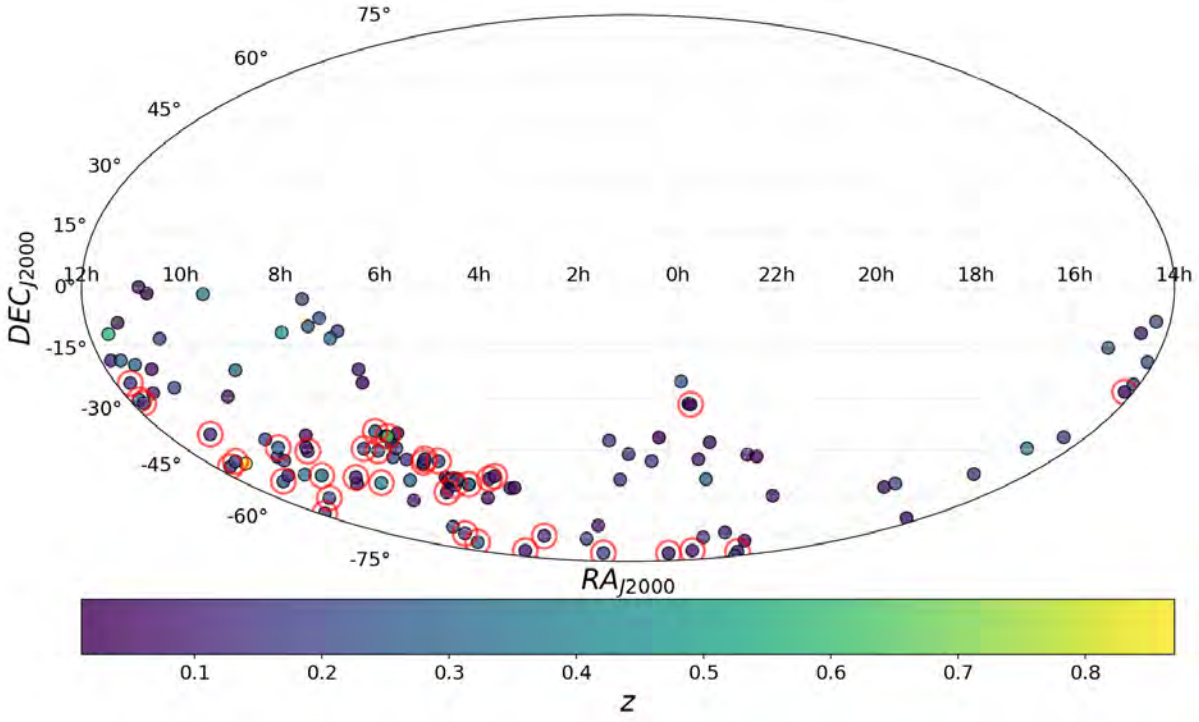

FIGURE 2.2: Sky distribution of the 115 MGCLS cluster fields. The red circles indicate the fields selected for our HzRG search (see Section 2.2).

2.1.1.1 MGCLS Data Products

The first data release (DR1) of the MGCLS provides a range of data products, including uncalibrated visibilities, continuum imaging products, and multiple source catalogues made available with the paper by Knowles et al. (2022). Each galaxy cluster in the survey includes Stokes-I products, while approximately 40% also have Stokes-Q and U products. All DR1 legacy products can be accessed via the MGCLS-SARAO website[3], and the raw visibilities are available on SARAO's Archive Server[4] with the project ID "SSV-20180624-FC-01".

In this study, we use the MGCLS compact source catalogue compiled from the MGCLS total intensity image by applying the Python Blob Detector and Source Finder (PyBDSF)[5] with 3σ island RMS and 5σ peak RMS thresholds (Knowles et al., 2022). Only sources that were well fitted with a single Gaussian component (PyBDSF types 'S' or 'C') were retained after removal of spurious detections. The full DR1 catalogue[6]

[3] http://mgcls.sarao.ac.za/data-releases/
[4] https://archive.sarao.ac.za/
[5] https://pybdsf.readthedocs.io/en/latest/
[6] https://doi.org/10.48479/7epd-w356

TABLE 2.1: Excerpt of observed cluster sample. (1) Cluster Name; (2–3) MeerKAT pointing: J2000 Right Ascension (R.A.) and Declination (Dec.) in degrees; (4) Cluster redshift; (5–6) Astrometry: corrected mapping (Fix) and positional offsets (Posn), polarisation (Pol.); (7) root mean square (RMS) noise (sigma-clipped standard deviation in μJy beam^{-1}); (8) Data Quality Flag (0: Good, 1: Moderate, 2: Poor, 3: Very Poor); (9) Presence of diffuse cluster emission. Adapted from Knowles et al. (2022).

(1)	(2)	(3)	(4)	(5)		(6)	(7)	(8)	(9)
Cluster Name	**R.A.**	**Dec.**	**z**	**Fix**	**Posn**	**Pol.**	**RMS**	**DQF**	**D.E.**
Abell 13	3.3842	-19.5010	0.094	-	✓	✓	3.5	1	✓
Abell 22	5.1608	-25.7220	0.142	✓	✓	✓	2.9	0	✓
Abell 33	6.779	-19.5067	0.280	-	✓	✓	5.7	1	-
Abell 85	10.4529	-9.3180	0.055	✓	✓	✓	3.3	1	✓
Abell 133	15.6879	-21.8800	0.057	✓	✓	✓	6.7	1	-
Abell 168	18.7908	0.2475	0.045	✓	✓	✓	3.6	2	✓
Abell 194	21.4458	-1.3731	0.018	✓	✓	✓	5.7	1	-
Abell 209	22.9896	-13.5764	0.206	✓	✓	✓	3.6	1	✓
Abell 370	39.9604	-1.5856	0.375	✓	✓	-	6.9	2	✓
Abell 521	73.5358	-10.2442	0.253	-	✓	✓	3.4	0	✓

contains approximately 626,000 sources in all cluster fields. An excerpt is shown in Table **??**. Catalogue columns (detailed in the caption) include integrated flux density, peak brightness, source size, and positions in decimal degrees. The source identifiers follow the designation of the International Astronomical Union (IAU) designation MKTCS JHHMMSS.ss±DDMMSS.s (Knowles et al., 2022).

A number of data quality issues in the DR1 release impact the visibility and images. Many of these effects have been corrected for in the images, as is outlined below.

TABLE 2.2: Excerpt of the MGCLS compact source catalogue at 1.28 GHz. Columns: (1) MGCLS source Name using the IAU designation; (2–3) J2000 R.A. and Dec.; (4) Total integrated Stokes-I flux density at the reference frequency; (5) Peak Stokes-I brightness; (6) Source size: FWHM of the major (s_{max}) and minor (s_{min}) axes; (7) Cluster field of the source. Adapted from Knowles et al. (2022).

(1) **Src. Name**	(2) **R.A.** (deg)	(3) **Dec.** (deg)	(4) $\mathbf{S_{tot}}$ (mJy)	(5) $\mathbf{I_{peak}}$ (mJy/b)	(6) $\mathbf{s_{max}}$ ($''$)	$\mathbf{s_{min}}$ ($''$)	(7) **Field**
J001059.77190940.3	2.7491	-19.1612	0.695	0.669	7.6	7.5	Abell_13
J001059.94190654.9	2.7498	-19.1153	0.113	0.081	9.8	7.8	Abell_13
J001059.14195204.2	2.7464	-19.8679	0.106	0.056	14.2	7.3	Abell_13
J001059.23194540.7	2.7468	-19.7613	0.077	0.045	11.1	8.4	Abell_13
J001059.50192405.3	2.7479	-19.4015	0.050	0.060	8.0	5.8	Abell_13
J002318.34254121.6	5.8264	-25.6894	0.053	0.061	7.4	6.5	Abell_22
J002317.08253627.2	5.8212	-25.6076	0.939	0.827	8.3	7.6	Abell_22
J002318.08253621.5	5.8253	-25.6060	0.073	0.067	8.5	7.1	Abell_22
J002317.47252111.6	5.8228	-25.3532	0.242	0.198	8.6	7.8	Abell_22
J002317.15261532.9	5.8215	-26.2592	0.573	0.156	19.6	10.3	Abell_22

2.1.1.2 Dynamic Range

MGCLS fields containing powerful sources ($I >$ a few hundred mJy beam^{-1}) are often limited by residual artefacts from these bright sources. This issue is pronounced when multiple bright sources are widely separated, as self-calibration struggles to correct direction-dependent effects (Knowles et al., 2022).

Fields with a good dynamic range are those where the radio observations can capture both faint and bright radio sources with minimal interference from bright outliers or image artefacts. In Table 2.1, a column for the Data Quality Flag (DQF) is presented for the dynamic range, where 0 is Good, 1 is Moderate, 2 is Poor, and 3 is Very Poor. For fields with a good dynamic range, the ratio can surpass 10,000:1, depending on the quality of the observations. Fields with a good dynamic range are crucial for searching for HzRGs because they allow for the detection of both faint and bright radio signals in the same field of view and ensure reliable flux measurements across the band.

2.1.1.3 Astrometric Accuracy

Several instrumental issues impacted the accuracy of the astrometry in the MGCLS data, including the time offset, calibrator position errors, and the low accuracy delay model

in the correlator. To address these issues, Knowles et al. (2022) corrected the image astrometry in each field by aligning the source positions with their respective optical hosts, achieving a final accuracy better than $0.3''$ in regions with a high signal-to-noise ratio (SNR).

Early observations were affected by a 2-second time offset in the data labelling and a half-channel frequency error, both leading to inaccuracies in the u, v, w coordinates. Table 2.1 includes a "Fix" column, indicating cluster fields where these issues were corrected in the visibilities. Fields not corrected may exhibit rotation and scaling errors in source positions, which can be as large as $20''$ at the field edges (Knowles et al., 2022).

To mitigate positional inaccuracies, Knowles et al. (2022) matched compact radio components with various background quasars, radio galaxies, and star-forming galaxies in each field with DECaLS. For each cluster field, a flux density-weighted average correction was calculated, as indicated in the "Posn" column of Table 2.1, and corresponding adjustments were made to the images. Although residual systematic errors are expected to remain below $0.1''$, individual sources may still exhibit larger errors.

2.1.2 Optical data: DECaLS

The DECaLS is a deep optical imaging survey using the Dark Energy Camera (DECam) on the Blanco 4 m telescope. Covering approximately 9,000 square degrees of the sky in the g, r, and z bands, with positional accuracy of ~ 20 mas, DECaLS aims to support the study of the large-scale structure of the Universe by providing high-quality imaging data for target selection Dey et al. (2019). The purpose of this study is to complement existing spectroscopic data from the Sloan Digital Sky Survey (SDSS). It is designed to provide deep optical imaging for the Dark Energy Spectroscopic Instrument (DESI) project. DECaLS provides deeper and higher quality images than previous surveys, reaching surface brightness levels of 28.5 mag/arcsec^2 for individual galaxies at $0.19 < z < 0.50$ (Li et al., 2022). This improved depth reveals previously unseen features such as spiral arms, weak bars, and tidal structures. The survey data have been used for detailed morphological classifications of galaxies by human volunteers and machine learning algorithms (Walmsley et al., 2022). DECaLS data also show promise for measuring the outer light of massive galaxies as a proxy for dark matter halo mass (Li et al., 2022).

DESI Legacy Imaging Surveys have mapped approximately 14,000 to 16,000 deg^2 of the extragalactic sky in three optical bands (g, r, z) using telescopes at the Kitt Peak and

Cerro Tololo observatories (Dey et al., 2019; Burleigh et al., 2020). DESI uses the imaging data to select targets for its 5-year survey, which aims to measure 35 million spectra of galaxies and quasars from redshift 0.05 to 3.5 (Vargas-Magana et al., 2019). DESI's primary science goals include constraining dark energy and testing General Relativity using Baryonic Acoustic Oscillations and Redshift Space Distortions. The target selection pipeline, `desitarget`, processes and categorises various target types for DESI observations (Myers et al., 2023).

2.1.3 Infrared data: AllWISE

The AllWISE programme builds on the success of the WISE mission (Wright et al., 2010) by merging its data and the post-cryogenic Near-Earth Object Wide Infrared Survey Explorer survey (Mainzer et al., 2006), creating the most comprehensive mid-infrared view of the sky to date. AllWISE delivers new products with enhanced photometric sensitivity, greater accuracy, and improved astrometric precision compared to the 2012 WISE All-Sky Data Release. The WISE is a NASA mission designed to map the entire sky in four mid-infrared bands centred at 3.4, 4.6, 12, and 22 μm (Wright et al., 2010). The spacecraft operates in a sun-synchronous polar orbit, employing a simple and efficient survey approach with a constant rotation rate and scanning mirror mechanism (Mainzer et al., 2006; Wright et al., 2010).

2.2 Sample Selection

To carry out our search, we selected MGCLS fields with good dynamic range (DQF = 0; see Section 2.1.1.2), ensuring accurate recovery of both bright and faint sources, high astrometric accuracy, as well as full spatial coverage from DECaLS and AllWISE. 30 of the observed MGCLS fields meet these conditions and are shown in Table 2.3. The primary beam-corrected image of these fields has low RMS noise and has a resolution of $\sim 7.8''$. In addition, the fields show minimal visual contamination from bright source artefacts. The sky positions of these fields are marked by red circles in Figure 2.2, and correspond to a non-contiguous total sky area of $\sim$43.2 deg^2, with a total of 198,120 compact radio sources.

2.3 Searching for HzRGs

The search for HzRGs has evolved through a range of methodologies, with a significant focus on USS radio sources. One of the early influential approaches, outlined by De Breuck et al. (1998), used a spectral index cut-off of $\alpha < -1.3$ combined with a low flux density cut-off of 10 mJy. Later, Singh et al. (2014) extended the USS criteria to fainter radio sources, discovering potential HzRGs and obscured radio-loud AGN at moderate redshift (ranging from $z \sim 0.03$ to 3.86). Schmidt et al. (2006) introduced an innovative strategy by focusing on bright radio sources without optical counterparts, paired with near-infrared imaging, using the K-z relation to efficiently identify HzRG candidates. More recently, Knowles et al. (2021) used high-sensitivity MeerKAT data, cross-matching radio sources with multi-wavelength catalogues, and applying a spectral index cut-off of $\alpha < -1$ to select HzRG candidates at flux densities lower than previously achieved. Together, these techniques have contributed to discovering multiple spectroscopically confirmed HzRGs, contributing to our understanding of HzRGs and their role in galaxy formation and evolution.

We use a multistage process to identify HzRG candidates, applying sequential selection criteria to generate the final list of candidates. The detailed procedure is demonstrated for the Abell 22 field, randomly chosen for the sake of demonstration, and the same approach is applied to the remaining 29 fields in Table 2.3. Abell 22 is located at a redshift of $z = 0.142$ and is located at R.A. = 00h 20m 38.59s and Dec. = $-25^{o}43'19.2''$. The compact source catalogue contains 6,119 radio sources, making it a data-rich field for exploration.

2.4 Unresolved source selection

HzRGs tend to have smaller angular sizes, typically $\leq 30''$, compared to their low redshift counterparts (Pentericci et al., 2000; Singh et al., 2021). The statistical decrease in the angular sizes of radio sources with increasing redshift has been known for a long time, with studies by Miley (1968); Neeser et al. (1995) and Daly and Guerra (2002) demonstrating this trend. More recently, Morabito et al. (2017) demonstrated that the angular sizes of radio sources tend to decrease with increasing redshift, a trend observed in deep radio observations at low frequencies.

The selection of unresolved sources plays a key role in identifying HzRGs when using lower resolution (lower frequency) data, as it increases the likelihood of detecting HzRGs.

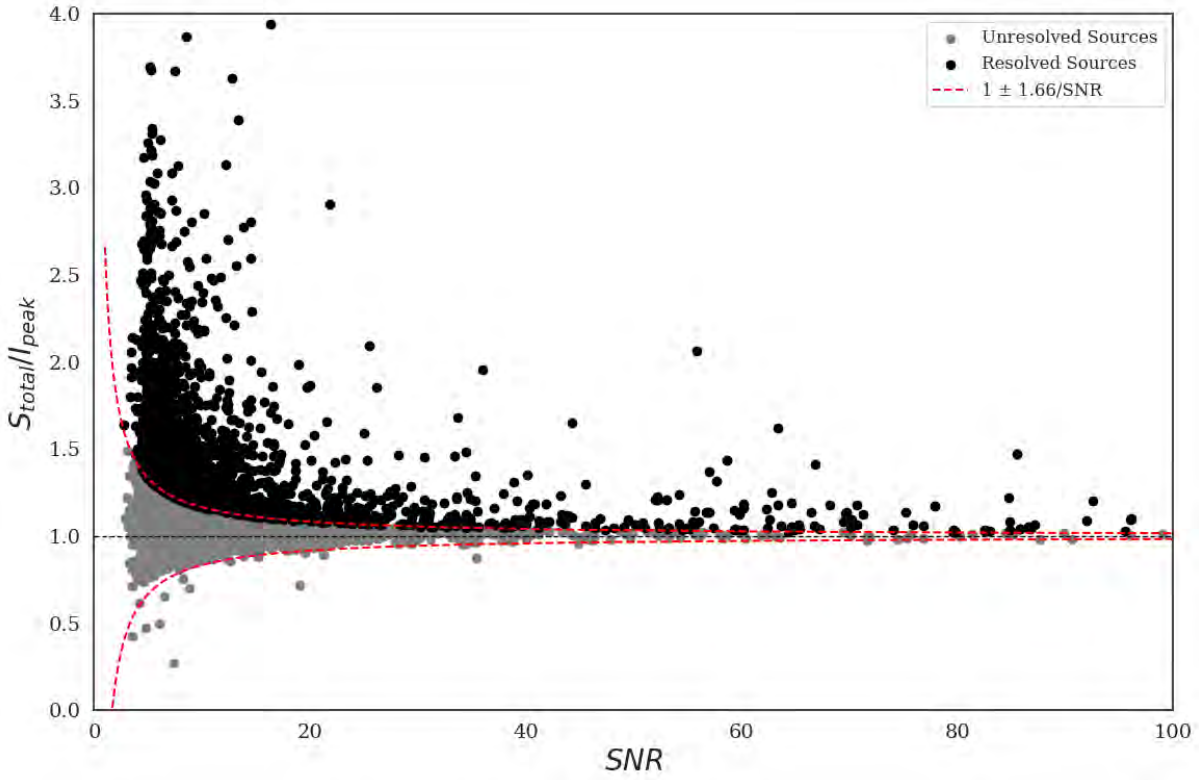

FIGURE 2.3: Ratio of the total flux density to the peak brightness as a function of the source SNR. The horizontal dotted black line indicates the $S_{total} = S_{peak}$ locus. Sources falling below the upper envelope, described by the dotted red curve $1 - 1.66/\text{SNR}$, are considered unresolved.

In order to preferentially select HzRGs, we restrict our catalogue to unresolved sources. The PyBDSF source finding algorithm used to build the radio source catalogue provides the source sizes by fitting one or more two-dimensional elliptical Gaussians to the radio emission. However, the presence of noise peaks around a source can affect the fitted size, particularly in the case of faint sources. To account for these, we used the diagnostic plot of the total-to-peak flux density ratio versus SNR. This method is widely used in studies that involve a large population of faint radio sources (Prandoni et al., 2000; Singh et al., 2018; Ishwara-Chandra et al., 2020).

Unresolved sources are expected to have a ratio $S_{total}/S_{peak} = 1$. However, as shown in Figure 2.3, there is an increasing dispersion around the line $S_{total}/S_{peak} = 1$ for fainter sources. This dispersion is due to the influence of image noise. To account for these noise peaks, a curve defined as $1 - 1.66/\text{SNR}$ is plotted, which envelopes nearly all sources falling below the $S_{total}/S_{peak} = 1$ line. The reflection of this curve around $S_{total}/S_{peak} = 1$, defined as $1 + 1.66/\text{SNR}$, is also plotted to address the uncertainties introduced by the positive noise peaks. To obtain the curve, the data were binned by SNR, and for each bin, the lower envelope was defined as the point where the sorted values of the ratio showed a

continuous distribution. The lower envelope was then fitted to a model, $1+a/\mathrm{SNR}$, where a was determined to be 1.66. All sources that fall below the upper curve, including those below the lower curve, are considered unresolved sources. Abell 22 has 3,638 unresolved radio sources.

2.5 SNR Cut

HzRGs are intrinsically faint and easily lost in noise, imposing a minimum flux-density threshold that both suppresses spurious detections and yields a more reliable candidate list. Consequently, most HzRG searches apply such cuts, with recent studies often using sub-mJy limits at low frequencies (sub-GHz) to push deeper into the faint source population (Saxena et al., 2018a). Given the sensitivity of the MGCLS data, we can probe down to approximately 35 mJy at the 1.28 GHz 5σ level (Knowles et al., 2021). Although we selected MGCLS fields with minimal bright source artefacts, the image noise still varies across the field because of the primary beam correction, with the local RMS noise increasing toward the image edges. Instead of applying a fixed flux density cut, we apply an SNR cut, using the ratio of the fitted flux density to its associated uncertainty from the source catalogue. We apply an SNR cut of 5σ, justified as a good balance between reliability and completeness. After the SNR cut, Abell 22 contains 1,482 sources. These, together with their counterparts in the full-field sample, provide unprecedented statistical power to test the canonical spectral index for optically thin synchrotron emission (see Chapter 4).

2.6 Multi-wavelength Cross-matching

To further refine our candidate list, we exclude sources with a multiwavelength counterpart in the large sky surveys. By definition, HzRGs reside at high redshift and are expected to fall below the detection thresholds of wide-area optical and mid-infrared surveys such as DECaLS and AllWISE. DECaLS reaches median 5σ depths of $g \approx 24.7$, $r \approx 23.9$, and $z \approx 23.0$ AB magnitudes for sources with at least three passes (Dey et al., 2019). AllWISE, in comparison, achieves 5σ limits of roughly $W1 \approx 16.9$, $W2 \approx 15.95$, $W3 \approx 11.5$, and $W4 \approx 8.0$ (Vega) in uncrowded regions (Kurcz et al., 2016). To exclude sources with multi-wavelength counterparts, we first need to find them, so we do cross-matching. To select HzRG candidates from the unresolved SNR-cut catalogue of 1482

sources, we identify sources with optical and infrared counterparts by cross-matching the reduced Abell 22 radio catalogue with DECaLS and AllWISE. A simple cross-correlation method, which selects the closest object to the radio source within a set matching radius, can result in many false associations, especially with deep images (Roseboom et al., 2009). Thus, we use the likelihood ratio (LR) method, originally introduced by Sutherland and Saunders (1992) and later refined by Ciliegi et al. (2003) to perform the cross-match.

The LR value is calculated for each potential match within a defined search radius. This LR value compares the probability that a match is a true counterpart to the probability of the match being a spurious one, i.e.,

$$LR = \frac{q(m)f(r)}{n(m)} \tag{2.1}$$

where $q(m)$ represents the expected magnitude distribution for the true counterparts, $f(r)$ is the probability distribution function of the positional uncertainties in the catalogues used, and $n(m)$ denotes the surface density of unrelated background objects with magnitude m in the DECaLS r band (or g or z band). The magnitudes are AB magnitudes for DECaLS. This method considers both the position of the counterpart, the magnitude distribution of the background source, and the potential for multiple counterparts for the same radio source (Ciliegi et al., 2003), and consists of three main steps:

1. Compute $n(m)$ as a function of m;
2. Evaluate the LR for each possible counterpart;
3. Compute the reliability of each association.

Initially, the MGCLS and DECaLS are cross-matched and checked to determine whether the observed matches between the catalogues are statistically significant or if they could occur randomly. The same is applied to MGCLS and AllWISE source catalogues. Figure 2.4 shows radio sources in the Abell 22 field with overlapping DECaLS and AllWISE counterparts.

Figure 2.5 shows the comparison of the angular separations of real matches with those of randomly generated sources; the histograms demonstrate whether the observed matches are significantly closer than those expected by random chance. The real data histogram shows a sharp peak at small separations compared to the simulated data, indicating that the real matches are statistically significant and not due to random alignments.

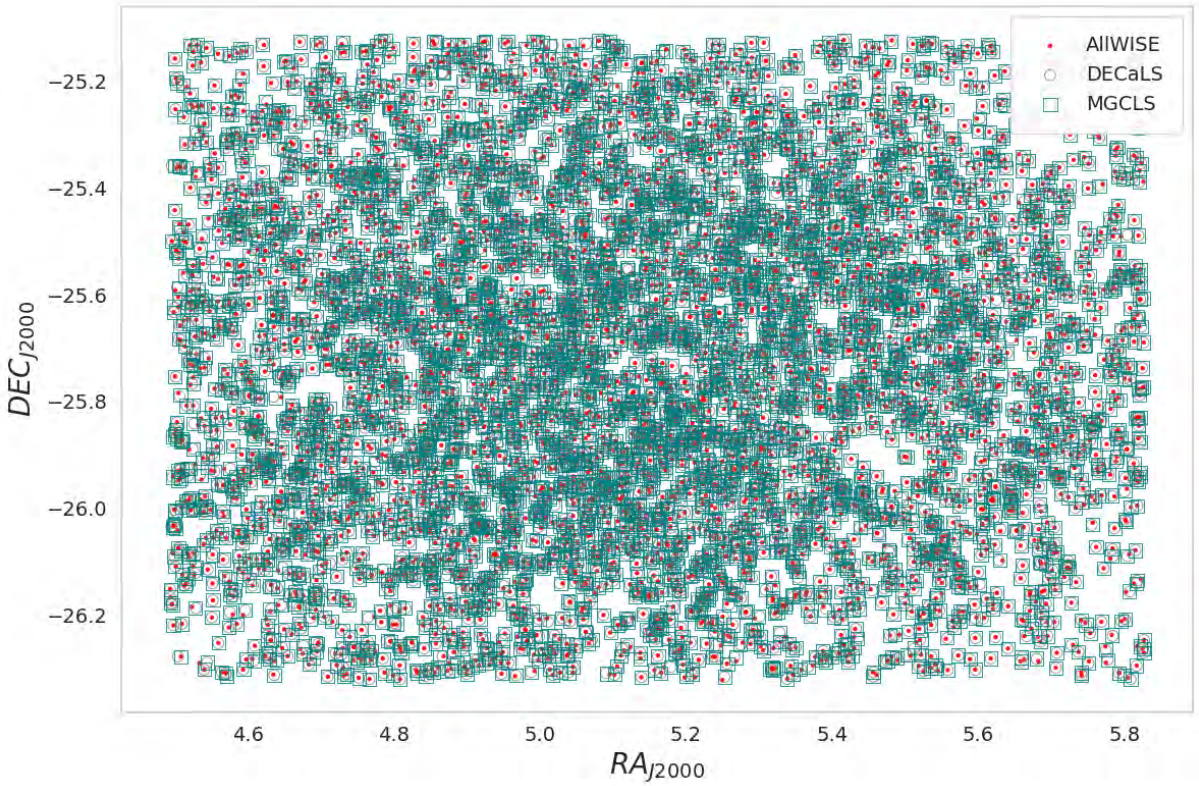

FIGURE 2.4: Radio sources in the Abell 22 field with their DECaLS and AllWISE counterparts. These objects are excluded from our HzRG candidate list because the presence of optical and infrared counterparts indicates they are unlikely to reside at high redshift.

The *a priori* probability $q(m)$ is determined as follows: initially, the radio and optical source catalogues are matched by identifying the closest counterpart within a predefined search radius of $2''$. This radius is chosen based on our distributions of cross-matches, as shown in Figure 2.6, where the distributions of the angular separations in R.A. and Dec. between the positions of the MGCLS sources can be modelled as Gaussian functions. The optimal search radius is $2''$, where the highest number of true sources is detected. Increasing the radius beyond $2''$ leads to a rise in the number of false matches. The estimated number of false matches, with magnitude m, is determined by scaling $n(m)$ to the area corresponding to the $2''$ search radius. This value is then subtracted from the total number of counterparts to obtain the number of true counterparts, $q(m)$.

The probability distribution $f(r)$ follows a two-dimensional Gaussian distribution:

$$f(r) = \frac{1}{2\pi\delta^2} \exp\left(\frac{-r^2}{2\delta^2}\right) \tag{2.2}$$

where r represents the angular separation from the radio source position, and δ is the

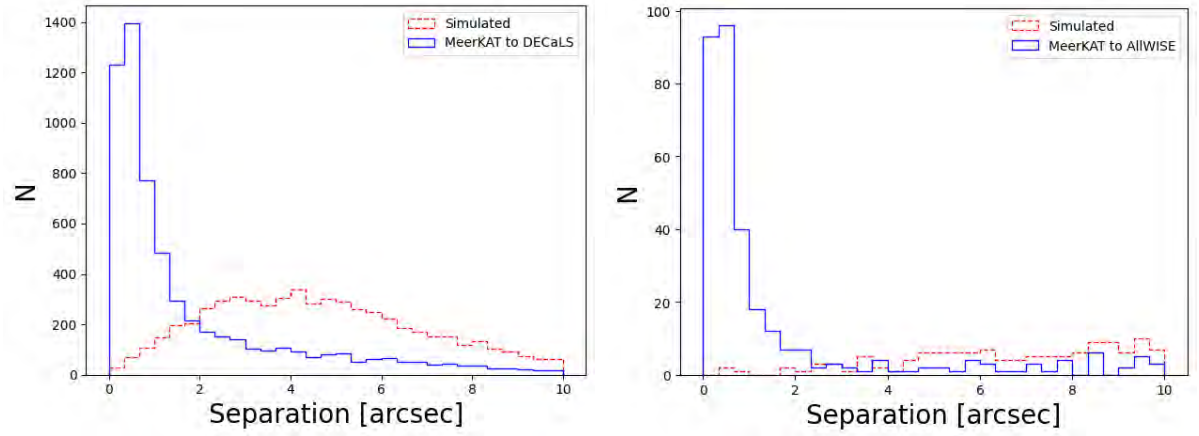

FIGURE 2.5: Comparison of angular separations between MGCLS and DECaLS counterparts **(left)** and MGCLS and AllWISE counterparts **(right)**. The blue histogram represents the actual separations between matched sources, while the red dashed histogram shows the separations for randomly simulated sources. The sharp peak in the blue curves at small separations suggests that the observed matches are statistically significant and not due to random chance.

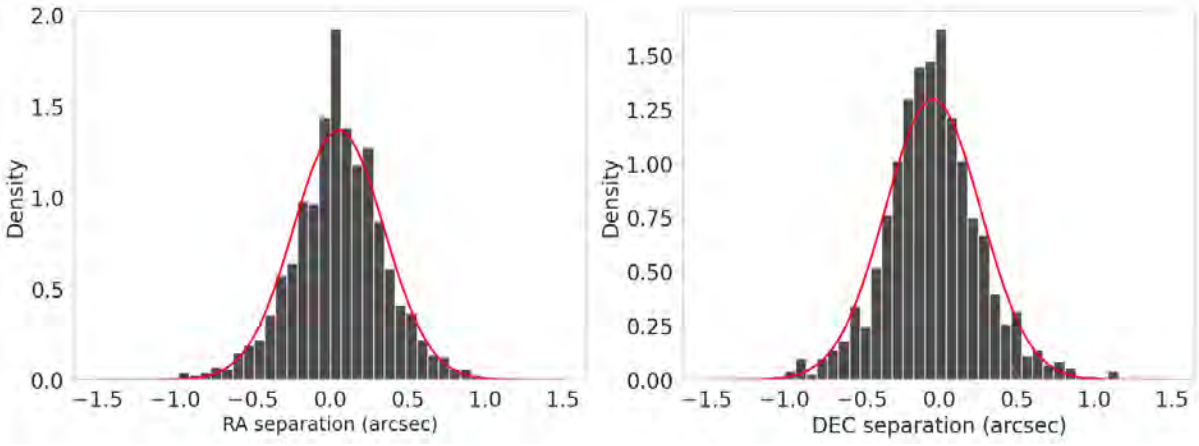

FIGURE 2.6: Histograms of the R.A. **(left)** and Dec. **(right)** angular separations between the positions of MGCLS compact source catalogue and their optical counterparts, for LR > 0.5. In each panel, the red line shows the normalised Gaussian distribution.

combined positional uncertainty, given by $\sqrt{\delta^2_{\rm DECaLS} + \delta^2_{\rm MGCLS}}$. Here, $\delta_{\rm DECaLS}$ is the positional uncertainty from the DECaLS catalogues and $\delta_{\rm MGCLS}$ is the positional uncertainty from the MGCLS compact source catalogues. For each source in the MGCLS DR1 compact source catalogues, we assume a systematic positional uncertainty of $0.2''$ in both R.A. and Dec., and the same optical position uncertainty of $0.2''$ is assumed for the DECaLS catalogue (Dey et al., 2019). The same is valid for MGCLS to AllWISE cross-match, where we assume a position uncertainty of $0.15''$ (Wright et al., 2010).

The existence of multiple counterparts for a given radio source yields additional insight beyond what is provided by the LR alone. This information can be used to assess the reliability of the counterpart source, which reflects the probability that a specific source

is the correct counterpart. The reliability of the radio source i, as defined by Sutherland and Saunders (1992), is expressed as:

$$\mathrm{REL}_i = \frac{\mathrm{LR}_i}{\sum \mathrm{LR}_{\text{search radius}} + (1 - Q)} \tag{2.3}$$

where $\sum \mathrm{LR}_{\text{search radius}}$ represents the sum of the LR values for all potential DECaLS counterparts within a search radius of $2''$. The variable Q denotes the fraction of MGCLS compact radio sources that possess optical counterparts that exceed the DECaLS magnitude limit. By comparing $\sum \mathrm{REL}_i$ with the total number of counterparts that have $\mathrm{LR} > \mathrm{LR}_{\text{cutoff}}$, we can estimate the spurious identification rate, also known as the error rate (ER). The selection of the LR cutoff is a balance between achieving maximum completeness and maximum purity. Completeness is defined as the proportion of radio catalogue sources that have an optical counterpart, while purity, calculated as $1 - \mathrm{ER}$, is the fraction of radio or optical sources that are real.

After performing the multi-wavelength cross-matching and excluding all the sources with optical and infrared counterparts, the Abell 22 field is reduced to 187 sources.

2.7 Manual Cross-checking

We use the NASA/IPAC Extragalactic Database (NED)[7] to check for any available redshift information of the MGCLS HzRG candidates or if they appear in other optical or infrared catalogues. We use a search radius of $4''$ in NED, which is half of the beam size of the lower resolution (1.28 GHz) survey, to balance the need to include true matches (given the combined astrometric uncertainties) against the risk of spurious associations in crowded fields. All candidates with $z < 2$ and/or with NED cross-matches from other optical/IR catalogues are excluded from the candidate list. Cross-checking the 187 from the Abell 22 field, we found that one source has available redshift information; however, it is at $z < 2$. This source is excluded from the candidate list, narrowing the list to 186 candidates.

[7] https://ned.ipac.caltech.edu/

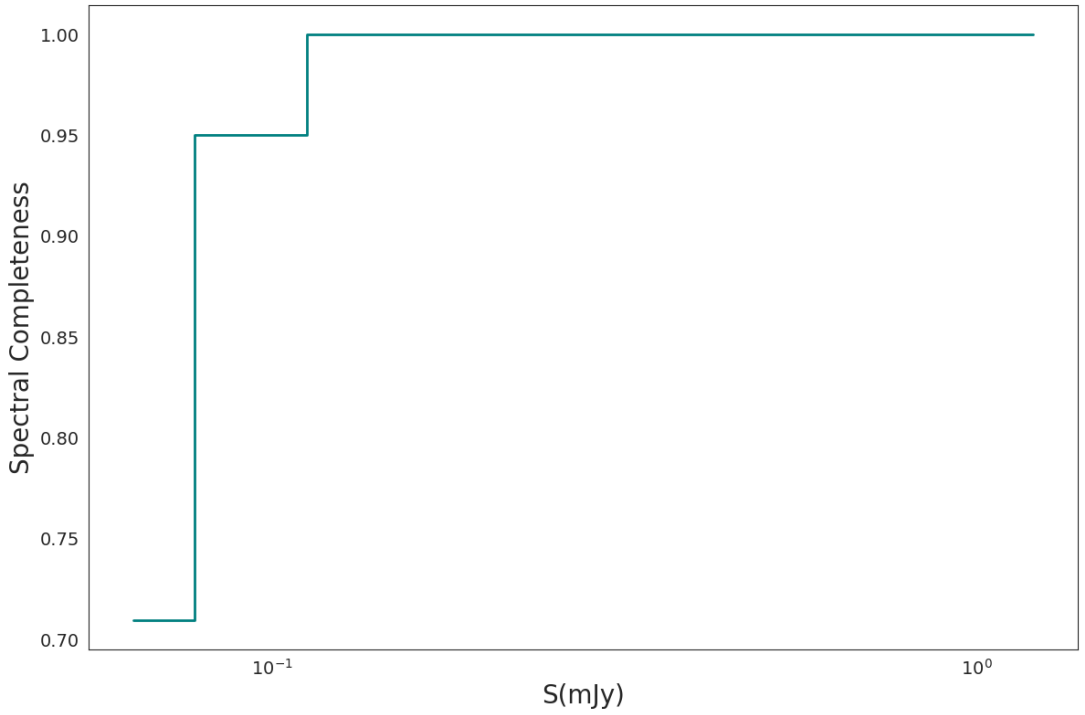

FIGURE 2.7: Spectral completeness as a function of flux density for Abell 22 field, showing the fraction of sources with spectral data. Completeness reaches 100% at a minimum flux density of $\sim$ 0.11 mJy, indicating the flux threshold for complete spectral coverage.

2.8 Ultra-Steep Spectrum Selection

USS selection is a widely used method for identifying HzRGs. The rationale is based on the correlation between the steepness of the radio spectrum and the cosmological redshift, where higher-redshift radio sources often exhibit steeper spectra (Blumenthal and Miley, 1979; Laing and Peacock, 1980; De Breuck et al., 2000). This approach has been widely adopted in the literature, typically using multi-frequency radio data to measure spectral indices over wide frequency ranges (Pentericci et al., 2000; Singh et al., 2014). Such methods, while effective, require multiple radio datasets to derive reliable spectral indices, which may not always be available.

In contrast, the wide bandwidth of the MGCLS data allows for an in-band spectral index estimation, rather than relying on separate multi-band datasets. The MGCLS data span $\sim$700 MHz in frequency, with a fractional bandwidth of 0.55 (Knowles et al., 2022), providing a continuous frequency range to derive in-band spectral indices of radio sources. This broadband nature eliminates the need for combining data from different instruments and simplifies the process of identifying HzRG candidates based on their spectral properties.

MGCLS DR1 offers a 12-plane frequency cube for each field, with effective observing frequencies at 0.908, 0.952, 0.997, 1.043, 1.093, 1.145, 1.317, 1.381, 1.448, 1.520, 1.594, and 1.656 GHz. We perform source finding using PYBDSF in each frequency plane and cross-match the resulting catalogues to build the flux density distribution for each source to estimate the spectral index value for each source. The flux density distributions are combined with the 1.28 GHz centre frequency, with its respective uncertainty, to improve the robustness of spectral indices estimation, particularly in cases where the in-band sub-bands have pronounced uncertainties.

Figure 2.7 shows a candidate's spectral completeness (defined as the fraction of sources at a given flux density that have associated spectral data in at least two sub-bands) as a function of the flux density. The completeness progressively increases with flux density, eventually reaching 100% at 0.11 mJy in the Abell 22 field. At flux densities lower than 0.11 mJy, the completeness decreases gradually due to limitations in the detection of faint sources in all sub-bands. Of a total of 186 HzRG potential candidates in the Abell 22 field, 173 have associated spectral data, giving an overall spectral completeness of 93%. The remaining 13 sources do not have associated spectral data in any sub-band.

For sources with spectral data, we start by assuming a power-law distribution, fitting a model of the form $S_\nu \propto \nu^\alpha$ to each flux density spectrum using the weighted Levenberg-Marquardt (LM) least squares method (Marquardt, 1963; Levenberg, 1944). We require sources to be detected in at least two frequency planes, with a minimum frequency separation of 200 MHz for those with only two flux density measurements, to ensure sensitivity to spectral trends when fitting a model. Among the 173 sources with spectral data, 18 fail this criterion, leaving 155 with enough spectral data for spectral index estimation. These 18 sources, along with 13 without spectral data, totalling 31 sources, remain on the candidate list, as data at additional frequencies could be used for these faintest populations, which could be provided in the near future by the MeerKAT UHF band at a similar resolution ($\sim 8''$).

Figure 2.8 shows the results of the LM power-law fit for one of the radio sources in the Abell 22 field, MKTCS J001856.90-254112.7. The slope (α) of the model was estimated at -1.39 ± 0.19. The reduced chi-square (χ^2_r) value for this fit was ~ 1, suggesting that the model fits the data relatively well, given the variance. Since the flux density measurements come from the same dataset and share the same resolution across sub-bands, any spatial variability in the flux density scale should affect all sub-band images, minimising potential biases in spectral index fitting.

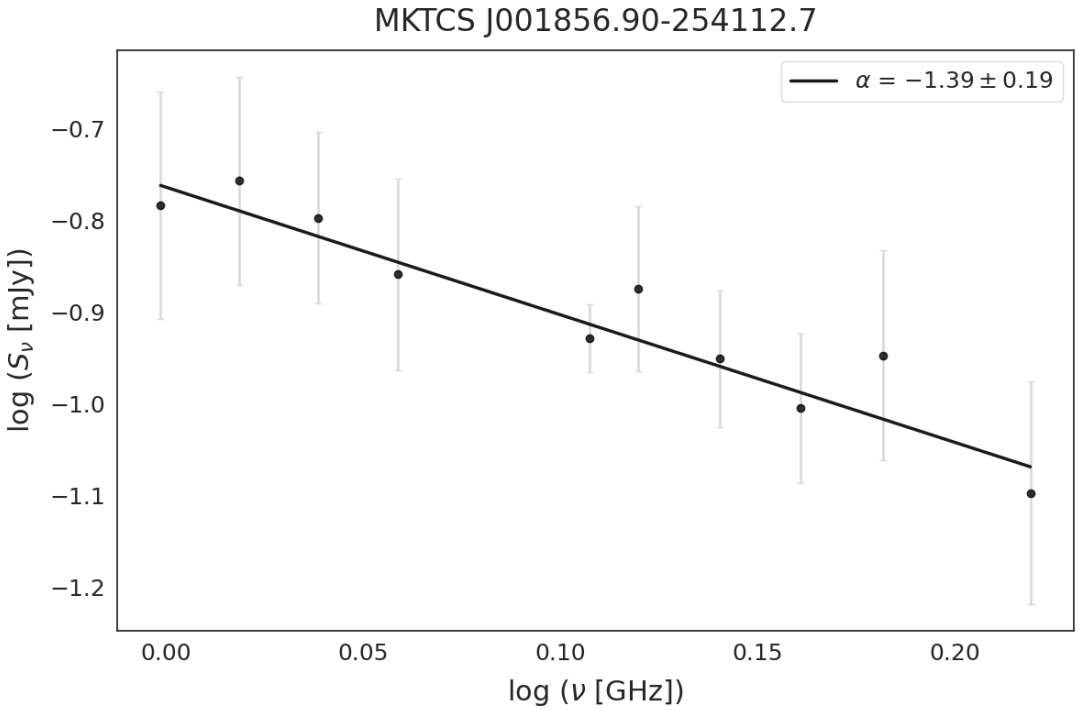

FIGURE 2.8: Radio spectrum for MKTCS J001856.90-254112.7 in Abell 22 field. The solid black line represents the LM power-law fit, giving a spectral index of $\alpha = -1.39 \pm 0.19$.

We adopt the USS selection criterion of $\alpha < -1$, which is suitable for identifying HzRG candidates, especially at low flux densities (Singh et al., 2014). Furthermore, we set a threshold for model quality, requiring the uncertainty in α, σ_α, to satisfy $\sigma_\alpha < 0.3\,|\alpha|$, and, in cases where α is small, to remain below 0.3. The choice of these values is based on the balance of statistical significance and data quality. A value of χ^2_r below 10 indicates an acceptable fit to the data while minimising the risk of including sources with poor fit. This criterion excludes poorly constrained fits, particularly at low flux densities where noise can dominate the derived α.

Of the 155 sources with enough spectral data for spectral index estimation, 56 have a reliable spectral fit, and 39 meet the USS criterion. The remaining 99 sources exhibit a poor LM fit, some deviating from a simple power-law distribution, as illustrated in Figure 2.9. Additionally, some spectra exhibit clear turnovers at higher frequencies, as illustrated in Figure 2.10.

For sources that do not follow a single power-law distribution and those that exhibit a spectral turnover, we use a piecewise fitting approach, as described by Akima (1970), to accurately capture their complex spectral shapes. Piecewise fitting is a powerful method for modelling complex data relationships, achieved by segmenting the data and applying separate fitting functions to each segment. The piecewise linear model approach allows us

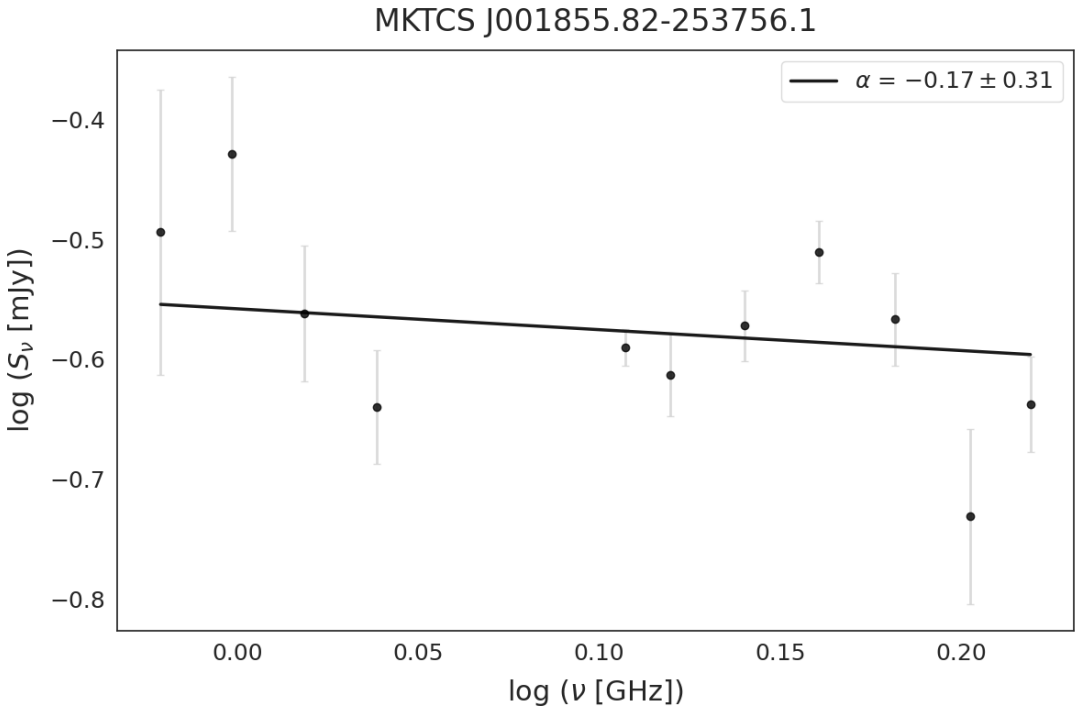

FIGURE 2.9: Radio spectrum for source MKTCS J001855.82-253756.1 in Abell 22 field. The model reveals a discrepancy with the observed flux density points with $\chi_r^2 \sim 12$, suggesting limitations in the fit's accuracy and reliability for this source.

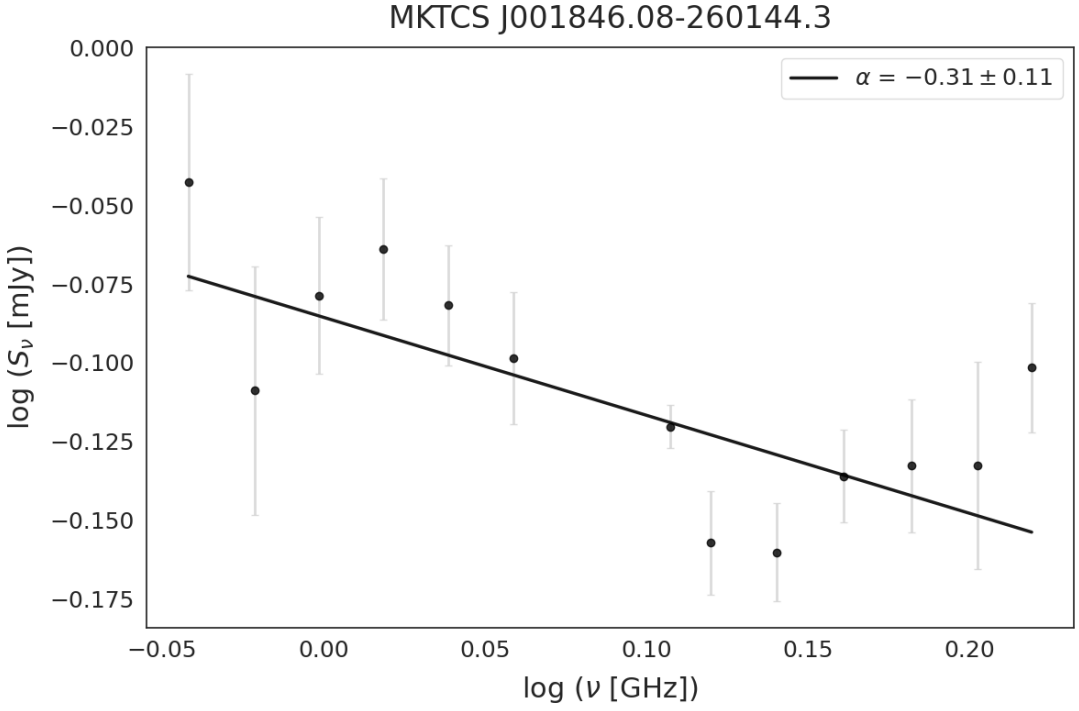

FIGURE 2.10: Radio spectrum for source MKTCS J001846.08-260144.3 in Abell 22 field. The plot reveals a spectral turnover around $\log(\nu[\text{GHz}]) \sim 0.16$, and the model fit does not accurately capture the observed flux density trend with $\chi_r^2 \sim 13$, indicating a lack of reliability of the model.

to capture the distinct spectral behaviour of sources with non-uniform flux distribution across frequencies, which is indicative of processes such as synchrotron self-absorption or free-free absorption (Tingay and De Kool, 2003).

We employ a Bayesian framework to perform the piecewise linear fitting, which provides the flexibility to model the spectral turnover by dividing the spectral profile into two segments. An example of this method is shown in Figure 2.11 for one of the potential HzRG candidates in the Abell 22 field. There are distinct spectral regimes on either side of the turnover point. We make use of the `specfit`[8] python package (see Appendix A), which is tailored to model a segmented linear relationship and infer key parameters such as the slopes, the location of the turnover (change point), and associated uncertainties. This method employs Markov Chain Monte Carlo (MCMC) sampling to draw posterior distributions for each parameter (Molteno, 2024), providing estimates of the slope before and after the turnover point, along with credible intervals. An example of this method, applied to one of the potential HzRG candidates in the Abell 22 field, is shown in Figure 2.11. The piecewise method determines two mean slopes -0.52 ± 0.16 and 0.70 ± 0.83 respectively, separated by the change point, with a mean around $\nu[GHz] = 1.41 \pm 0.13$. In this case, none of the segments falls under the USS criterion, so this source is excluded from the HzRG candidates list. For these cases, we are interested in the lower frequency part of the spectrum, below the changing point, because USS sources are intrinsically brighter at lower frequencies, so observing there boosts the SNR (Singh et al., 2014), and reduces inclusion of flat-spectrum core-dominated AGN and peaked-spectrum sources, further refining our selection (Afonso et al., 2011).

The posterior probability density function (PDF) for MKTCS J001846.08-260144.3 is shown in Figure 2.12. The PDF exhibits a sharp peak with minimal spread for the parameter cps, representing the change point, and exhibits a broad distribution, reflecting the uncertainty in the exact location of the transition. The slope parameter k, associated with the first segment of the model, also shows uncertainty, indicating variability in the initial slope of the spectrum. In contrast, the second slope m is more precisely constrained, with a narrower distribution, suggesting confidence in this part of the model. The change point difference *delta* demonstrates the most significant variability, although its high effective sample size indicates reasonable convergence.

This procedure produced spectral index measurements for all 99 sources. However, none exhibited an USS below the turnover point, and so no sources were carried forward into our final HzRG candidate list. The final HzRG candidate list for the Abell 22 field has 70

[8] https://github.com/tmolteno/specfit

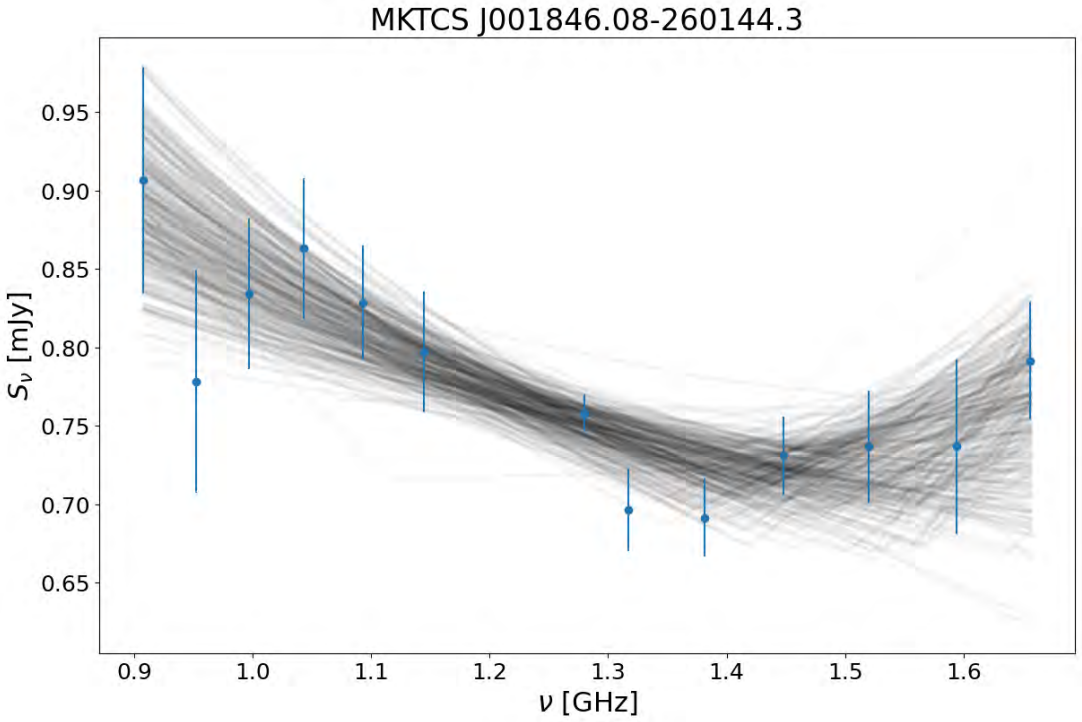

FIGURE 2.11: Radio spectrum for MKTCS J001846.08-260144.3 in Abell 22 field, showing multipole splines. We end up with two mean slopes -0.52 ± 0.16 and 0.70 ± 0.83 respectively, separated by the mean changing point at ν[GHz]$= 1.41 \pm 0.13$.

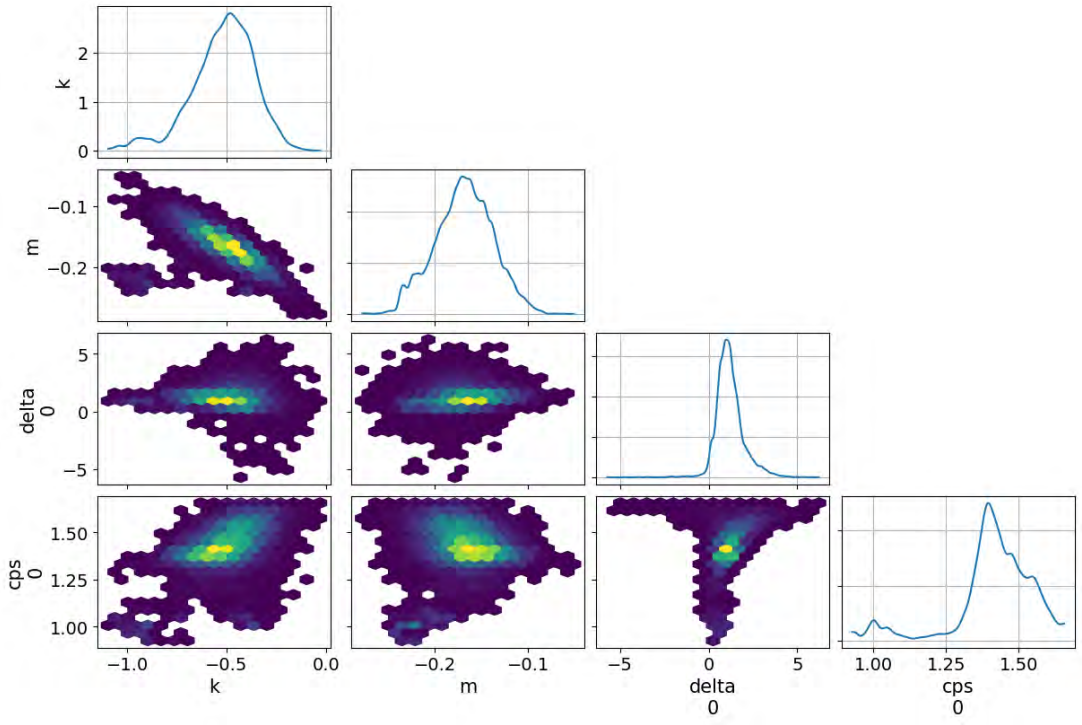

FIGURE 2.12: Pair plot of the posterior distributions and parameter relationships for MKTCS J001846.08- 260144.3 in Abell 22 field, showing marginal PDFs (diagonal) and pairwise correlations (off-diagonal) for the model parameters k, m, *delta*, and *cps*.

sources, 39 of which are USS sources and 31 potential candidates, as they lack sufficient spectral data for a reliable spectral index measurement. Together, these 70 candidates represent just 1.1% of the total number of sources in the Abell 22 MGCLS compact source catalogue. Table 2.4 summarises each stage of our multistage process, and the fraction of remaining HzRG candidates after each step.

TABLE 2.3: Selected sample of cluster fields with good dynamic range, high astrometric accuracies, and full spatial coverage in DECaLS and AllWISE. The Right Ascension (R.A.) and Declination (Dec) are given in degrees, and the RMS in μJy/beam.

Cluster Name	**R.A.**	**Dec**	***z***	**RMS**
Abell 22	5.1608	-25.7220	0.142	2.9
Abell 2744	3.5671	-30.3830	0.308	2.9
Abell 2751	4.0580	-31.3885	0.107	2.6
Abell 3562	202.7833	-31.6731	0.049	3.3
Abell 4038	356.8796	-28.2028	0.028	3.0
Abell S295	41.4000	-53.0380	0.300	2.3
J0014.3-6604	3.5767	-66.0775	0.155	2.5
J0027.3-5015	6.8388	-50.2511	0.145	2.6
J0051.1-4833	12.7967	-48.5597	0.187	2.6
J0108.5-4020	17.1383	-40.3500	0.143	2.6
J0145.2-6033	26.3196	-60.5650	0.184	2.3
J0232.2-4420	38.0700	-44.3475	0.284	2.6
J0303.7-7752	45.9433	-77.8692	0.274	2.9
J0314.3-4525	48.5825	-45.4242	0.073	2.5
J0342.8-5338	55.7246	-53.6353	0.060	3.4
J0351.1-8212	57.7871	-82.2167	0.061	2.8
J0352.4-7401	58.1229	-74.0308	0.127	2.6
J0449.9-4440	72.4800	-44.6781	0.172	2.6
J0510.2-4519	77.5575	-45.3211	0.200	3.0
J0542.8-4100	85.7117	-41.0014	0.640	2.4
J0600.8-5835	90.2013	-58.5872	0.037	2.5
J0610.5-4848	92.6333	-48.8072	0.243	2.8
J0616.8-4748	94.2233	-47.8050	0.116	3.0
J0631.3-5610	97.8363	-56.1722	0.054	2.7
J0637.3-4828	99.3288	-48.4783	0.203	3.0
J0658.5-5556	104.6296	-55.9469	0.296	3.2
J0738.1-7506	114.5375	-75.1067	0.111	2.6
J0948.6-8327	147.1642	-83.4656	0.198	3.1
J1705.1-8210	256.2929	-82.1739	0.074	2.8

TABLE 2.4: Summary of the selection criteria for the Abell 22 field. The table shows the selection step, the number of sources remaining after each step and the corresponding fraction. The final list of candidates contains USS sources obtained using the LM method, $\alpha_{LM} < -1$; sources with sufficient spectral data to fit a model, α_{none}, and USS sources obtained through `specfit`, $\alpha_{\texttt{specfit}} < -1$. The selection criteria for the full cluster sample can be found in Table 3.1.

Selection	**Number of Sources**	**Fraction (%)**
Initial catalogue	6,119	100.00
Unresolved sources selection	3,638	59.45
5σ SNR limit	1,482	45.53
Cross-match: DECaLS	424	6.92
Cross-match: AllWISE	187	3.05
Manual cross-checks	186	3.03
α_{LM} (α_{none}) ($\alpha_{\texttt{specfit}}$)	39 (31) (0)	0.63 (0.5) (0)
Total Number Candidates	70	1.14

Chapter 3

Results and Discussion

Having demonstrated the methodology used to search for HzRG in the Abell 22 field, we now apply the same techniques to the full sample introduced in Chapter 2. In this chapter, we present the flux density distributions and spectral index trends measured for the Abell 22 field, then extend the analysis to the full sample, assessing the MGCLS data's potential to isolate HzRG candidates.

3.1 HzRG Candidates: Abell 22 Field

The Abell 22 field produced 70 HzRG candidates, and the flux density distribution for the candidates is shown in Figure 3.1. Spectral index measurements for these candidates are complete above 0.134 mJy, but drop off sharply and become largely incomplete below 100 μJy. This flux density is lower than that obtained by Knowles et al. (2021) (0.3 mJy), which is the lowest flux density at GHz frequencies to be probed for HzRGs to date. All candidates without a spectral index (empty bins) are faint ($S < 0.134$ mJy), making it difficult to detect them across most of the in-band sub-bands needed for spectral index measurements.

Figure 3.2 shows the spectral index distribution of our USS candidates in the Abell 22 field, with a median value of -1.4. The histogram is bounded by the USS selection threshold ($\alpha < -1.0$).

To examine whether positional effects, such as those arising from the primary beam correction at different frequencies, influence the assignment of spectral indices to sources, we plot the sky positions of the HzRG candidates in the Abell 22 field in Figure 3.3. We

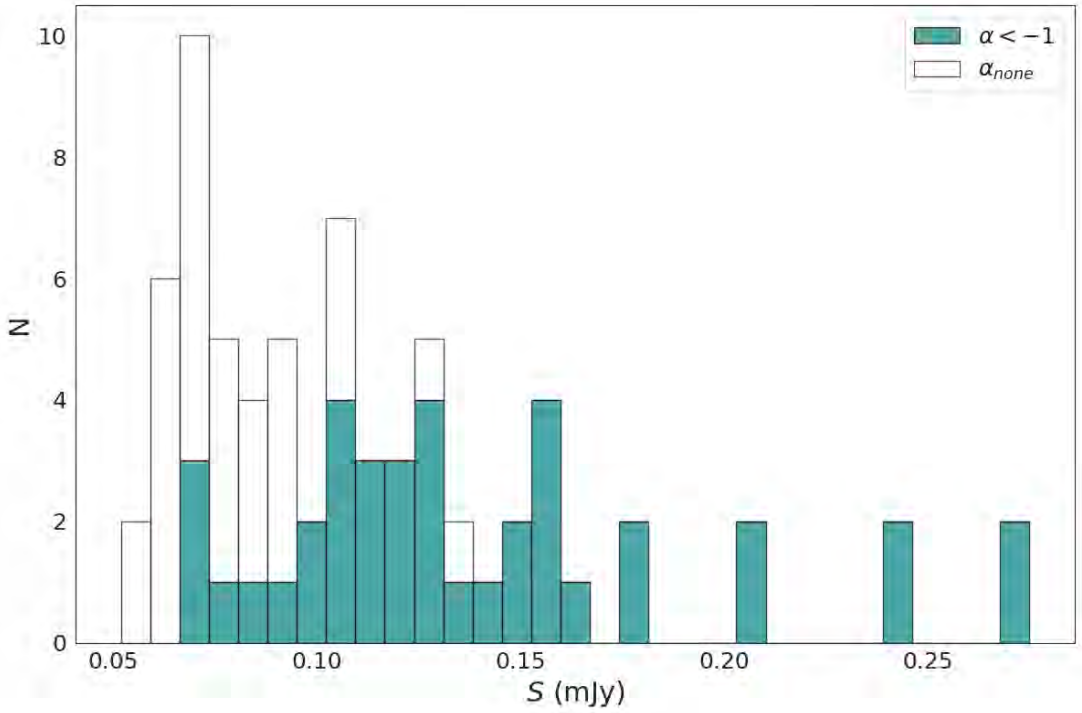

FIGURE 3.1: Flux density distribution of HzRG candidates in the Abell 22 field. Above 0.134 mJy, spectral index measurements for all candidates are complete; below 100 μJy, they become largely incomplete.

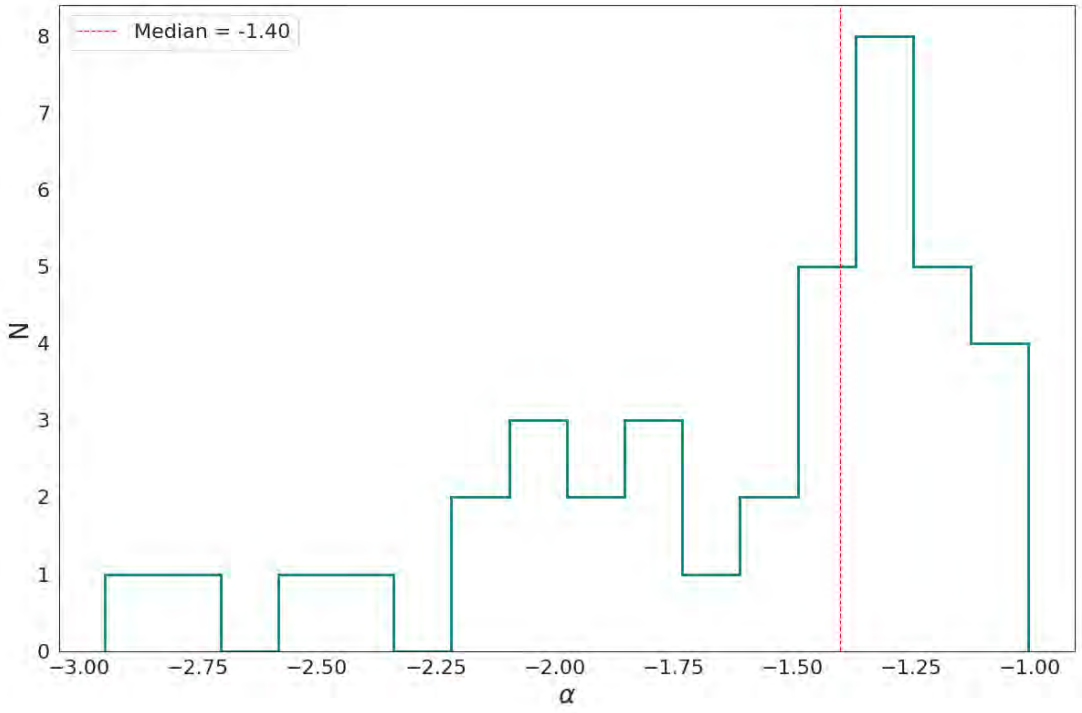

FIGURE 3.2: Spectral index distribution of HzRG candidates in the Abell 22 field. The median spectral index is −1.40.

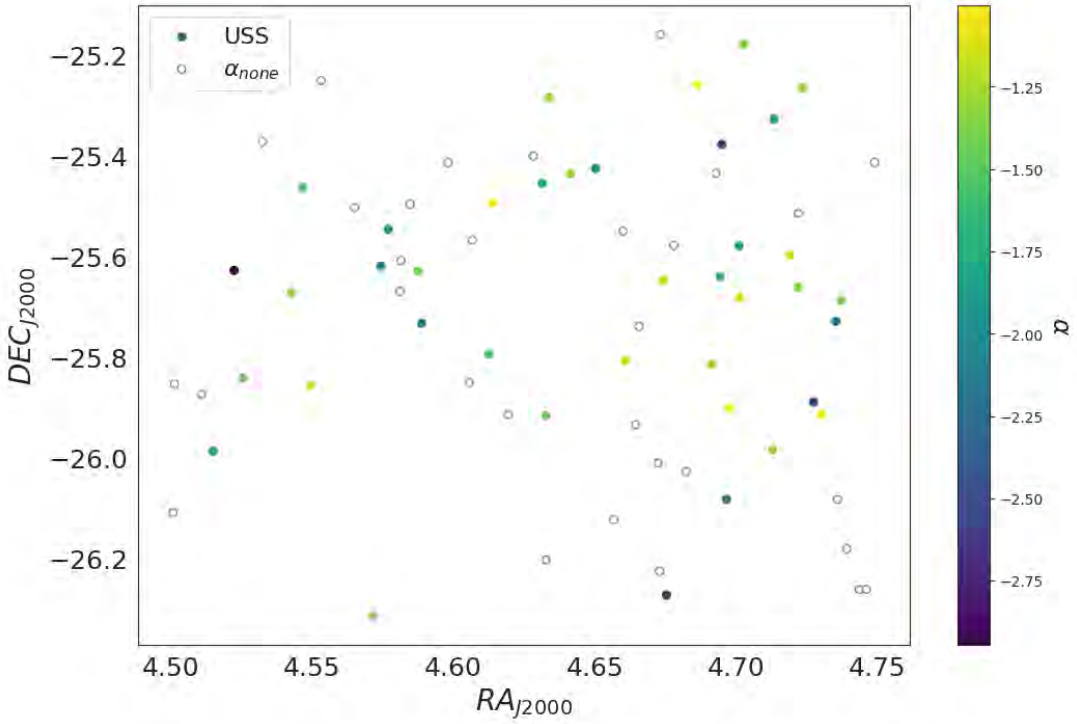

FIGURE 3.3: Sky distribution of the HzRG candidates in the Abell 22 field, with USS sources marked by coloured circles and their respective spectral indices. We see no positional trend with respect to the candidates with no spectral index values.

see no positional effects in this field, and the same is true for the full sample. The sources are colour-coded on the basis of whether or not a spectral index could be determined. The absence of a positional trend for sources with undetermined spectral index values suggests that the SNR threshold effectively accounts for variations in noise levels across the primary beam-corrected field of view. These clusters of USS candidates may indicate the positions of proto-clusters (Bornancini et al., 2006).

3.2 HzRG Candidates: Full Sample

Table 3.1 summarises the filtering of the initial 198,120 sources through each stage of our multi-step HzRG candidate search for the full sample (listed in Table 2.3). Column **A** gives the initial source count per field; Column **B** gives the number of unresolved sources retained. In Column **C** we apply a 5σ SNR restriction on flux density, and Columns **D** and **E** show, respectively, the sources without counterparts in DECaLS and in AllWISE after statistical cross-matching. Column **F** lists the objects with no redshift information in NED, while those with $z < 2$ (excluded as low redshift) are removed. Column **G** then counts the sources that have at least two flux measurements separated

by 200 MHz, sufficient for an in-band spectral-index fit, while Column **H** records those that lack enough spectral data (which we nevertheless retain as potential candidates). Columns **I** and **J** give the number of USS sources identified by the LM and `specfit` methods, respectively. Column **J** lists 10 sources whose spectra follow a broken power-law with an USS low-frequency slope (see Appendix A for details). Finally, Column **K** presents the total HzRG candidates (USS plus insufficient spectral data sources) and Column **L** their fraction as a percentage of the original sample.

The full sample produced 1,817 HzRG candidates, corresponding to $\sim 0.9\%$, over a non-contiguous total sky area of $\sim$43.2 deg^2. This low fraction highlights the rigorous selection criteria applied throughout the search. 777 of these sources are classified as USS (767 estimated using the LM method and 10 obtained using `specfit`), and 1,040 lack sufficient spectral data for spectral index estimates. Of the 3165 sources reviewed after the manual check, 2,113 have associated spectral data, resulting in an overall spectral completeness of $\sim$ 67%. The flux density distribution for all HzRG candidates in the full sample is presented in Figure 3.4. This represents the largest and faintest population of HzRG candidates identified to date, with an unprecedented number of USS sources. Above the 0.76 mJy completeness threshold, our spectral index measurements are essentially complete. Below 0.76 mJy, however, some sources lack sufficient spectral data, underscoring the need for deeper low-frequency or higher SNR observations before drawing any conclusions about their spectral index.

Figure 3.5 shows the spectral index as a function of the flux density of the HzRG candidates. Spectral index measurements are down to 30 µJy. The plot highlights the relationship between spectral steepness and flux density, showing a clear trend for more negative spectral indices for lower flux densities. This suggests that the faintest sources tend to have steeper spectra, which is consistent with the known property of HzRGs, where steep spectra are often observed in older and more distant sources (De Breuck et al., 2000; Pedani, 2003; Argo et al., 2013; Singh et al., 2014).

Table 3.2 presents an excerpt of the final list of HzRG candidates from the full sample. The table includes the IAU MGCLS source identifier, the J2000 radio coordinates in decimal degrees, the 1.28 GHz flux density with its statistical uncertainty, the source dimensions (major and minor axes and position angle), and the fitted in-band spectral index and its respective uncertainties.

The 23,071 unresolved sources detected above 5σ listed in Column **C** of Table 3.1 constitute a statistically powerful sample with which we can investigate the limits of the

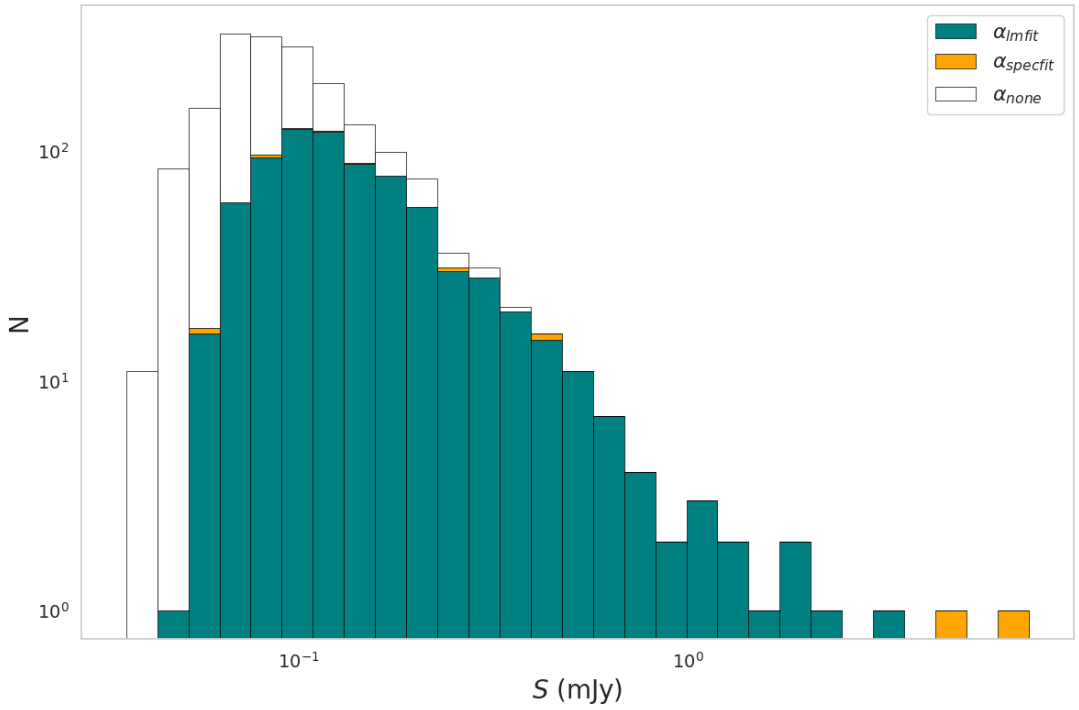

FIGURE 3.4: Flux density distribution of HzRG candidates in the full sample. The empty bins are the 1040 sources without enough spectral data for reliable spectral index determination. The orange bins are the 10 USS sources obtained through the `specfit`, and the teal bins represent the 767 USS sources obtained through the LM method. Spectral index measurements for candidates are complete above 0.76 mJy

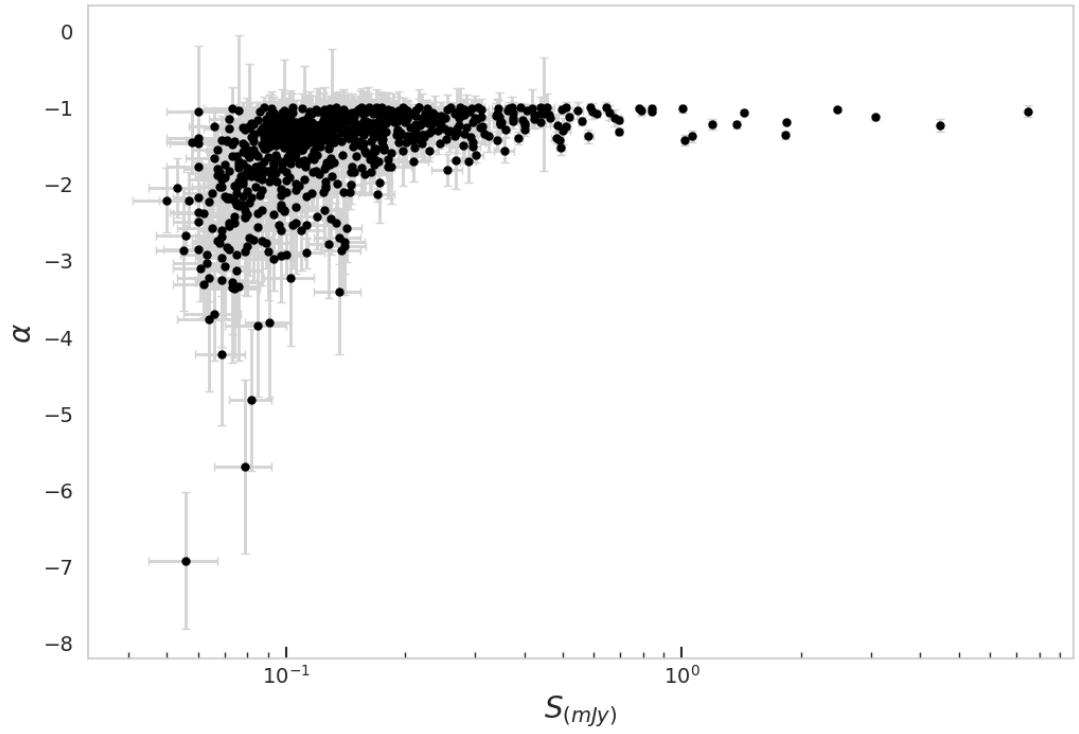

FIGURE 3.5: Spectral index as a function of flux density of HzRG candidates, down to 30 μJy. Fainter sources tend to exhibit steeper spectral indices, consistent with the properties of HzRGs.

literature's assumed canonical spectral index for flux density extrapolation, see Chapter 4.

3.3 Confirming HzRGs

Although our radio selection and in-band spectral fitting have produced a promising sample of HzRG candidates, we currently lack the spectroscopic or deep photometric data required to confirm their redshifts. To confirm the redshifts of candidates potentially at $z > 2$, requires two complementary approaches: wide-area, multi-object (fibre) redshift surveys to obtain many low-to-moderate-depth redshifts efficiently, and deep, targeted red/near-IR spectroscopy for the faintest, and highest-redshift candidates. Fibre-based facilities such as the 4-metre Multi-Object Spectroscopic Telescope (4MOST; de Jong et al., 2012) can potentially deliver large numbers of spectra across wide fields with relatively modest per–target exposure times (minutes to ∼1000s), making them efficient in confirming redshift. However, fibre surveys have practical magnitude and surface-brightness limits and are optimised for bulk spectroscopy rather than very faint single-object follow-up; consequently, the faint hosts and heavily dust-obscured counterparts expected for some of our HzRGs may remain inaccessible to these surveys and will still require long integrations with instruments that offer greater red/near-IR sensitivity.

The forthcoming facilities will change the balance between wide-area and deep follow-up. The Vera C. Rubin Observatory[1] will provide very deep, multi-epoch optical imaging across large areas, improving photometric constraints on host galaxies and enabling better photo-z estimates for many radio sources (though its optical-only bands will still leave the highest-z features in the near-infrared). JWST, with its very deep near-IR imaging and multi-object or integral-field spectroscopy, will be essential for targeted confirmations of the faintest, highest-z HzRG candidates; however, over much smaller fields than Rubin or fibre surveys.

[1] https://rubinobservatory.org/

TABLE 3.1: Summary of HzRG candidates selection process. The table presents the following columns: **A** - Total number of sources; **B** - Unresolved sources; **C** - 5σ SNR limit; **D** - Sources without DECaLS counterparts; **E** - Sources without AllWISE counterparts; **F** - Sources after manual cross-checking with NASA/IPAC Extragalactic Database; **G** - Sources with enough spectral data; **H** - Sources without enough spectral data; **I** - USS sources by LM method; **J** - USS sources by `specfit`; **K** - Final HzRG candidates; **L** - Fraction of HzRGs candidates in %.

Field	**A**	**B**	**C**	**D**	**E**	**F**	**G**	**H**	**I**	**J**	**K**	**L**
Abell 22	6,119	3,638	1,482	424	187	186	155	31	39	0	70	1.14
Abell 2744	5,224	1,010	398	99	39	39	29	10	10	0	20	0.38
Abell 2751	3,610	886	239	55	34	34	17	17	6	0	23	0.64
Abell 3562	5,442	2,283	1,080	262	138	129	89	40	28	2	70	1.29
Abell 4038	6,197	1,982	655	172	87	84	49	35	24	0	59	0.95
Abell S295	6,549	662	388	103	60	60	57	3	9	0	12	0.18
J0014.3-6604	8,456	1,050	332	114	71	71	43	28	19	0	47	0.56
J0027.3-5015	5,810	788	230	57	27	27	22	5	11	0	16	0.28
J0051.1-4833	7,311	1,599	459	112	55	54	26	28	11	1	40	0.55
J0108.5-4020	6,914	3,375	1,282	329	148	147	76	71	28	1	100	1.45
J0117.8-5455	8,221	3,642	1,582	431	184	183	114	69	59	1	129	1.57
J0145.2-6033	6,645	858	216	61	29	29	16	13	6	0	19	0.29
J0232.2-4420	7,873	4,381	1,900	481	189	189	112	67	43	0	110	1.40
J0303.7-7752	5,261	1,686	586	164	62	62	40	22	18	0	40	0.76
J0314.3-4525	8,355	4,740	2,346	570	634	222	175	47	72	1	120	1.44
J0342.8-5338	6,144	440	109	25	11	11	8	3	2	0	5	0.08
J0351.1-8212	6,815	2,502	1,112	330	166	166	114	52	31	1	84	1.23
J0352.4-7401	5,621	2,314	876	305	190	189	135	54	47	0	101	1.80
J0449.9-4440	7,757	1,720	569	151	71	71	46	25	15	1	41	0.53
J0510.2-4519	6,113	1,378	680	144	65	65	48	17	13	1	31	0.51
J0542.8-4100	7,804	2,435	1,074	299	148	148	105	43	49	0	92	1.18
J0600.8-5835	7,394	1,378	421	109	47	47	34	13	16	0	29	0.39
J0610.5-4848	5,910	929	448	108	45	45	41	4	11	0	15	0.25
J0616.8-4748	6,835	1,765	660	169	67	67	40	27	14	0	41	0.60
J0631.3-5610	8,357	2,497	907	299	164	162	102	60	50	0	110	1.32
J0637.3-4828	6,701	2,702	1,333	484	264	264	182	80	54	0	134	1.99
J0658.5-5556	5,759	370	63	13	7	7	3	4	1	0	5	0.09
J0738.1-7506	7,681	1,463	462	202	139	138	79	59	34	0	93	1.21
J0948.6-8327	6,932	1,771	845	291	166	166	106	60	29	0	89	1.28
J1705.1-8210	4,310	1,132	337	171	103	103	50	53	18	1	72	1.67
Total	**198,120**	**57,379**	**23,071**	**6,536**	**3,597**	**3,163**	**2,113**	**1,040**	**767**	**10**	**1,817**	**0.92**

TABLE 3.2: Excerpt from the HzRG candidates from the full sample. Columns list the IAU MGCLS source ID, J2000 coordinates (deg), total flux density and uncertainty (mJy), major and minor deconvolved axes (arcsec), in-band spectral index and uncertainty, Model Flag (MF) where 0 = `specfit`; 1 = LM, and the survey field name. The full catalogue is available online at HzRG Candidates Catalogue.

Source name	**RA** (deg)	**Dec** (deg)	$S_{\rm tot}$ (mJy)	ΔS (mJy)	$s_{\rm max}$ (arcsec)	$s_{\rm min}$ (arcsec)	α	$\Delta\alpha$	**MF**	**Field**
MKTCS J010537.48-400624.9	16.4062	-40.1069	0.131	0.014	7.9	7.3	-1.03	0.78	0	J0108.5-4020
MKTCS J044807.46-440449.8	72.0311	-44.0805	4.480	0.018	7.4	7.4	-1.24	0.08	0	J0449.9-4440
MKTCS J011517.99-550605.7	18.8250	-55.1016	0.060	0.010	8.0	7.8	-1.06	0.85	0	J0117.8-5455
MKTCS J132908.53-311305.8	202.2856	-31.2183	7.483	0.019	7.7	7.1	-1.05	0.07	0	Abell 3562
⋮	⋮	⋮	⋮	⋮	⋮	⋮	⋮	⋮	⋮	⋮
MKTCS J164920.25-820932.1	252.3344	-82.1589	0.294	0.019	8.2	7.0	-1.01	0.12	1	J1705.1-8210
MKTCS J165259.61-821411.5	253.2484	-82.2365	0.317	0.015	7.9	7.3	-1.35	0.14	1	J1705.1-8210
MKTCS J165249.81-821342.8	253.2076	-82.2286	1.018	0.015	8.0	7.3	-1.43	0.07	1	J1705.1-8210
MKTCS J164838.13-815450.2	252.1589	-81.9140	0.114	0.021	7.8	7.6	–	–	–	J1705.1-8210
MKTCS J165138.12-814637.4	252.9088	-81.7771	0.297	0.022	8.4	7.1	-1.46	0.22	1	J1705.1-8210
MKTCS J164920.25-820932.1	252.3344	-82.1589	0.294	0.019	8.2	7.0	-1.01	0.12	1	J1705.1-8210
MKTCS J164655.13-823019.1	251.7297	-82.5053	0.117	0.021	8.3	6.8	–	–	–	J1705.1-8210
MKTCS J164645.48-823020.1	251.6895	-82.5056	0.114	0.022	9.0	6.3	–	–	–	J1705.1-8210

Chapter 4

Testing the Spectral Index Assumption for Flux Density Extrapolation

In Chapter 2, our search for HzRG candidates yielded a statistically large sample of sources with reliable in-band spectral index measurements. Building on this, we investigate the limitations of the assumption of a canonical spectral index in the literature, particularly important when doing flux density extrapolations between different frequencies. We compare the flux densities extrapolated using the canonical spectral index value to those based on in-band spectral index measurements across different frequencies and SNR regimes. This allows us to quantify the applicability of the canonical spectral index at MeerKAT L-band frequencies and identify any systematic deviations.

4.1 Radio spectral indices

Early radio astronomy observations established that most non-thermal radio sources exhibit power-law spectra of the form $S_\nu \propto \nu^\alpha$, interpreted as arising from synchrotron emission (Kellermann, 1964; Pacholczyk, 1970). Over the decades, this assumption has remained central to characterising radio galaxy populations. The so-called canonical spectral index of $\alpha \approx -0.7$ emerged from statistical studies of large samples of extragalactic radio sources, typically interpreted as optically thin synchrotron radiation from relativistic electrons in magnetic fields (Condon, 1992; De Zotti et al., 2010).

More recent work continues to adopt this approximation, particularly in simulations and flux extrapolations across frequencies, while also probing its limitations. In 2017, Intema et al. (2017) cross-matched the TGSS and NVSS, measuring the spectral indices of over 1.4 million sources with a full sky median of $\alpha \approx -0.70$. In 2019, Tiwari (2019) analysed sources common to TGSS and NVSS, about 1.3 million sources, reporting a median $\alpha \approx -0.78$. The sample was divided into two categories based on flux densities: Low flux, with TGSS < 100 mJy and NVSS < 20 mJy, and High flux, with TGSS > 100 mJy and NVSS > 20 mJy. In 2020, sources with integrated flux densities greater than 4 Jy at 151 MHz were selected from the Galactic and Extragalactic All-sky Murchison Wide-field Array (GLEAM) survey, finding $\alpha \approx -0.740 \pm 0.012$ (151–843 MHz) and -0.786 ± 0.006 (151 MHz–1.4 GHz) (Hurley-Walker et al., 2017). Shimwell et al. (2022) cross-matched 22000 sources from the Low Frequency Array (LOFAR) Low-Band Antenna Sky Survey (LoLSS) against NVSS and the LOFAR Two-metre Sky Survey (LoTSS) DR2, yielding $\alpha \approx -0.77 \pm 0.18$ and -0.71 ± 0.31, respectively. More recently, Böhme et al. (2023) confirmed median spectral indices of -0.77 and -0.71 in a combined LOFAR low- and high-band study for sources above 181 mJy.

Given the wideband nature of the MGCLS data, we use the 23,071 unresolved sources, all detected above 5σ in the total intensity full-band image (presented in Table 3.1; see Chapter 3), to create a sample of radio power-law spectral index measurements of the MGCLS full sample. Each unresolved source in our sample has flux densities measured in 12 sub-bands, in addition to the 1.28 GHz reference frequency of the MGCLS. We model each spectrum with a weighted LM fit of the form $\log S_\nu = \log S_0 + \alpha \log\left(\frac{\nu}{\nu_0}\right)$, where $\nu_0 = 1.28\,\mathrm{GHz}$. We require at least three detections per source (i.e, in more than three frequency planes) to perform the fit.

Of the 23,071 total unresolved sources, 15,795, which account for 68.5%, meet this criterion, yielding initial spectral index measurements; the remaining 7,276 lack sufficient sub-band coverage for a reliable fit. We set a threshold for model quality, requiring σ_α, to satisfy $\sigma_\alpha < 0.3\,|\alpha|$, and, in cases where α is small, to remain below 0.3 (see Chapter 2). We obtain 11,043 reliable spectral index measurements. The remaining 4,752 sources do not follow a single power-law distribution and are not included in our analysis. Our analysis sample of 11,043 radio sources constitutes 47.9% of the detected unresolved sources.

Figure 4.1 shows the plot of spectral index versus flux density of the power-law spectrum sources, with fainter sources tending to have a wider range of spectral indices. Of

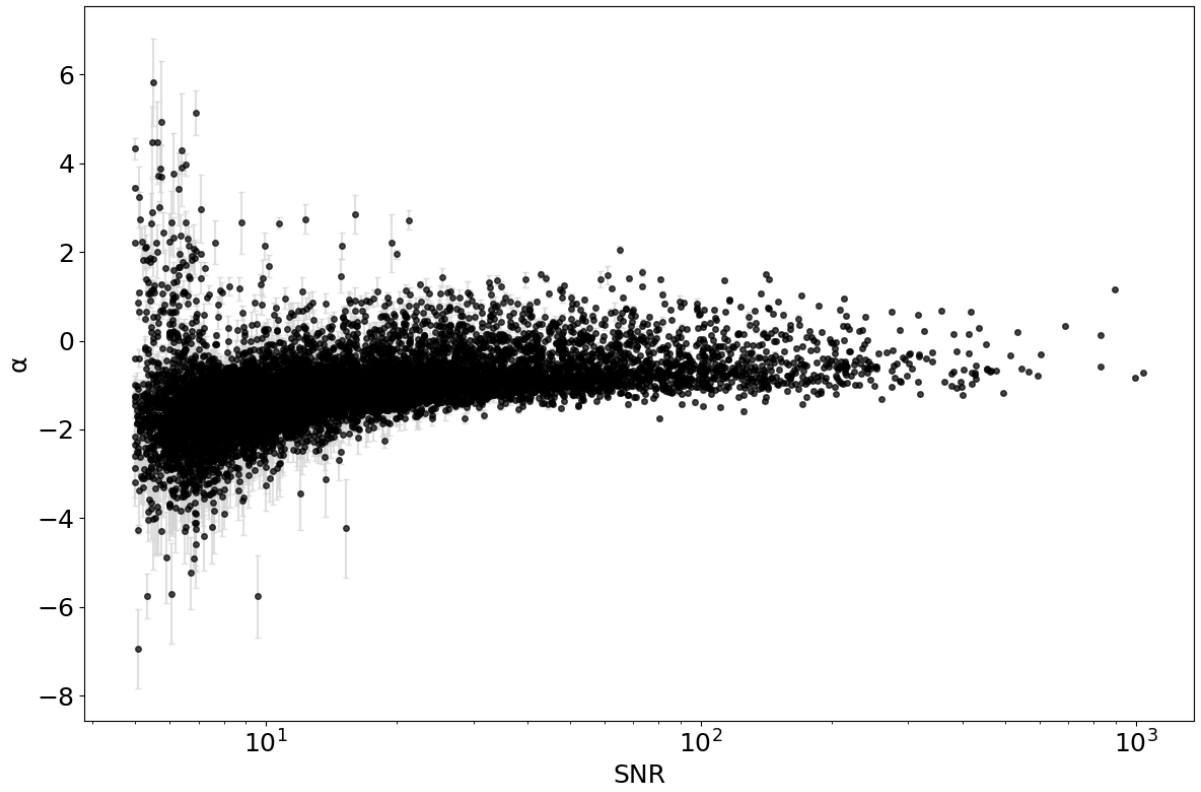

FIGURE 4.1: Plot of spectral index versus SNR, with fainter sources showing a larger range of observed spectral indices, including more inverted and steeper spectral slopes.

the 11,043 sources with reliable spectral index measurement, 9481 are considered steep-spectrum sources ($\alpha < -0.5$), 850 flat-spectrum sources ($-0.5 \leq \alpha \leq 0$), and 712 are considered inverted-spectrum sources ($\alpha > 0$). Steep-spectrum sources are often associated with HzRGs (Dwarakanath and Kale, 2009; van Weeren et al., 2011; van Weeren et al., 2019). Flat-spectrum sources and inverted-spectrum sources are less common (Zhang et al., 2003). Extremely inverted spectra ($\alpha > 2.5$) are rare and may indicate free-free absorption or non-standard electron energy distributions (Krishna et al., 2014).

Following the criteria used for MGCLS flux-density validation by Knowles et al. (2022), which uses SNR ≥ 50 and the canonical spectral index for its quality checks, we begin by selecting sources with SNR≥ 50. From this high-confidence subset, we then lower the threshold stepwise to SNR lower limits of 30, 20 and 10, tracking how the median in-band spectral index deviates from the canonical value at each stage.

Figure 4.2 shows the spectral index versus the SNR at different SNR levels. At SNR ≥ 50, there are 1,115 radio sources. Figure 4.2a shows a slight but noticeable flattening of the median α to -0.63 ± 0.02, with an interquartile range (IQR) ranging from -0.88 to -0.22. At this SNR threshold, flatter-spectrum cores emerge, shifting the distribution away from

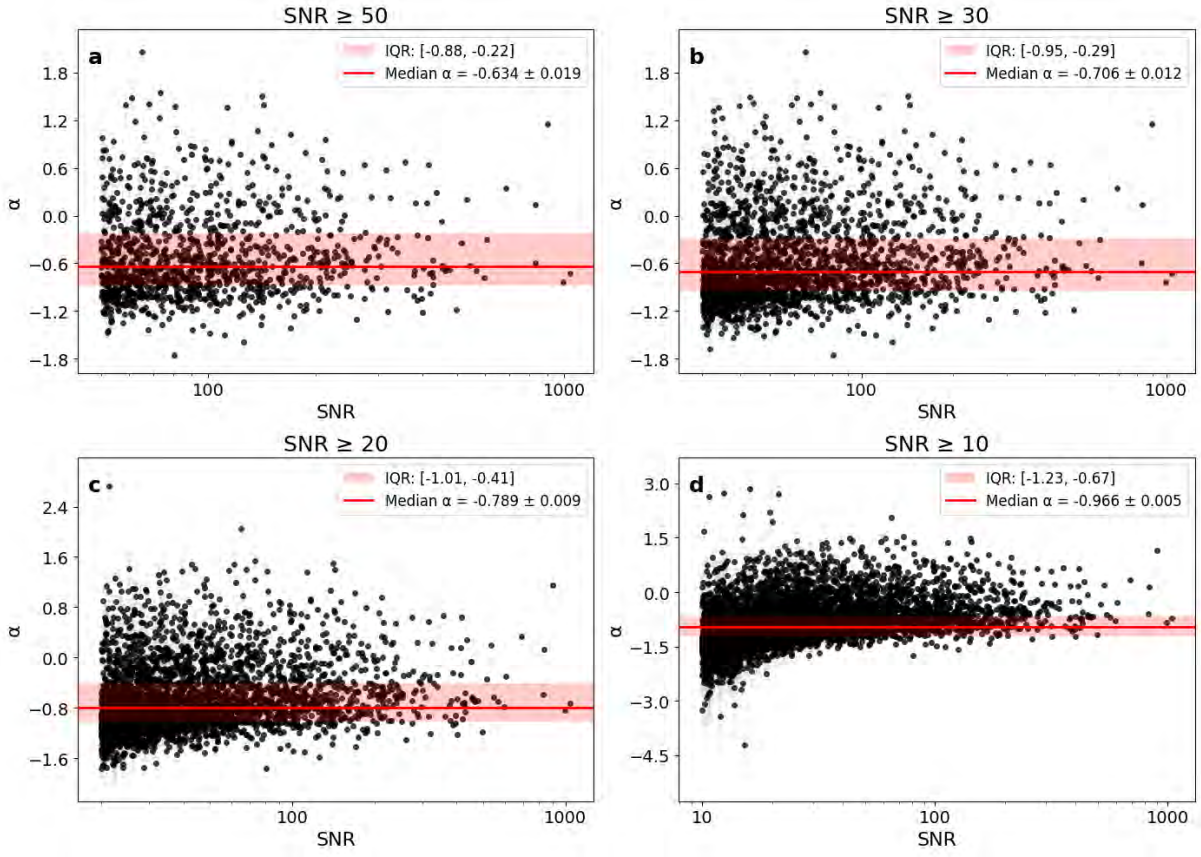

FIGURE 4.2: Spectral index versus SNR for sources with total flux < 10 mJy, shown in four panels: (a) SNR ≥ 50, (b) SNR ≥ 30, (c) SNR ≥ 20, and (d) SNR ≥ 10. In each panel, the red shaded band indicates the IQR of α; and the red horizontal line is the median α with its estimated uncertainty.

the canonical spectral index. For these high-SNR sources, assuming $\alpha = -0.7$ for flux density extrapolation would somewhat overestimate the low-frequency flux densities.

At SNR ≥ 30, the sample is increased to 2080 radio sources. In Figure 4.2b, the median α is -0.71 ± 0.01, closely matching the canonical spectral index, and the IQR ranges from -0.95 to -0.29. At this SNR threshold, assuming the canonical spectral index for flux density extrapolations would introduce only a minor systematic error for most radio sources.

The SNR ≥ 20 increases the sample to 3385 radio sources. Figure 4.2c shows that the median α is -0.79 ± 0.01, and the IQR ranges from -1.01 to -0.41. Nearly half of the sources lie outside the IQR, and assuming the canonical spectral index for flux density extrapolations would introduce systematic error for most radio sources.

Finally, at SNR ≥ 10, the sample increases to 7383 radio sources. Figure 4.2d shows that the median spectral index in this subset is steep, at $\alpha = -0.97 \pm 0.01$, with an IQR

ranging from -1.23 to -0.67. At this SNR, trying to extrapolate flux densities using the canonical spectral index would systematically overestimate the flux densities of most sources, especially the lower frequency ones, as the median spectral index is steeper than the canonical spectral index, making most sources fall off more rapidly towards lower frequencies than the canonical law would predict.

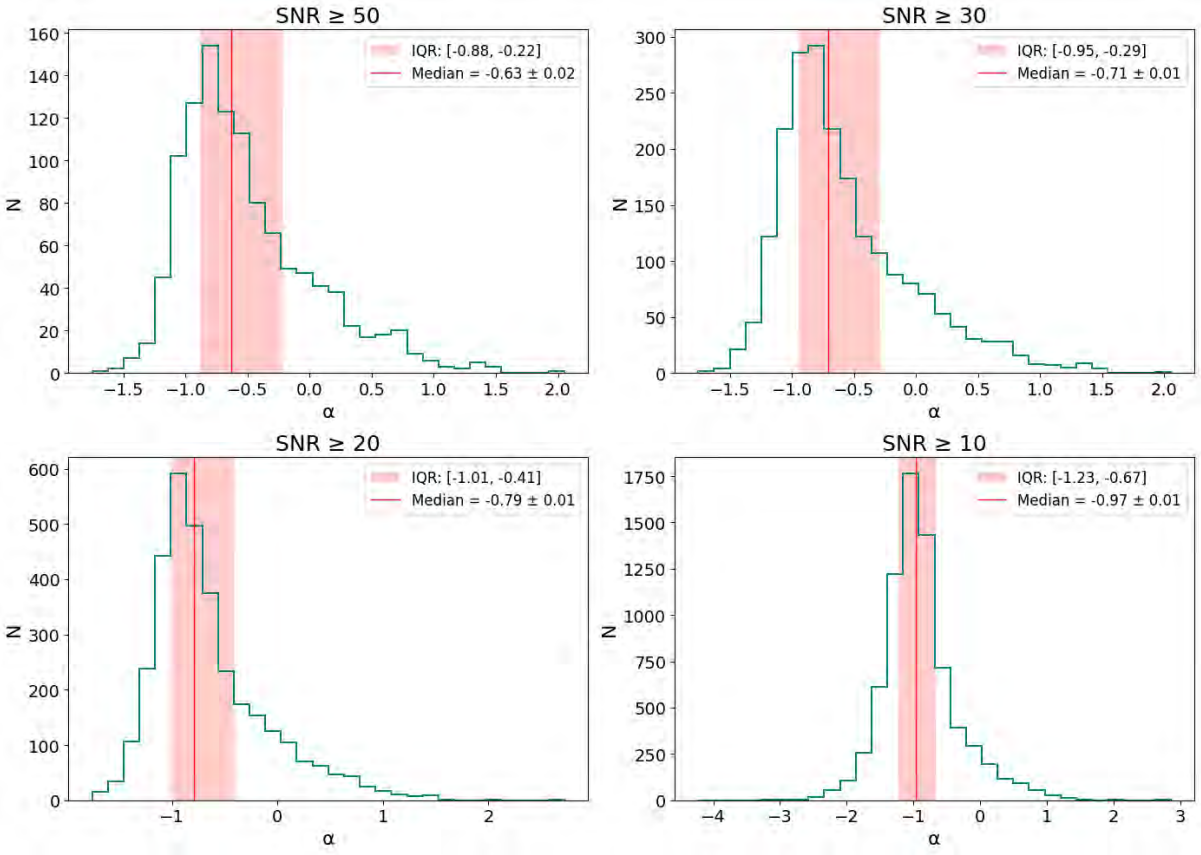

FIGURE 4.3: Spectral index distributions for sources with total flux < 10 mJy, shown in four panels: (a) SNR ≥ 50, (b) SNR ≥ 30, (c) SNR ≥ 20, and (d) SNR ≥ 10. In each panel, the teal stepped line represents the histogram of α values; the red shaded region marks the IQR of the distribution; and the solid red vertical line indicates the median α. Restricting to SNR $\geq$ 30 significantly narrows the α distribution and reduces the median's uncertainty.

Below SNR ≈ 20, noise bias makes the canonical spectral index assumption for flux density extrapolation not reliable; between SNR 20 and 30, the population median approaches -0.7 but with large scatter; at SNR ≥ 30, $\alpha = -0.7$ is justified; and above SNR ≈ 50, a slight intrinsic flattening of the spectral indices emerges.

Figure 4.3 shows the spectral index distributions of the sources at different SNR thresholds, with flux < 10 mJy. Sources down to SNR ≥ 10 present a large statistical sample of α, however, the median α is more affected by noise. Sources down to SNR ≥ 30 present

a narrow, well-defined α distribution and minimal uncertainty on the median α. In practice, SNR ≥ 30 provides a good balance, as the median α remains at about -0.7 and the spread of the distribution is relatively small if compared with the SNR ≥ 50 sources.

4.2 Effect on Flux Density Extrapolation

To investigate the impact of the canonical spectral index assumption on flux density extrapolations, we compare the flux densities extrapolated across wide frequency ranges at different SNR, using the canonical spectral index assumed in the literature $\alpha_{\rm can} = -0.70 \pm 0.01$, versus our measured in-band spectral index $\alpha_{\rm meas}$. This analysis allows us to quantify the systematic deviations introduced when adopting a typical spectral index for extrapolating to frequencies far from the MGCLS reference frequency of 1.28 GHz.

For each source with measured flux density S_0 at $\nu_0 = 1.28$ GHz, we extrapolate the fluxes to a target frequency ν, using the $\alpha_{\rm can}$ and $\alpha_{\rm meas}$ via:

$$S_{\alpha_{can}}(\nu) = S_0 \left(\frac{\nu}{\nu_0}\right)^{\alpha_{\rm can}}, \qquad S_{\alpha_{\rm meas}}(\nu) = S_0 \left(\frac{\nu}{\nu_0}\right)^{\alpha_{\rm meas}}.$$

The uncertainties on the extrapolated flux densities using the canonical spectral index and the median spectral index are:

$$\sigma_{S_{\alpha_{\rm can}}} = S_{\alpha_{\rm can}} \left|\ln\left(\frac{\nu}{\nu_0}\right)\right| \sigma_{\alpha_{\rm can}}$$

and

$$\sigma_{S_{\alpha_{\rm meas}}} = S_{\alpha_{\rm meas}} \left|\ln\left(\frac{\nu}{\nu_0}\right)\right| \sigma_{\alpha_{\rm meas}}$$

We then perform a weighted least-squares fit in log space:

$$\log_{10} S_{\alpha_{\rm meas}} = \log_{10} G + K \log_{10} S_{\alpha_{\rm can}},$$

where G is a flux scale factor and K is a slope parameter, using weights $w = 1/\sigma^2_{\log_{10} S_{\alpha_{\rm meas}}}$. Values of 1 for G and K would indicate an exact one-to-one correspondence. This approach helps us to quantify the effects of extrapolating flux densities to different frequencies using our median spectral indices in different SNR thresholds. The uncertainties in G and K were derived from the fit covariance matrix.

We extrapolate the MGCLS flux density of each source at 1.28 GHz across three survey frequencies: the Rapid ASKAP Continuum Survey (RACS) Mid frequency of 1367.5 MHz, at ~ 100 MHz above MGCLS, and RACS-Low frequency of 887.5 MHz (Duchesne et al., 2023) at ~ 400 MHz below the MGCLS; and LoTSS DR2 frequency of 144 MHz (Shimwell et al., 2022), at ~ 1 GHz below MGCLS, using the canonical spectral index. We then repeat the extrapolations with each source's measured in-band spectral index and compare the two sets to quantify the bias and uncertainty introduced by assuming a fixed spectral slope.

Figure 4.4 shows the comparison of flux density extrapolations for radio sources at SNR ≥ 10 and SNR ≥ 20. The fluxes were extrapolated to frequencies at 100 MHz, 400 MHz and 1 GHz away from the MGCLS centre frequency, respectively. Panels **a** and **b** show the comparison between the flux densities extrapolated using α_{can} and α_{meas}. The sources lie almost exactly on the 1:1 dashed red line, and a least-squares fit (solid orange) returns G = 0.99 $\pm$ 0.00, demonstrating that the assumption of canonical spectral index does not adversely affect the flux density extrapolation if the frequency difference is less than 100 MHz. Panels **c** and **d** show the 400 MHz frequency offset, which presents a slight positive deviation, with G = 1.02 $\pm$ 0.00 at SNR ≥ 10 and G = 1.03 $\pm$ 0.00 at SNR ≥ 20, suggesting that the sources are marginally brighter than predicted by a simple power-law extrapolation with α_{can}. Panels **e** and **f** show the 1 GHz frequency offset, with a significant upward flux deviation with G = 2.03 $\pm$ 0.01 at SNR ≥ 10 and G = 2.60 $\pm$ 0.01 at SNR ≥ 20, indicating that low-frequency emission is substantially stronger than expected, over 100% brighter, highlighting the inadequacy of using the canonical spectral index assumption across frequency offset above 1 GHz.

Figure 4.5 shows a more conservative sample of radio sources at SNR ≥ 30 and SNR $\geq$ 50. The 100 MHz frequency offset for both SNR thresholds again confirms its excellent consistency with expectations, with G = 0.99 $\pm$ 0.00, maintaining near perfect alignment with the 1:1 line, as shown in panels **a** and **b**. In contrast, the 400 MHz frequency offset shows a slightly larger deviation, with G = 1.05 $\pm$ 0.00 at SNR ≥ 30, and G = 1.07 $\pm$ 0.00 at SNR ≥ 50, now implying a $\sim$5% and $\sim$7% excess in the measured flux densities, as shown in panels **c** and **d** respectively. This may reflect the beginning of a trend in which steep-spectrum sources dominate at higher SNR. Panels **e** and **f** show the 1 GHz frequency offset, with G = 3.14 $\pm$ 0.01 at SNR ≥ 30, corresponding to a 214% increase in flux density compared to what would be expected. At SNR ≥ 50, the deviation reaches its peak with G = 4.12 $\pm$ 0.02, which implies that the flux densities are 312% higher than expected.

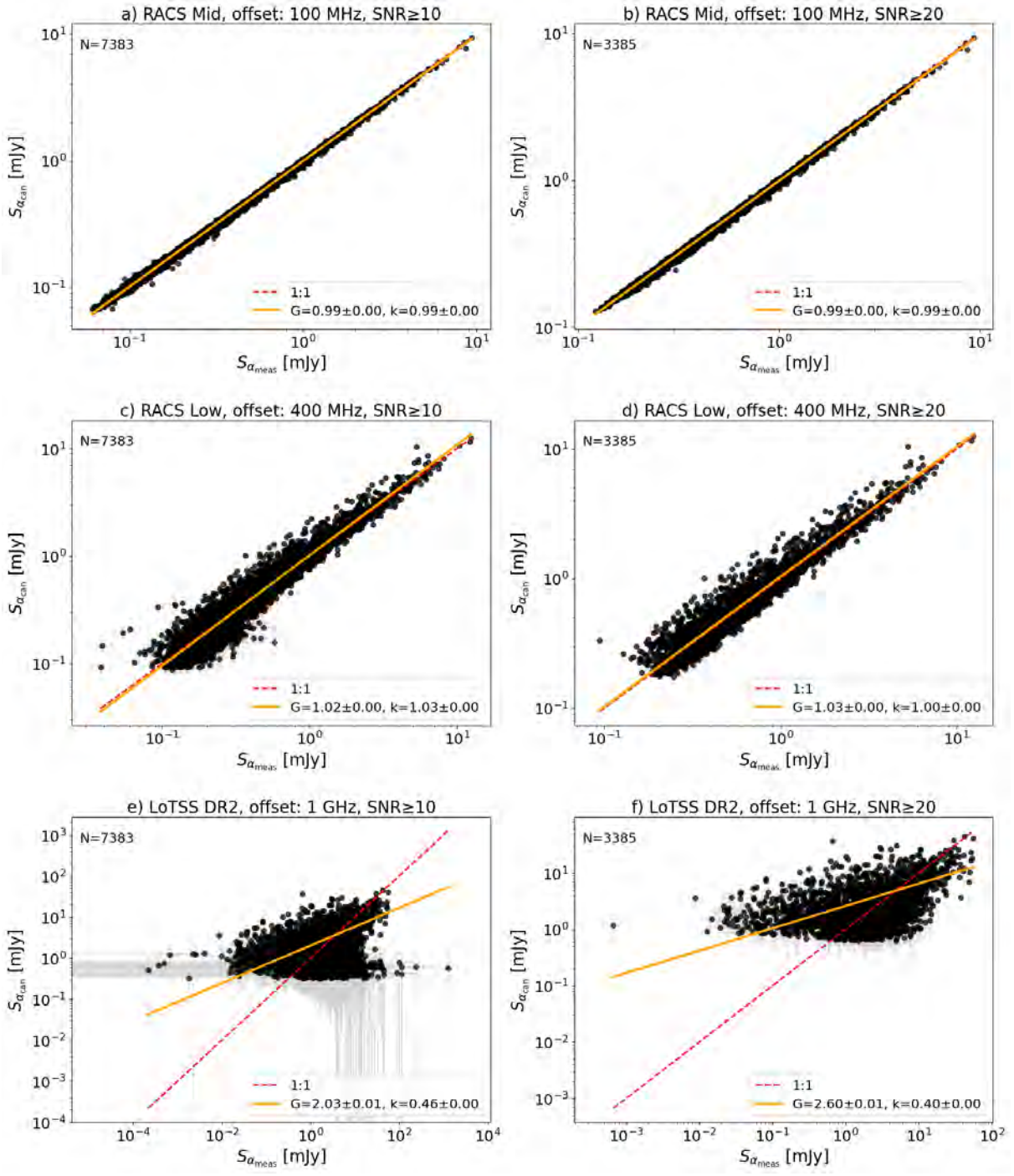

FIGURE 4.4: Comparison between flux densities extrapolated using $\alpha_{\text{can}} = -0.70 \pm 0.01$ and α_{meas} for radio sources at 100 MHz, 400 MHz and 1 GHz frequency offsets. The **left** column is SNR ≥ 10 and the **right** column is SNR ≥ 20. Each panel shows a log–log plot of $S_{\alpha_{\text{can}}}$ versus $S_{\alpha_{\text{meas}}}$ extrapolated from 1.28 GHz to **a** and **b:** RACS-Mid at 1377.5 MHz; **c** and **d:** RACS-Low at 887.5 MHz; and **e** and **f:** LoTSS DR2 at 144 MHz. The red dashed line indicates the 1:1 relationship, and the best fit relation for each case is shown by the solid orange line. At 1 GHz frequency offset, the fluxes extrapolated with $S_{\alpha_{\text{can}}}$ are overestimated by $\sim 100\%$, highlighting the inadequacy of the α_{can} assumption across wider frequency separation. N represents the number of sources above each SNR.

H

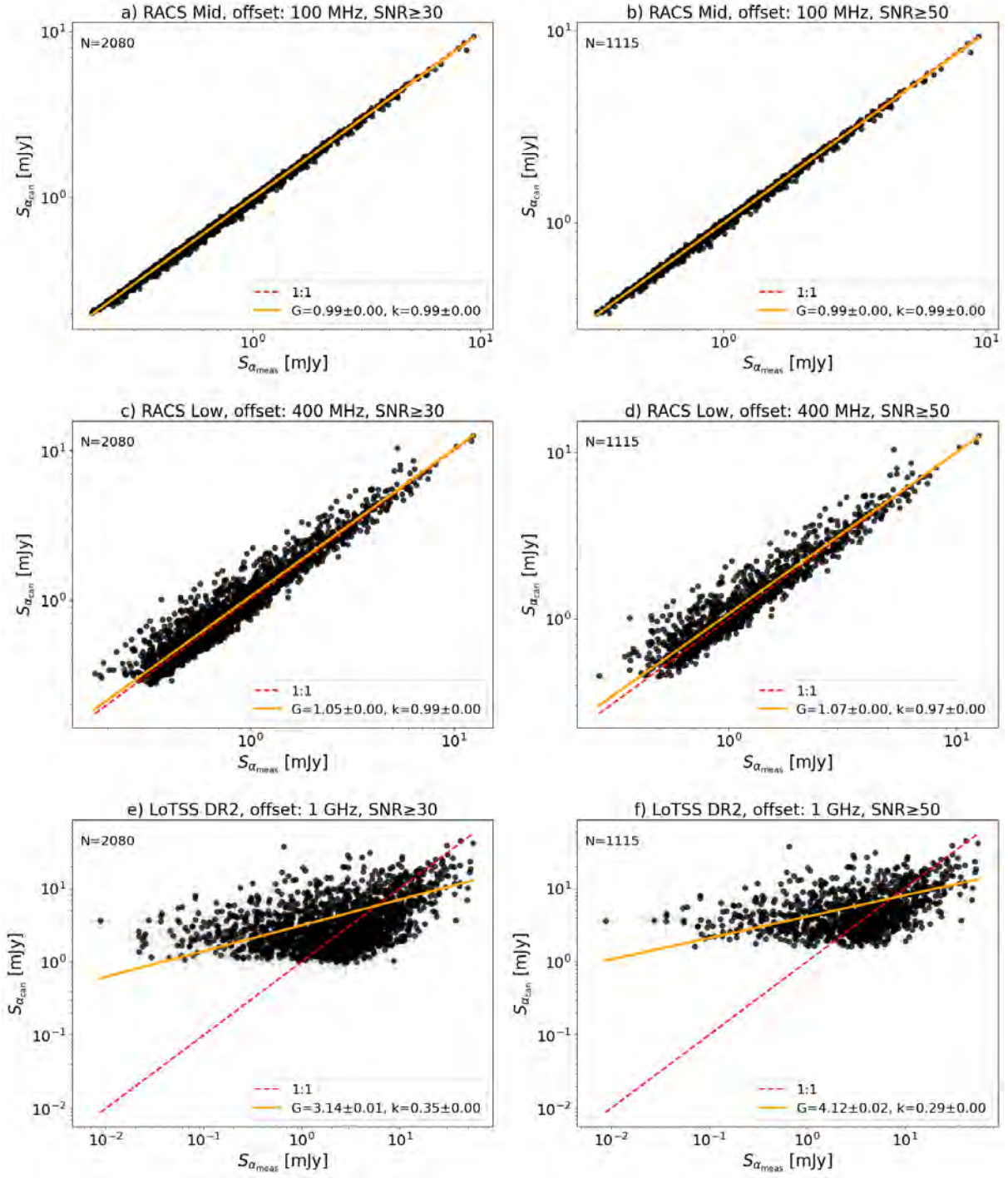

FIGURE 4.5: Comparison between flux densities extrapolated using $\alpha_{\text{can}} = -0.70 \pm 0.01$ and α_{meas} for radio sources at 100 MHz, 400 MHz and 1 GHz frequency offsets, as per Figure 4.4. The **left** column is SNR ≥ 30 and the **right** column is SNR ≥ 50. At 1 GHz frequency offset, the fluxes extrapolated with $S_{\alpha_{\text{can}}}$ are overestimated by $\sim 214\%$ and 312%, highlighting the inadequacy of the α_{can} assumption across wider frequency separation. N represents the number of sources above each SNR.

4.3 Conclusion

In this study, we find that assuming the literature's canonical synchrotron index for flux density extrapolation remains valid only under constrained conditions. For high-SNR sources (SNR $\geq$ 30) and narrow frequency separations ($\leq$ 100 MHz), the extrapolated fluxes deviate by less than 1%, well below the typical calibration or measurement uncertainties of radio telescopes. Under these circumstances, such as extrapolating MGCLS fluxes to the RACS-Mid band, a fixed canonical spectral index can serve as a rapid, first-order approximation without introducing significant bias.

When the frequency offset increases to $\sim$ 400 MHz, even high-SNR sources begin to exhibit systematic deviations of several per cent. These errors are comparable to, or larger than, the flux-scale uncertainties inherent to most instruments. Therefore, in precision studies that demand better than 5% accuracy, one should replace the canonical spectral index assumption with each source's measured in-band spectral index measurement.

Beyond 400 MHz offset, and especially at offsets approaching 1 GHz, the canonical spectral index fails to extrapolate accurate flux densities. Our results show flux overestimates of order 214 to 312%, respectively. This breakdown reflects the limitations of using the canonical spectral index assumption over a wide frequency separation. For any wide offset extrapolation in high-precision survey work, measured spectral indices must be used to avoid large systematic biases.

Chapter 5

Conclusion

We presented the results of a search for HzRG candidates using 30 of the 115 cluster fields of the MGCLS at 1.28 GHz. These fields were selected on the basis of their good dynamic range, astrometric accuracy, and complete optical and infrared coverage from DECaLS and AllWISE, respectively. Our multistage approach involved selecting unresolved radio sources, applying an SNR cut, identifying sources without DECaLS and AllWISE counterparts, and isolating USS sources ($\alpha < -1$).

We identified 1817 HzRG candidates (0.9% of the full sample), over a non-contiguous sky area of ≈ 43.2 deg^2. Of these, 777 satisfy the USS criterion, 767 via the LM method and 10 via `specfit`, while 1040 lack sufficient spectral data for in-band spectral index measurement, and remain potential candidates. This represents the largest and faintest population of HzRG candidates identified to date, including an unprecedented number of USS sources. Sources without spectral data will require additional observations to determine their spectral index, which can be achieved using MeerKAT's UHF band at MGCLS-like resolution with minimal telescope time.

We have complete spectral coverage for sources with flux densities above 0.76 mJy and spectral index estimates above a flux density threshold of 30 μJy, marking the lowest flux density population at GHz frequencies to be probed for the HzRGs search to date. This highlights the potential of MGCLS for identifying faint HzRG candidates, which can allow the exploration of HzRGs that are potentially more obscured and at higher redshifts, offering valuable insights into the early universe's massive galaxy formation and evolution.

This study demonstrates the potential of MGCLS to uncover faint HzRG candidates, which could help advance our understanding of the early universe. The upcoming deep, wide-area photometry from the Vera C. Rubin Observatory and Euclid, combined with future spectroscopic follow-up campaigns such as the 4MOST, will secure the redshift and the nature of these sources. To confirm the redshift and the nature of these candidates, spectroscopic follow-up observations are needed. High-quality photometric data can also provide valuable information on their properties. This work lays the foundation for these studies with the potential to provide a deeper understanding of the origin and evolution of radio galaxies at high redshift and their role in shaping the cosmic environment.

Taking advantage of the in-band spectral index measurements produced in this study, we compared the flux density extrapolations made using the literature's canonical synchrotron spectral index value of $\alpha = -0.7$ against those using each source's measured in-band spectral index at RACS-Mid, RACS-Low, and LoTSS DR2 frequencies, which are at 100 MHz, 400 MHz, and 1 GHz away from the MGCLS centre frequency, respectively. While the $\alpha = -0.7$ assumption did not affect the flux density extrapolation at 100 MHz frequency offset, it introduced a $\sim$7% deviation at 400 MHz frequency offset for high SNR sources and overestimated the flux densities by a factor of 4 at 1 GHz frequency offset. These results demonstrate that relying on the canonical spectral index for flux density extrapolation is only reliable for frequency offsets below 400 MHz and not reliable for frequency offsets around 1 GHz, even at high SNR.

Future work could explore whether there is a revised canonical spectral index for large frequency separations. For example, a joint MeerKAT–LOFAR study (outside the MGCLS footprint) could track how spectral curvature evolves from $\sim$50 MHz up to $\sim$1.4 GHz for thousands of sources, and the upcoming Square Kilometre Array (SKA)-Low and SKA-Mid surveys will deliver high-resolution, high-sensitivity catalogues spanning $>$1 GHz in bandwidth. Such efforts would not only quantify the frequency dependence of the spectral index but could establish new empirical prescriptions for flux extrapolation across very large frequency intervals.

Appendix A

Spectral Analysis

In this appendix, we give an overview of the methods used to fit models to the spectral data of radio sources to determine their spectral indices, focussingg on the Levenberg-Marquardt least-squares fitting procedure and `specfit`. These methods allow us to accurately model the flux density as a function of frequency and determine the spectral index of the sources, which is crucial for characterising their physical properties.

A.1 Single power-law fit

The weighted Levenberg-Marquardt (LM) least-squares fitting algorithm is a robust optimisation technique that combines the gradient descent and Gauss-Newton methods. We use it here to fit a power-law model spectrum of the form:

$$S_\nu \propto \nu^\alpha,$$

where:

- S_ν is the flux density at frequency ν,
- α is the spectral index, which quantifies the slope of the spectrum.

This method is particularly effective for datasets with measurement uncertainties, as it incorporates weights to account for errors in the flux density measurements.

Mathematical Basis

The fitting procedure minimizes the weighted sum of squared residuals:

$$\chi^2 = \sum_i w_i \left[S_{\nu,i} - S_{\nu,\text{model}}(\nu_i; \alpha) \right]^2 ,$$

where:

- $w_i = \frac{1}{\sigma_i^2}$ is the weight, determined by the uncertainty σ_i in the observed flux density $S_{\nu,i}$,
- $S_{\nu,\text{model}}(\nu_i; \alpha)$ is the model prediction for the flux density at frequency ν_i.

The Levenberg-Marquardt algorithm iteratively adjusts the spectral index α and other parameters (e.g., normalization) to minimize χ^2.

Python Implementation with `SciPy`

The Python package `SciPy` provides an efficient implementation of the Levenberg-Marquardt algorithm through the `scipy.optimize.curve_fit` function. Below is an example of fitting a power-law spectrum:

```
import numpy as np
from scipy.optimize import curve_fit

# Define the power-law model
def power_law(nu, alpha, S0):
    return S0 * (nu ** alpha)

# Example data: frequencies (nu), flux densities (S), and uncertainties (sigma)
nu = np.array([0.9, 1.0, 1.2, 1.4, 1.6, 1.8])  # GHz
S = np.array([0.3, 0.25, 0.22, 0.18, 0.15, 0.12])  # Jy
sigma = np.array([0.01, 0.015, 0.01, 0.012, 0.01, 0.013])  # Jy

# Perform the fit
```

```
popt, pcov = curve_fit(power_law, nu, S, sigma=sigma, absolute_sigma=True)

# Extract the fitted parameters and their uncertainties
alpha, S0 = popt
alpha_err, S0_err = np.sqrt(np.diag(pcov))

print(f"Fitted spectral index (alpha): {alpha:.3f} ± {alpha_err:.3f}")
print(f"Fitted normalization (S0): {S0:.3f} ± {S0_err:.3f}")
```

Results

The `curve_fit` function returns:

- `popt`: The optimized parameters (α and S_0).
- `pcov`: The covariance matrix, from which parameter uncertainties are derived.

This method accounts for measurement uncertainties (σ) through the weights, ensuring a more accurate and reliable fit, especially when errors vary between data points.

A.2 Broken power-law fit

The `specfit` package is a Python-based tool designed for the spectral analysis of astronomical data. It provides functionalities for piecewise linear fitting and statistical inference, making it an essential utility for analysing complex spectral datasets. The package facilitates reproducible and efficient analysis while offering flexibility for customisation.

Workflow for Using `specfit`

1. Preprocessing FITS Files The first step involves splitting a FITS file into individual JSON files, where each JSON corresponds to a single source. This is done with the following command:

```
python3 fits_analyze.py --fits="input_file" --output-dir="output"
```

This step enables easier access to and manipulation of the data for each source.

2. Performing Inference Once the FITS file has been split, the tool processes all JSON files to perform spectral inference. This step generates a summary file, `results.csv`, which includes key parameters such as spectral indices (slopes), their uncertainties, change points, and marginal likelihood values. The command for this step is:

```
python3 fits_analyze.py --fits="input_file" --output-dir="output" --process
```

3. Outputs and Visualisations For each source, `specfit` generates the following outputs in the specified directory:

- `_data.json`: Original source data.
- `_processed.json`: Results of the spectral inference, including fitted parameters and samples.
- Graphs:
  - Posterior plot of the samples.
  - Parameter correlation plots.
  - MCMC diagnostic plot showing traces of sampled parameters.

These outputs provide detailed information about the spectral properties and the fitting process.

Figure A.1 presents a gallery of radio spectra for 10 HzRG candidates, each exhibiting a broken power-law and USS low-frequency slopes. All of these sources are included in the final HzRG candidate list, see Chapter 4.

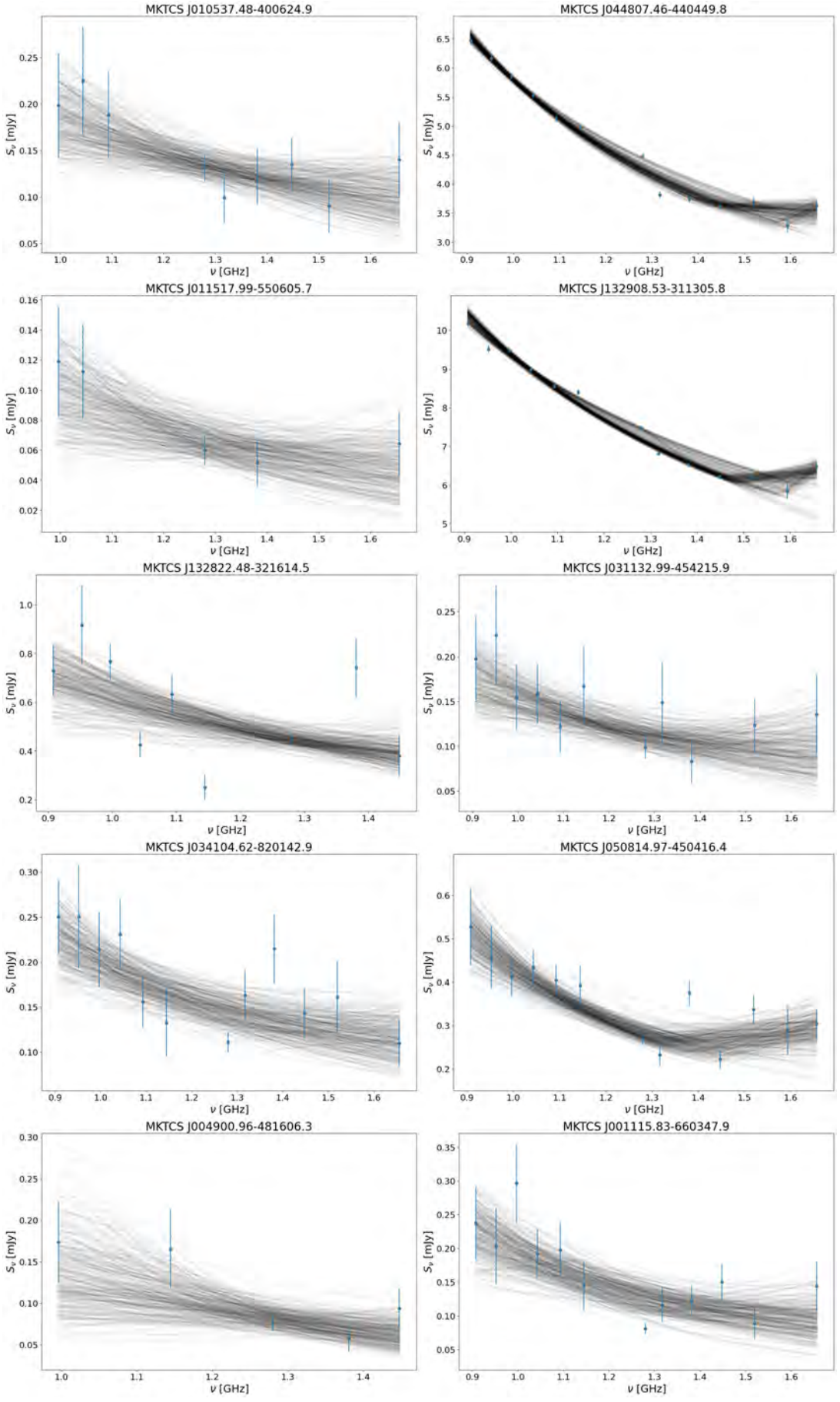

FIGURE A.1: Composite gallery of the radio spectra for ten HzRG candidates, each exhibiting a broken power-law, represented by multipole spline fits derived with `specfit`. These sources are USS at the lower frequency part of the spectrum.

RHODES UNIVERSITY
Where leaders learn

RESEARCH ETHICS DECLARATION

To be included in the Appendices of research papers / dissertations / theses submitted for postgraduate examination where research did not involve interaction with human participants, or the use of animal subjects, and therefore did not require research ethics approval.

Candidates whose research did require ethics clearance must include their ethics approval letter in the Appendix of their examination submission.

Name of Candidate: Vasco Cossa

Name of Supervisor: Kenda Knowles

Degree: Masters of Science

Title of research: High-redshift radio galaxy searches with the MeerKAT Galaxy Cluster Legacy Survey

DECLARATION

I declare that my research did not require ethical clearance because (tick all that apply):

I did not collect data from human participants or animal subjects	X
I used previously collected data that had already received ethics clearance.	
I analysed documents / open-access digital texts that are freely available in the public domain.	X
I did a literature review/analysis of theoretical or secondary material only.	
I used human datasets of non-sensitive information that are either anonymous (identifiers were never collected) or have been deidentified (identifiers have been completely removed).	
I used commercially produced human biological material (e.g. established human cell lines).	
I observed people in public spaces and natural environments where they had no reasonable expectation of privacy and I did not interact with them or intervene in any way.	
I used non-living animal materials (eg bones of already deceased organisms or fossils) while complying with any custody and/or jurisdiction requirements.	
I did a content analysis of public media (newspapers, advertisements, and social media posts).	
I did a simulation study with no real-world consequences and does not involve disturbing or distressing content.	
I observed flora, fauna, and ecosystems without interfering with or disturbing their natural state while complying with any jurisdiction requirements.	
Other (Please provide details):	

Signature of Candidate: Vasco Cossa
Date: 30/06/2025

Signature of Supervisor:

Date: 01 July 2025

Bibliography

Afonso, J., Bizzocchi, L., Ibar, E., Grossi, M., Simpson, C., Chapman, S., Jarvis, M. J., Rottgering, H., Norris, R. P., Dunlop, J., Ivison, R. J., Messias, H., Pforr, J., Vaccari, M., Seymour, N., Best, P., González-Solares, E., Farrah, D., Fernandes, C. A. C., Huang, J. S., Lacy, M., Maraston, C., Marchetti, L., Mauduit, J. C., Oliver, S., Rigopoulou, D., Stanford, S. A., Surace, J., and Zeimann, G. (2011). Ultra Steep Spectrum Radio Sources in the Lockman Hole: SERVS Identifications and Redshift Distribution at the Faintest Radio Fluxes. , 743(2):122.

Akima, H. (1970). A new method of interpolation and smooth curve fitting based on local procedures. *Journal of the ACM (JACM)*, 17(4):589–602.

Antonucci, R. (2011). Thermal and Nonthermal Radio Galaxies. *arXiv e-prints*, page arXiv:1101.0837.

Argo, M. K., Paragi, Z., Röttgering, H., et al. (2013). Probing the nature of compact ultrasteep spectrum radio sources with the e-EVN and e-MERLIN. *Monthly Notices of the Royal Astronomical Society: Letters*, 431(1):L58–L62.

Arshakian, T. G., Laboratory, M. S. L. C., and Observatory, B. (2000). An asymmetric relativistic model for classical double radio sources. *Monthly Notices of the Royal Astronomical Society*, 311:846–860.

Atek, H. et al. (2014). Probing the $z \sim 6$ universe with the first Hubble frontier fields cluster A2744. *The Astrophysical Journal*, 786(1):60.

Atek, H., Shuntov, M., Furtak, L. J., Richard, J., Kneib, J.-P., Mahler, G., Zitrin, A., McCracken, H., Charlot, S., Chevallard, J., et al. (2023). Revealing galaxy candidates out to $z \sim 16$ with JWST observations of the lensing cluster SMACS0723. *Monthly Notices of the Royal Astronomical Society*, 519(1):1201–1220.

Baade, W. and Minkowski, R. (1979). Identification of the radio sources in cassiopeia, cygnus a, and puppis a. In *A Source Book in Astronomy and Astrophysics, 1900–1975*, pages 786–791. Harvard University Press.

Bechtold, J., Green, R. F., Weymann, R. J., et al. (1984). IUE observations of high-redshift quasars. *Astrophysical Journal, Part 1 (ISSN 0004-637X), vol. 281, June 1, 1984, p. 76-89.*, 281:76–89.

Behiri, M., Giulietti, M., Galluzzi, V., et al. (2024). Teaming up Radio and Sub-mm/FIR Observations to Probe Dusty Star-Forming Galaxies. *Galaxies*, 12(2):14.

Bélopolsky, A. (1901). On an Apparatus for the Laboratory Demonstration of the Doppler-Fizeau Principle. , 13:15.

Belsole, E., Worrall, D. M., and Hardcastle, M. J. (2004). High redshift radio galaxies as tracers of galaxy clusters. XMM-Newton observations. In *Multiwavelength Cosmology: Proceedings of the "Multiwavelength Cosmology" Conference, held on Mykonos Island, Greece, 17–20 June, 2003*, pages 145–148. Springer.

Best, P. N., Kauffmann, G., Heckman, T., et al. (2005). A sample of radio-loud active galactic nuclei in the sloan digital sky survey. *Monthly Notices of the Royal Astronomical Society*, 362(1):9–24.

Biretta, J. A. and Meisenheimer, K. (1993). The jet of M 87.

Blecha, L., Snyder, G. F., Satyapal, S., et al. (2018). The power of infrared AGN selection in mergers: a theoretical study. , 478(3):3056–3071.

Blumenthal, G. and Miley, G. (1979). Spectral index dependent properties of steep spectrum radio sources. *Astronomy and Astrophysics, vol. 80, no. 1, Nov. 1979, p. 13-21. Research supported by the Martin Kellog Fund*, 80:13–21.

Blundell, K. M., Rawlings, S., Eales, S. A., Taylor, G. B., and Bradley, A. D. (1998). A sample of 6C radio sources designed to find objects at redshift z¿ 4—I. the radio data. *Monthly Notices of the Royal Astronomical Society*, 295(2):265–279.

Böhme, L., Schwarz, D. J., de Gasperin, F., Röttgering, H. J., and Williams, W. L. (2023). Matching LOFAR sources across radio bands. *Astronomy & Astrophysics*, 674:A189.

Bonzini, M., Mainieri, V., Padovani, P., et al. (2012). The sub-mjy radio population of the e-cdfs: optical and infrared counterpart identification. *The Astrophysical Journal Supplement Series*, 203(1):15.

Bornancini, C. G., Padilla, N. D., Lambas, D. G., and De Breuck, C. (2006). Spatial clustering of ultra steep spectrum sources and galaxies. *Monthly Notices of the Royal Astronomical Society*, 368(2):619–622.

Brandt, W. and Vito, F. (2017). High-redshift active galactic nuclei and the next decade of chandra and XMM-Newton. *Astronomische Nachrichten*, 338(2-3):241–248.

Brandt, W. N. and Hasinger, G. (2005). Deep extragalactic X-ray surveys. *Annu. Rev. Astron. Astrophys.*, 43(1):827–859.

Broderick, J., Bryant, J., Hunstead, R., Sadler, E., and Murphy, T. (2007). A new search for distant radio galaxies in the southern hemisphere–I. sample definition and radio properties. *Monthly Notices of the Royal Astronomical Society*, 381(1):341–366.

Broderick, J. J. and Condon, J. J. (1975). Compact components in a complete sample of extragalactic radio sources. , 202:596–602.

Broderick, J. W., Drouart, G., Seymour, N., et al. (2022). The GLEAMing of the first supermassive black holes: II. A new sample of high-redshift radio galaxy candidates. , 39:e061.

Bunker, A., Stanway, E., Ellis, R., McMahon, R., Eyles, L., and Lacy, M. (2006). Star forming galaxies at z 6 and reionization. *New Astronomy Reviews*, 50(1-3):94–100.

Burleigh, K. J., Landriau, M., Dey, A., et al. (2020). Dynamic Observing and Tiling Strategies for the DESI Legacy Surveys. *The Astronomical Journal*, 160(2):61.

Cai, Z., Nan, R., Schilizzi, R. T., et al. (2002). A 327 MHz VLBI study of high redshift radio galaxies 1345+245, 1809+407 and 2349+289. , 381:401–407.

Capetti, A. and Balmaverde, B. (2024). The radio properties of $z > 3.5$ quasars: Are most high-redshift radio-loud active galactic nuclei obscured? *Astronomy & Astrophysics*, 689:A174.

Carilli, C. and Yun, M. S. (2000). The scatter in the relationship between redshift and the radio-to-submillimeter spectral index. *The Astrophysical Journal*, 530(2):618.

Casey, C. M., Cooray, A., Killi, M., Capak, P., Chen, C.-C., Hung, C.-L., Kartaltepe, J., Sanders, D., and Scoville, N. (2017). Near-infrared MOSFIRE Spectra of Dusty Star-forming Galaxies at $0.2 < z < 4$. *The Astrophysical Journal*, 840(2):101.

Ciliegi, P., Zamorani, G., Hasinger, G., et al. (2003). A deep VLA survey at 6 cm in the Lockman Hole. *Astronomy & Astrophysics*, 398(3):901–918.

Cochrane, R. (2019). Resolving distant, dusty galaxies using observations and simulations. *Proceedings of the International Astronomical Union*, 15(S352):282–286.

Cohen, A., Röttgering, H., Jarvis, M., Kassim, N., and Lazio, T. (2004). A deep, high-resolution survey at 74 MHz. *The Astrophysical Journal Supplement Series*, 150(2):417.

Condon, J. (1992). Radio emission from normal galaxies. *In: Annual review of astronomy and astrophysics. Vol. 30 (A93-25826 09-90), p. 575-611.*, 30:575–611.

Condon, J., Cotton, W., White, S., et al. (2021). Threads, ribbons, and rings in the radio galaxy IC 4296. *The Astrophysical Journal*, 917(1):18.

Cruz, M. J., Jarvis, M. J., Blundell, K. M., Rawlings, S., Croft, S., Klöckner, H.-R., McLure, R. J., Simpson, C., Targett, T. A., and Willott, C. J. (2006). The C** sample of steep-spectrum radio sources–I. radio data, near-infrared imaging and optical spectroscopy. *Monthly Notices of the Royal Astronomical Society*, 373(4):1531–1562.

Dabhade, P., Saikia, D., and Mahato, M. (2023). Decoding the giant extragalactic radio sources. *Journal of Astrophysics and Astronomy*, 44:781–784.

Daddi, E., Cimatti, A., Renzini, A., Fontana, A., Mignoli, M., Pozzetti, L., Tozzi, P., and Zamorani, G. (2004). A new photometric technique for the joint selection of star-forming and passive galaxies at 1.4 $\geq z$ 2.5. *The Astrophysical Journal*, 617(2):746.

Daly, R. A. and Guerra, E. J. (2002). Quintessence, cosmology, and Fanaroff-Riley type IIb radio galaxies. *The Astronomical Journal*, 124(4):1831.

Davidson, W. (1962). The cosmological implications of the recent counts of radio sources: II. an evolutionary model. *Monthly Notices of the Royal Astronomical Society*, 124(1):79–93.

De Breuck, C., Hunstead, R. W., Sadler, E. M., Rocca-Volmerange, B., and Klamer, I. (2004). A search for distant radio galaxies from SUMSS and NVSSI. sample definition, radio and K-band imaging. *Monthly Notices of the Royal Astronomical Society*, 749(3):837–853.

De Breuck, C., Van Breugel, W., Röttgering, H., et al. (1998). Searches for high redshift radio galaxies. In *Observational Cosmology: With the New Radio Surveys Proceedings of a Workshop held in a Puerto de la Cruz, Tenerife, Canary Islands, Spain, 13–15 January 1997*, pages 185–190. Springer.

De Breuck, C., van Breugel, W., Röttgering, H., et al. (2001). Spectroscopy of Ultra-steep-Spectrum Radio Sources. , 121(3):1241–1265.

De Breuck, C., van Breugel, W., Röttgering, H. J. A., et al. (2000). A sample of 669 ultra steep spectrum radio sources to find high redshift radio galaxies. , 143:303–333.

De Breuck, C., van Breugel, W., Stanford, S., et al. (2002). Optical and near-infrde2000sampleared imaging of ultra-steep-spectrum radio sources: The K-z. diagram of radio-selected and optically selected galaxies. *The Astronomical Journal*, 123(2):637.

de Jong, R. S., Bellido-Tirado, O., Chiappini, C., Depagne, É., Haynes, R., Johl, D., Schnurr, O., Schwope, A., Walcher, J., Dionies, F., Haynes, D., Kelz, A., Kitaura, F. S., Lamer, G., Minchev, I., Müller, V., Nuza, S. E., Olaya, J.-C., Piffl, T., Popow, E., Steinmetz, M., Ural, U., Williams, M., Winkler, R., Wisotzki, L., Ansorge, W. R., Banerji, M., Gonzalez Solares, E., Irwin, M., Kennicutt, R. C., King, D., McMahon, R. G., Koposov, S., Parry, I. R., Sun, D., Walton, N. A., Finger, G., Iwert, O., Krumpe, M., Lizon, J.-L., Vincenzo, M., Amans, J.-P., Bonifacio, P., Cohen, M., Francois, P., Jagourel, P., Mignot, S. B., Royer, F., Sartoretti, P., Bender, R., Grupp, F., Hess, H.-J., Lang-Bardl, F., Muschielok, B., Böhringer, H., Boller, T., Bongiorno, A., Brusa, M., Dwelly, T., Merloni, A., Nandra, K., Salvato, M., Pragt, J. H., Navarro, R., Gerlofsma, G., Roelfsema, R., Dalton, G. B., Middleton, K. F., Tosh, I. A., Boeche, C., Caffau, E., Christlieb, N., Grebel, E. K., Hansen, C., Koch, A., Ludwig, H.-G., Quirrenbach, A., Sbordone, L., Seifert, W., Thimm, G., Trifonov, T., Helmi, A., Trager, S. C., Feltzing, S., Korn, A., and Boland, W. (2012). 4MOST: 4-metre multi-object spectroscopic telescope. In McLean, I. S., Ramsay, S. K., and Takami, H., editors, *Ground-based and Airborne Instrumentation for Astronomy IV*, volume 8446 of *Society of Photo-Optical Instrumentation Engineers (SPIE) Conference Series*, page 84460T.

De Zotti, G., Massardi, M., Negrello, M., and Wall, J. (2010). Radio and millimeter continuum surveys and their astrophysical implications. *The Astronomy and Astrophysics Review*, 18:1–65.

Dey, A., Schlegel, D. J., Lang, D., et al. (2019). Overview of the DESI legacy imaging surveys. *The Astronomical Journal*, 157(5):168.

Dickinson, M. (2016). The early phases of galaxy formation and evolution. In *AIP Conference Proceedings*, volume 1732. AIP Publishing.

Duchesne, S. W., Thomson, A. J. M., Pritchard, J., Lenc, E., Moss, V. A., McConnell, D., Wieringa, M. H., Whiting, M. T., Wang, Z., Wang, Y., Rose, K., Raja, W., Murphy,

T., Leung, J. K., Huynh, M. T., Hotan, A. W., Hodgson, T., and Heald, G. H. (2023). The Rapid ASKAP Continuum Survey IV: continuum imaging at 1367.5 MHz and the first data release of RACS-mid. , 40:e034.

Duffy, P. and Blundell, K. M. (2012). The non-thermal emission of extended radio galaxy lobes with curved electron spectra. *Monthly Notices of the Royal Astronomical Society*, 421(1):108–11.

Dwarakanath, K. S. and Kale, R. (2009). Steep-Spectrum Sources from the VLA 74 MHz Survey. In Saikia, D. J., Green, D. A., Gupta, Y., and Venturi, T., editors, *The Low-Frequency Radio Universe*, volume 407 of *Astronomical Society of the Pacific Conference Series*, page 162.

Ekers, R. (1978). Radio observations of active and normal nuclei. *Physica Scripta*, 17(3):171.

Fan, X. (2012). Observations of the first light and the epoch of reionization. *Research in Astronomy and Astrophysics*, 12(8):865.

Friedmann, A. (1924). Über die möglichkeit einer welt mit konstanter negativer krümmung des raumes. *Zeitschrift für Physik*, 21(1):326–332.

Gabuzda, D. C. (2015). Parsec-scale jets in active galactic nuclei.

Galametz, A., Stern, D., De Breuck, C., et al. (2012). The mid-infrared environments of high-redshift radio galaxies. *The Astrophysical Journal*, 749(2):169.

Gardner, J. P., Mather, J. C., Abbott, R., Abell, J. S., Abernathy, M., Abney, F. E., Abraham, J. G., Abraham, R., Abul-Huda, Y. M., Acton, S., et al. (2023). The James Webb Space Telescope mission. *Publications of the Astronomical Society of the Pacific*, 135(1048):068001.

Ghisellini, G., Celotti, A., Tavecchio, F., Haardt, F., and Sbarrato, T. (2014). Radio-loud active galactic nuclei at high redshifts and the cosmic microwave background. *Monthly Notices of the Royal Astronomical Society*, 438(3):2694–2700.

Gopal-Krishna (1988). An investigation of the redshift-dependence of the radio spectral index among powerful double radio sources. , 192:37–41.

Herzog, A., Middelberg, E., Norris, R. P., et al. (2014). Infrared-faint radio sources are at high redshifts-spectroscopic redshift determination of infrared-faint radio sources using the very large telescope. *Astronomy & Astrophysics*, 567:A104.

Hodges-Kluck, E., Gallo, E., Ghisellini, G., Haardt, F., Wu, J., and Ciardi, B. (2021). Proof of CMB-driven X-ray brightening of high-z radio galaxies. *Monthly Notices of the Royal Astronomical Society*, 505(1):1543–1556.

Hubble, E. (1929). A relation between distance and radial velocity among extra-galactic nebulae. *Proceedings of the national academy of sciences*, 15(3):168–173.

Huggins, W. (1868). XXI. Further observations on the spectra of some the stars and nebulæ, with an attempt to determine therefrom whether these bodies are moving towards or from the earth, also observations on the spectra of the sun and of comet ii., 1868. *Philosophical Transactions of the Royal Society of London*, (158):529–564.

Hurley-Walker, N., Callingham, J. R., Hancock, P. J., Franzen, T. M. O., Hindson, L., Kapińska, A. D., Morgan, J., Offringa, A. R., Wayth, R. B., Wu, C., Zheng, Q., Murphy, T., Bell, M. E., Dwarakanath, K. S., For, B., Gaensler, B. M., Johnston-Hollitt, M., Lenc, E., Procopio, P., Staveley-Smith, L., Ekers, R., Bowman, J. D., Briggs, F., Cappallo, R. J., Deshpande, A. A., Greenhill, L., Hazelton, B. J., Kaplan, D. L., Lonsdale, C. J., McWhirter, S. R., Mitchell, D. A., Morales, M. F., Morgan, E., Oberoi, D., Ord, S. M., Prabu, T., Shankar, N. U., Srivani, K. S., Subrahmanyan, R., Tingay, S. J., Webster, R. L., Williams, A., and Williams, C. L. (2017). GaLactic and Extragalactic All-sky Murchison Widefield Array (GLEAM) Survey - I. A low-frequency extragalactic catalogue. , 464(1):1146–1167.

Intema, H., Jagannathan, P., Mooley, K., and Frail, D. (2017). The GMRT 150 MHz all-sky radio survey-first alternative data release TGSS ADR1. *Astronomy & Astrophysics*, 598:A78.

Ishwara-Chandra, C., Taylor, A., Green, D., et al. (2020). A wide-area GMRT 610-MHz survey of ELAIS N1 field. *Monthly Notices of the Royal Astronomical Society*, 497(4):5383–5394.

Ishwara-Chandra, C. H., Sirothia, S. K., Wadadekar, Y., et al. (2010). Deep GMRT 150-MHz observations of the LBDS-Lynx region: ultrasteep spectrum radio sources. , 405(1):436–446.

Ivezić, Ž., Kahn, S. M., Tyson, J. A., Abel, B., Acosta, E., Allsman, R., Alonso, D., AlSayyad, Y., Anderson, S. F., Andrew, J., Angel, J. R. P., Angeli, G. Z., Ansari, R., Antilogus, P., Araujo, C., Armstrong, R., Arndt, K. T., Astier, P., Aubourg, É., Auza, N., Axelrod, T. S., Bard, D. J., Barr, J. D., Barrau, A., Bartlett, J. G., Bauer, A. E., Bauman, B. J., Baumont, S., Bechtol, E., Bechtol, K., Becker, A. C.,

Becla, J., Beldica, C., Bellavia, S., Bianco, F. B., Biswas, R., Blanc, G., Blazek, J., Blandford, R. D., Bloom, J. S., Bogart, J., Bond, T. W., Booth, M. T., Borgland, A. W., Borne, K., Bosch, J. F., Boutigny, D., Brackett, C. A., Bradshaw, A., Brandt, W. N., Brown, M. E., Bullock, J. S., Burchat, P., Burke, D. L., Cagnoli, G., Calabrese, D., Callahan, S., Callen, A. L., Carlin, J. L., Carlson, E. L., Chandrasekharan, S., Charles-Emerson, G., Chesley, S., Cheu, E. C., Chiang, H.-F., Chiang, J., Chirino, C., Chow, D., Ciardi, D. R., Claver, C. F., Cohen-Tanugi, J., Cockrum, J. J., Coles, R., Connolly, A. J., Cook, K. H., Cooray, A., Covey, K. R., Cribbs, C., Cui, W., Cutri, R., Daly, P. N., Daniel, S. F., Daruich, F., Daubard, G., Daues, G., Dawson, W., Delgado, F., Dellapenna, A., de Peyster, R., de Val-Borro, M., Digel, S. W., Doherty, P., Dubois, R., Dubois-Felsmann, G. P., Durech, J., Economou, F., Eifler, T., Eracleous, M., Emmons, B. L., Fausti Neto, A., Ferguson, H., Figueroa, E., Fisher-Levine, M., Focke, W., Foss, M. D., Frank, J., Freemon, M. D., Gangler, E., Gawiser, E., Geary, J. C., Gee, P., Geha, M., Gessner, C. J. B., Gibson, R. R., Gilmore, D. K., Glanzman, T., Glick, W., Goldina, T., Goldstein, D. A., Goodenow, I., Graham, M. L., Gressler, W. J., Gris, P., Guy, L. P., Guyonnet, A., Haller, G., Harris, R., Hascall, P. A., Haupt, J., Hernandez, F., Herrmann, S., Hileman, E., Hoblitt, J., Hodgson, J. A., Hogan, C., Howard, J. D., Huang, D., Huffer, M. E., Ingraham, P., Innes, W. R., Jacoby, S. H., Jain, B., Jammes, F., Jee, M. J., Jenness, T., Jernigan, G., Jevremović, D., Johns, K., Johnson, A. S., Johnson, M. W. G., Jones, R. L., Juramy-Gilles, C., Jurić, M., Kalirai, J. S., Kallivayalil, N. J., Kalmbach, B., Kantor, J. P., Karst, P., Kasliwal, M. M., Kelly, H., Kessler, R., Kinnison, V., Kirkby, D., Knox, L., Kotov, I. V., Krabbendam, V. L., Krughoff, K. S., Kubánek, P., Kuczewski, J., Kulkarni, S., Ku, J., Kurita, N. R., Lage, C. S., Lambert, R., Lange, T., Langton, J. B., Le Guillou, L., Levine, D., Liang, M., Lim, K.-T., Lintott, C. J., Long, K. E., Lopez, M., Lotz, P. J., Lupton, R. H., Lust, N. B., MacArthur, L. A., Mahabal, A., Mandelbaum, R., Markiewicz, T. W., Marsh, D. S., Marshall, P. J., Marshall, S., May, M., McKercher, R., McQueen, M., Meyers, J., Migliore, M., Miller, M., and Mills, D. J. (2019). LSST: From Science Drivers to Reference Design and Anticipated Data Products. , 873(2):111.

Iye, M. (2008). High redshift galaxy surveys. In *Observatory Operations: Strategies, Processes, and Systems II*, volume 7016, pages 17–26. SPIE.

Jansen, F., Lumb, D., Altieri, B., Clavel, J., Ehle, M., Erd, C., Gabriel, C., Guainazzi, M., Gondoin, P., Much, R., et al. (2001). XMM-Newton observatory-I. the spacecraft and operations. *Astronomy & Astrophysics*, 365(1):L1–L6.

Jarvis, M. J., Cruz, M. J., Cohen, A. S., Röttgering, H. J., and Kassim, N. E. (2004). Near-infrared K-band imaging of a sample of ultra-steep-spectrum radio sources selected at 74 MHz. *Monthly Notices of the Royal Astronomical Society*, 355(1):20–30.

Jonas, J. and MeerKAT Team (2016). The MeerKAT Radio Telescope. In *MeerKAT Science: On the Pathway to the SKA*, page 1.

Jurlin, N., Morganti, R., Brienza, M., et al. (2020). The life cycle of radio galaxies in the lofar lockman hole field. *Astronomy & Astrophysics*, 638:A34.

Kaifu, N. (1998). Subaru Telescope. In *Advanced Technology Optical/IR Telescopes VI*, volume 3352, pages 14–22. SPIE.

Kaviraj, S., Khochfar, S., Schawinski, K., Yi, S., Gawiser, E., Silk, J., Virani, S., Cardamone, C., Van Dokkum, P., and Urry, C. (2008). The UV colours of high-redshift early-type galaxies: evidence for recent star formation and stellar mass assembly over the last 8 billion years. , 388(1):67–79.

Kellermann, K. (2014). The discovery of quasars and its aftermath. *Journal of Astronomical History and Heritage*, 17(3):267–282.

Kellermann, K. I. (1964). The spectra of non-thermal radio sources. *Astrophysical Journal, vol. 140, p. 969*, 140:969.

Ker, L., Best, P., Rigby, E., et al. (2012). New insights on the z–α correlation from complete radio samples. *Monthly Notices of the Royal Astronomical Society*, 420(3):2644–2661.

Knowles, K., Cotton, W. D., Rudnick, L., et al. (2022). The MeerKAT Galaxy Cluster Legacy Survey. I. Survey Overview and Highlights. , 657:A56.

Knowles, K., Manaka, S., Bietenholz, M. F., et al. (2021). Searching for High–z Radio Galaxies with the MGCLS. *Galaxies*, 9(4):89.

Kokorev, V., Fujimoto, S., Labbe, I., Greene, J. E., Bezanson, R., Dayal, P., Nelson, E. J., Atek, H., Brammer, G., Caputi, K. I., Chemerynska, I., Cutler, S. E., Feldmann, R., Fudamoto, Y., Furtak, L. J., Goulding, A. D., de Graaff, A., Leja, J., Marchesini, D., Miller, T. B., Nanayakkara, T., Oesch, P. A., Pan, R., Price, S. H., Setton, D. J., Smit, R., Stefanon, M., Wang, B., Weaver, J. R., Whitaker, K. E., Williams, C. C., and Zitrin, A. (2023). UNCOVER: A NIRSpec Identification of a Broad-line AGN at z = 8.50. , 957(1):L7.

Krishna, G., Sirothia, S. K., Mhaskey, M., Ranadive, P., Wiita, P. J., Goyal, A., Kantharia, N. G., and Ishwara-Chandra, C. (2014). Extragalactic radio sources with sharply inverted spectrum at metre wavelengths. *Monthly Notices of the Royal Astronomical Society*, 443(3):2824–2829.

Krolik, J. H. and Chen, W. (1991). Steep Radio Spectra in High-Redshift Radio Galaxies. , 102:1659.

Kurcz, A., Bilicki, M., Solarz, A., Krupa, M., Pollo, A., and Małek, K. (2016). Towards automatic classification of all WISE sources. , 592:A25.

Laing, R. and Peacock, J. (1980). The relation between radio luminosity and spectrum for extended extragalactic radio sources. *Monthly Notices of the Royal Astronomical Society, vol. 190, Mar. 1980, p. 903-924. Research supported by the Science Research Council.*, 190:903–924.

LaMassa, S. M., Heckman, T. M., Ptak, A., et al. (2009). XMM-Newton Observations of a Complete Sample of Optically Selected Type 2 Seyfert Galaxies. , 705(1):568–586.

Levenberg, K. (1944). A method for the solution of certain non-linear problems in least squares. *Quarterly of applied mathematics*, 2(2):164–168.

Li, J., Huang, S., Leauthaud, A., et al. (2022). Reaching for the Edge I: probing the outskirts of massive galaxies with HSC, DECaLS, SDSS, and Dragonfly. *Monthly Notices of the Royal Astronomical Society*, 515(4):5335–5357.

Lister, M. L., Hutchings, J., and Gower, A. C. (1994). Orientation modeling of radio galaxy and quasar properties: Evidence for a unified model. *Astrophysical Journal, Part 1 (ISSN 0004-637X), vol. 427, no. 1, p. 125-133*, 427:125–133.

Mainzer, A. K., Eisenhardt, P., Wright, E. L., et al. (2006). Update on the Wide-Field Infrared Survey Explorer (WISE). In *Space Telescopes and Instrumentation I: Optical, Infrared, and Millimeter*, volume 6265, pages 661–672. SPIE.

Marquardt, D. W. (1963). An algorithm for least-squares estimation of nonlinear parameters. *Journal of the society for Industrial and Applied Mathematics*, 11(2):431–441.

Marscher, A. (1977). Structure of radio sources with remarkably flat spectra-pks 0735+ 178. *Astrophysical Journal*, 82:781–784.

McCarthy, P., Kapahi, V., Breugel, W. v., et al. (1990). High-redshift radio galaxies from the Molonglo Catalogue. *Astronomical Journal*, 100(4):1014–1027.

Mellier, Y., Abdurroúf, A., Barroso, J. A., Achúcarro, A., Adamek, J., Adam, R., Addison, G., Aghanim, N., Aguena, M., Ajani, V., et al. (2024). Euclid. I. Overview of the Euclid mission. *arXiv e-prints*, page arXiv:2405.13491.

Miley, G. and De Breuck, C. (2008). Distant radio galaxies and their environments. *The Astronomy and Astrophysics Review*, 15:67–144.

Miley, G. K. (1968). Variation of the angular sizes of quasars with red-shift. *Nature*, 218(5145):933–934.

Miley, G. K., Overzier, R. A., Zirm, A. W., et al. (2006). The spiderweb galaxy: A forming massive cluster galaxy at $z \sim 2$. *The Astrophysical Journal*, 650(1):L29.

Minkowski, R. (1960). A new distant cluster of galaxies. *Astrophysical Journal, vol. 132, p. 908-910*, 132:908–910.

Miraghaei, H. and Best, P. (2017). The nuclear properties and extended morphologies of powerful radio galaxies: the roles of host galaxy and environment. *Monthly Notices of the Royal Astronomical Society*, 466:4346–4363.

Moffet, A. T. (1966). The structure of radio galaxies. *Annual Review of Astronomy and Astrophysics, vol. 4, p. 145*, 4:145.

Molteno, T. C. (2024). Correlation structure in flux-density calibrator models. *Monthly Notices of the Royal Astronomical Society*, 527(3):5732–5740.

Morabito, L. K. and Harwood, J. J. (2018). Investigating the cause of the α–z relation. , 480(2):2726–2732.

Morabito, L. K., Williams, W., Duncan, K. J., et al. (2017). Investigating the unification of LOFAR-detected powerful AGN in the boötes field. *Monthly Notices of the Royal Astronomical Society*, 469(2):1883–1896.

Morganti, R. (2024). What have we learned about the life cycle of radio galaxies from new radio surveys. *Galaxies*, 12(2):11.

Morganti, R., Oosterloo, T., Reynolds, J., et al. (1997). A study of cores in a complete sample of radio sources. *Monthly Notices of the Royal Astronomical Society*, 284(3):541–551.

Morishita, T., Stiavelli, M., Chary, R.-R., Trenti, M., Bergamini, P., Chiaberge, M., Leethochawalit, N., Roberts-Borsani, G., Shen, X., and Treu, T. (2024). Enhanced

Subkiloparsec-scale Star Formation: Results from a JWST Size Analysis of 341 Galaxies at $5 < z < 14$. , 963(1):9.

Myers, A. D., Moustakas, J., Bailey, S., et al. (2023). The Target-selection Pipeline for the Dark Energy Spectroscopic Instrument. *The Astronomical Journal*, 165(2):50.

Natarajan, P., Pacucci, F., Ricarte, A., Bogdán, Á., Goulding, A. D., and Cappelluti, N. (2024). First Detection of an Overmassive Black Hole Galaxy UHZ1: Evidence for Heavy Black Hole Seed Formation from Direct Collapse. , 960(1):L1.

Neeser, M. J., Eales, S. A., Law-Green, J. D., et al. (1995). The linear-size evolution of classical double radio sources. *arXiv preprint astro-ph/9508036*.

Nemiroff, R. J. and Patla, B. (2008). Adventures in Friedmann cosmology: A detailed expansion of the cosmological Friedmann equations. *American Journal of Physics*, 76(3):265–276.

Niu, Q., Li, Y., Xu, Y., Guo, H., and Zhang, X. (2025). Prospects for observing high-redshift radio-loud quasars in the ska era: paving the way for 21 cm forest observations. *The Astrophysical Journal*, 978(2):145.

Ogle, P., Whysong, D., and Antonucci, R. (2006). Spitzer reveals hidden quasar nuclei in some powerful FR II radio galaxies. *The Astrophysical Journal*, 647(1):161.

Orenstein, B. J., Collier, J. D., and Norris, R. P. (2019). The redshift distribution of infrared-faint radio sources. , 484(1):1021–1030.

Owen, F. N. and Puschell, J. J. (1984). VLA observations of Jodrell Bank radio quasars. *Astronomical Journal (ISSN 0004-6256), vol. 89, July 1984, p. 932-957.*, 89:932–957.

O'Dea, C. P. and Baum, S. A. (2023). Wide-angle-tail (WAT) radio sources. *Galaxies*, 11(3):67.

Pacholczyk, A. G. (1970). *Radio astrophysics. Nonthermal processes in galactic and extragalactic sources*.

Pedani, M. (2003). On the efficiency of the ultra steep spectrum technique in finding high–z radiogalaxies. *New Astronomy*, 8(8):805–815.

Pentericci, L., Van Reeven, W., Carilli, C., et al. (2000). VLA radio continuum observations of a new sample of high redshift radio galaxies. *Astronomy and Astrophysics Supplement Series*, 145(1):121–159.

Perley, R., Fomalont, E., and Johnston, K. (1982). The extended radio structure of compact extragalactic sources. *Astrophysical Journal*, 255:L93–L97.

Perlman, E. S., Biretta, J. A., Zhou, F., et al. (1999). Optical and radio polarimetry of the m87 jet at 02 resolution. *The Astronomical Journal*, 117(5):2185.

Prandoni, I., Gregorini, L., Parma, P., et al. (2000). The ATESP radio survey-II. the source catalogue. *Astronomy and Astrophysics Supplement Series*, 146(1):41–55.

Preston, R. A., Morabito, D. D., and Jauncey, D. L. (1983). A statistical VLBI study of milli-arcsecond cores in extragalactic radio sources. *Astrophysical Journal, Part 1 (ISSN 0004-637X), vol. 269, June 15, 1983, p. 387-399.*, 269:387–399.

Prieto, M. A., Brunetti, G., and Mack, K. H. (2002). Particle accelerators in the hot spots of radio galaxy 3C 445, imaged with the VLT. *Science*, 298:193–195.

Pyrzas, S., Steenbrugge, K. C., and Blundell, K. M. (2015). Multiwavelength study of Cygnus A - V. the hotspots in the lobe. *Astronomy and Astrophysics*, 574.

Readhead, A. and Pearson, T. (1982). The milliarcsecond structure of radio galaxies and quasars. *Symposium-International Astronomical Union*, 97:279–288.

Rhoads, J. E., Malhotra, S., Dey, A., Jannuzi, B. T., Stern, D., and Spinrad, H. (2001). The large area lyman alpha survey. *arXiv preprint astro-ph/0104294*.

Riguccini, L., Le Floc'h, E., Ilbert, O., Aussel, H., Salvato, M., Capak, P., McCracken, H., Kartaltepe, J., Sanders, D., and Scoville, N. (2011). Dust-obscured star formation and the contribution of galaxies escaping UV/optical color selections at $z \sim 2$. *Astronomy & Astrophysics*, 534:A81.

Rocca-Volmerange, B., Drouart, G., De Breuck, C., et al. (2013). Starburst and old stellar populations in the $z = 3.8$ radio galaxies 4C 41.17 and TN J20071316. *Monthly Notices of the Royal Astronomical Society*, 429(4):2780–2790.

Rocca-Volmerange, B., Le Borgne, D., De Breuck, C., et al. (2004). The radio galaxy Kz relation: The $M_{\odot}$ mass limit-masses of galaxies from the L luminosity, up to z. *Astronomy and Astrophysics*, 415(3):931–940.

Rogstad, D. and Ekers, R. (1969). Radio Sources and Elliptical Galaxies. *Astrophysical Journal, vol. 157, p. 481*, 157:481.

Roseboom, I. G., Oliver, S., Parkinson, D., et al. (2009). A new approach to multiwavelength associations of astronomical sources. *Monthly Notices of the Royal Astronomical Society*, 400(2):1062–1074.

Röttgering, H., Best, P., Pentericci, L., et al. (1999). Distant radio galaxies: Probes of the formation of massive galaxies. In *Symposium-International Astronomical Union*, volume 186, pages 471–474. Cambridge University Press.

Sadler, E. M., Jackson, C. A., Cannon, R. D., et al. (2002). Radio sources in the 2dF galaxy redshift survey-II. local radio luminosity functions for AGN and star-forming galaxies at 1.4 GHz. *Monthly Notices of the Royal Astronomical Society*, 329(1):227–245.

Saikia, D. (2022). Jets in radio galaxies and quasars: an observational perspective. *Journal of Astrophysics and Astronomy*, 43(2):97.

Sakelliou, I. and Merrifield, M. R. (2000). The origin of wide-angle tailed radio galaxies. , 311(3):649–656.

Salmon, B., Papovich, C., Finkelstein, S. L., Tilvi, V., Finlator, K., Behroozi, P., Dahlen, T., Davé, R., Dekel, A., Dickinson, M., et al. (2015). The relation between star formation rate and stellar mass for galaxies at $3.5 \leq z \leq 6.5$ in CANDELS. *The Astrophysical Journal*, 799(2):183.

Santos, J. S., Fassbender, R., Nastasi, A., Böhringer, H., Rosati, P., Šuhada, R., Pierini, D., Nonino, M., Mühlegger, M., Quintana, H., Schwope, A. D., Lamer, G., de Hoon, A., and Strazzullo, V. (2011). Discovery of a massive X-ray luminous galaxy cluster at z = 1.579. , 531:L15.

Saxena, A., Jagannathan, P., Röttgering, H., et al. (2018a). A search for faint high-redshift radio galaxy candidates at 150 MHz. *Monthly Notices of the Royal Astronomical Society*, 475(4):5041–5058.

Saxena, A., Marinello, M., Overzier, R., et al. (2018b). Discovery of a radio galaxy at z= 5.72. *Monthly Notices of the Royal Astronomical Society*, 480(2):2733–2742.

Saxena, A., Röttgering, H., Duncan, K., et al. (2019). The nature of faint radio galaxies at high redshifts. *Monthly Notices of the Royal Astronomical Society*, 489(4):5053–5075.

Schmidt, M. (1963). 3C 273 : A Star-Like Object with Large Red-Shift. , 197(4872):1040.

Schmidt, S. J., Connolly, A., and Hopkins, A. M. (2006). The DRaGONS survey: a search for high-redshift radio galaxies and heavily obscured active galactic nuclei. *The Astrophysical Journal*, 649(1):63.

Shapley, A. E. (2011). Physical properties of galaxies from $z = 2$–4. *Annual Review of Astronomy and Astrophysics*, 49(1):525–580.

She, R., Ho, L. C., and Feng, H. (2017). Chandra Survey of Nearby Galaxies: The Catalog. *The Astrophysical Journal*, 835(2):223.

Shen, X., Vogelsberger, M., Nelson, D., Tacchella, S., Hernquist, L., Springel, V., Marinacci, F., and Torrey, P. (2022). High-redshift predictions from illustristng–iii. infrared luminosity functions, obscured star formation, and dust temperature of high-redshift galaxies. *Monthly Notices of the Royal Astronomical Society*, 510(4):5560–5578.

Shimwell, T., Hardcastle, M., Tasse, C., Best, P., Röttgering, H., Williams, W., Botteon, A., Drabent, A., Mechev, A., Shulevski, A., et al. (2022). The LOFAR two-metre sky survey-V. second data release. *Astronomy & astrophysics*, 659:A1.

Silverstein, E. M. (2015). Double-lobed radio galaxies and the intragroup medium.

Silverstein, E. M., Anderson, M. E., and Bregman, J. N. (2017). Increased prevalence of bent lobes for double-lobed radio galaxies in dense environments. *The Astronomical Journal*, 155.

Simpson, C., Dunlop, J., Eales, S. A., Ivison, R., Scott, S., Lilly, S., and Webb, T. (2004). Deep near-infrared spectroscopy of submillimetre-selected galaxies. *Monthly Notices of the Royal Astronomical Society*, 353(1):179–188.

Singal, A. K. and Singh, R. L. (2013). Unification scheme of radio galaxies and quasars falsified by their observed size distributions. *The Astrophysical Journal*, 766(1):37.

Singh, V., Beelen, A., Wadadekar, Y., et al. (2014). Multiwavelength characterization of faint ultra steep spectrum radio sources: A search for high-redshift radio galaxies. *Astronomy & Astrophysics*, 569:A52.

Singh, V., Chand, H., Ishwara-Chandra, C., et al. (2018). Kpc-scale radio-jets in narrow-line Seyfert 1 galaxies. *arXiv preprint arXiv:1807.05179*.

Singh, V., Dutta, S., Wadadekar, Y., and Ishwara-Chandra, C. (2021). Remnant radio galaxy candidates of small angular sizes. *Galaxies*, 9(4):121.

Spinrad, H. (1982). Redshifts and spectroscopy of very distant radio galaxies with strong emission lines. *Publications of the Astronomical Society of the Pacific*, 94(559):397.

Stark, D. P. (2016). Galaxies in the first billion years after the big bang. *Annual Review of Astronomy and Astrophysics*, 54(1):761–803.

Steidel, C. C., Adelberger, K. L., Shapley, A. E., Pettini, M., Dickinson, M., and Giavalisco, M. (2003). Lyman break galaxies at redshift $z \sim$3: survey description and full data set. *The Astrophysical Journal*, 592(2):728.

Stern, D., Assef, R. J., Benford, D. J., Blain, A., Cutri, R., Dey, A., Eisenhardt, P., Griffith, R. L., Jarrett, T., Lake, S., et al. (2012). Mid-infrared selection of active galactic nuclei with the wide-field infrared survey explorer. I. characterizing wise-selected active galactic nuclei in cosmos. *The Astrophysical Journal*, 753(1):30.

Stern, D., Dey, A., Spinrad, H., et al. (1999). New high-redshift radio galaxies from the mit-green bank catalogue. *The Astronomical Journal*, 117(3):1122.

Stevens, J. A., Ivison, R., Dunlop, J., et al. (2003). The formation of cluster elliptical galaxies as revealed by extensive star formation. *Nature*, 425(6955):264–267.

Sutherland, W. and Saunders, W. (1992). On the Likelihood Ratio for source identification. *Monthly Notices of the Royal Astronomical Society*, 259(3):413–420.

Talia, M., Cimatti, A., Giulietti, M., Zamorani, G., Bethermin, M., Faisst, A., Le Fèvre, O., and Smolçić, V. (2021). Illuminating the dark side of cosmic star formation two billion years after the Big Bang. *The Astrophysical Journal*, 909(1):23.

Tingay, S. and De Kool, M. (2003). An investigation of synchrotron self-absorption and free-free absorption models in explanation of the gigahertz-peaked spectrum of pks 1718- 649. *The Astronomical Journal*, 126(2):723.

Tiwari, P. (2019). Radio spectral index from NVSS and TGSS. *Research in Astronomy and Astrophysics*, 19(7):096.

van Breugel, W., De Breuck, C., Röttgering, H., et al. (1999). Very high redshift radio galaxies. In *Looking Deep in the Southern Sky: Proceedings of the ESO/Australia Workshop Held at Sydney, Australia, 10–12 December 1997*, pages 236–245. Springer.

van Weeren, R., Röttgering, H., and Brüggen, M. (2011). Diffuse steep-spectrum sources from the 74 MHz VLSS survey. *Astronomy & Astrophysics*, 527:A114.

van Weeren, R. J., de Gasperin, F., Akamatsu, H., Brüggen, M., Feretti, L., Kang, H., Stroe, A., and Zandanel, F. (2019). Diffuse Radio Emission from Galaxy Clusters. , 215(1):16.

Vargas-Magana, M., Brooks, D. D., Levi, M. M., et al. (2019). Unraveling the Universe with DESI. *arXiv preprint arXiv:1901.01581*.

Viitanen, A., Allevato, V., Finoguenov, A., Bongiorno, A., Cappelluti, N., Gilli, R., Miyaji, T., and Salvato, M. (2019). The XMM-Newton wide field survey in the COSMOS field: Clustering dependence of X-ray selected AGN on host galaxy properties. *Astronomy & Astrophysics*, 629:A14.

Vito, F., Brandt, W., Stern, D., Assef, R., Chen, C. J., Brightman, M., Comastri, A., Eisenhardt, P., Garmire, G., Hickox, R., et al. (2018). Heavy X-ray obscuration in the most luminous galaxies discovered by WISE. *Monthly Notices of the Royal Astronomical Society*, 474(4):4528–4540.

Walmsley, M., Lintott, C., Géron, T., et al. (2022). Galaxy Zoo DECaLS: Detailed visual morphology measurements from volunteers and deep learning for 314 000 galaxies. *Monthly Notices of the Royal Astronomical Society*, 509(3):3966–3988.

Wang, Q. D., Garcia Diaz, C., Kamieneski, P. S., Harrington, K. C., Yun, M. S., Foo, N., Frye, B. L., Jimenez-Andrade, E. F., Liu, D., Lowenthal, J. D., Alcalde Pampliega, B., Pascale, M., Vishwas, A., and Gurwell, M. A. (2023). X-ray detection of the most extreme star-forming galaxies at the cosmic noon via strong lensing. *arXiv e-prints*, page arXiv:2312.05442.

Wang, W.-H., Barger, A. J., Cowie, L. L., et al. (2013). Radio and Submillimeter Continuum Observations of High-Redshift Galaxies. In Wong, T. and Ott, J., editors, *Molecular Gas, Dust, and Star Formation in Galaxies*, volume 292 of *IAU Symposium*, pages 175–180.

Weisskopf, M. C., Tananbaum, H. D., Van Speybroeck, L. P., and O'Dell, S. L. (2000). Chandra X-ray Observatory (CXO): overview. *X-ray optics, instruments, and missions iii*, 4012:2–16.

Werner, M. W., Roellig, T. L., Low, F., Rieke, G. H., Rieke, M., Hoffmann, W., Young, E., Houck, J., Brandl, B., Fazio, G., et al. (2004). The Spitzer space telescope mission. *The Astrophysical Journal Supplement Series*, 154(1):1.

Wright, E. L., Eisenhardt, P. R., Mainzer, A. K., Ressler, M. E., Cutri, R. M., Jarrett, T., Kirkpatrick, J. D., Padgett, D., McMillan, R. S., Skrutskie, M., et al. (2010). The Wide-field Infrared Survey Explorer (WISE): mission description and initial on-orbit performance. *The Astronomical Journal*, 140(6):1868.

Wu, J., Ghisellini, G., Hodges-Kluck, E., Gallo, E., Ciardi, B., Haardt, F., Sbarrato, T., and Tavecchio, F. (2017). CMB-induced radio quenching of high-redshift jetted AGNs with highly magnetic hotspots. *Monthly Notices of the Royal Astronomical Society*, 468(1):109–121.

Yamamoto, Y., Nagao, T., Yamashita, T., Uchiyama, H., Kubo, M., Toba, Y., Harikane, Y., Ichikawa, K., Kajisawa, M., Noboriguchi, A., Ono, Y., and Kawaguchi, T. (2025). A Wide and Deep Exploration of Radio Galaxies with Subaru HSC (WERGS). X. The Massive and Passive Nature of Radio Galaxies at z $\sim$ 4. , 978(1):102.

Zensus, J. A. (1997). Parsec-scale jets in extragalactic radio sources. *Annual Review of Astronomy and Astrophysics*, 35(1):607–636.

Zhang, J., Bai, J., Chen, L., et al. (2010). X-ray radiation mechanisms and beaming effect of hot spots and knots in active galactic nuclear jets. *The Astrophysical Journal*, 710(2):1017.

Zhang, X., Reich, W., Reich, P., and Wielebinski, R. (2003). New results on the spectral index-flux density relation from the WENSS/NVSS catalogues. , 404:57–62.